LA-UR-04-1420
095399

Annual Report On Regional Aquifer Modeling And Data Analysis

Elizabeth Keating

Velimir Vesselinov

Zhiming Lu

Edward Kwicklis

Hydrology, Geology, and Geochemistry Group

Earth and Environmental Sciences Division

Los Alamos

14679

LA-UR-04-1420

Annual Report On Regional Aquifer Modeling And Data Analysis

LOS ALAMOS NATIONAL LABORATORY
3 9338 00995 4362

Elizabeth Keating

Velimir Vesselinov

Zhiming Lu

Edward Kwicklis

Hydrology, Geology, and Geochemistry Group

Earth and Environmental Sciences Division

Los Alamos

TABLE OF CONTENTS

1 Executive Summary *1*

2 Data Summary *5*

2.1 Water levels **5**

2.2 Porosity **9**

2.3 Permeability **10**

3 Groundwater Velocity in the Regional Aquifer *13*

3.1 Estimates based on 2-D flow, measured hydraulic gradients and field-based hydraulic conductivity estimates **13**

3.2 Geochemical evidence **14**

3.3 Groundwater flow and transport modeling **15**

4 Model Development *19*

4.1 Computational mesh and hydrostratigraphy **19**

4.2 Model Calibrations, Using New Water Level Data from R-wells. **20**

4.3 Predictive Uncertainty **28**

5 Uncertainty in Groundwater Flow Directions *31*

5.1 Model uncertainty **31**

5.2 Impact of parameter uncertainty of predicted flow directions **33**

5.3 Theoretical basis **34**

5.4 Application to flow direction uncertainty **35**

5.5 Benefit of new data to reduce model uncertainty **38**

5.6 Summary **40**

6 Uncertainty in Lateral Fluxes to Aquifer Beneath LANL *41*

6.1 Abstract **41**

6.2 Introduction **42**

6.3 Model development **42**

6.4 Parameter estimation **44**

6.4.1 Steady-state basin model results 45

6.4.2 Steady-state sub-model results 46

6.4.3 Transient results 47

6.5 Uncertainty of fluxes across lateral boundaries of the submodel 47

6.6 The influence of flux uncertainty on transport calculations 48

7 Hydrologic Data Collection Priorities For Regional Aquifer Characterization 51

7.1 Flow directions 51

7.1.1 Permeability characterization 52

7.1.1.1 Large-scale permeability variations 52

7.1.1.2 Medium-scale permeability variations 52

7.1.1.3 Small-scale permeability variations 53

7.1.1.4 Definition of hydrostratigraphic zones 54

7.1.1.5 Data/analysis needs 54

7.1.2 Hydraulic gradients 55

7.1.2.1 Horizontal gradients 55

7.1.2.2 Vertical gradients 56

7.2 Groundwater velocity 57

7.3 Recharge/discharge 58

7.4 Montoring 59

8 Development of facies-based models of the Puye formation 61

8.1 Overview Of Stochastic Approaches To Modeling Heterogeneity 62

8.2 Markov Chain Theory 67

8.3 Derivation Of Statistical Properties For Puye Formation 71

8.3.1.1 Spatial analysis of geophysical data 71

8.3.1.2 Variogram overview 71

8.3.1.3 Analysis of textural classes identified in well logs and outcrops 73

8.4 Generation Of Markov Chain Models 75

8.4.1 Parameter derivation 75

8.4.2 Model domain and grid resolution 77

8.4.3 Conditioning 78

8.5 Images. 78

8.6 Calibrating 2-D Markov chain models to head data 81

8.7 Conclusions and suggestions for future work 83

8.8 Equivalent/Effective Permeability 87

8.9 Upscaling **91**

9 REFERENCES ***103***

10 Appendix A. Water level and permeability data ***107***

Appendix B. Hydrostratigraphy as interpolated onto locaL-scale model grid ***113***

Appendix C. data used in Markov chain models ***115***

LIST OF FIGURES

Figure 2-1. Water table elevation. Data used for drawing contours are listed in TableA-1 6
Figure 2-2. Heads projected onto a E-W cross-section through Pajarito Plateau 7
Figure 2-3. Effective porosity estimates for the Puye Formation, based on geophysical logs 9
Figure 2-4. Hydraulic conductivity estimates for the Puye Formation, based on geophysical logs 11
Figure 2-5. Permeability estimates from field-based methods 11
Figure 3-1. Histogram of velocity estimates, based on hydraulic testing and 2-D flow 14
Figure 3-3. E-W component of velocity at the water table, in m/yr 16
Figure 3-4. Histogram of E-W component of velocity at the water table, predicted by flow model 16
Figure 3-5. Ratio of horizontal to vertical velocity 18
Figure 4-1. Recharge rates, in mm/yr 23
Figure 4-2. Inverse model estimates of permeability, compared to field-based estimates 24
Figure 4-3. Confidence limits for inverse model estimates 24
Figure 4-4. Simulated water table contours. Measured water levels are indicated next to red dots. Dotted lines show contours indicate locations of model error, where simulated and measured contours differ Contour interval = 25m 25
Figure 4-5. Simulated heads for local-scale model (2) 26
Figure 4-6. Simulated heads for local-scale model (2) 27
Figure 4-7. Cross-section of simulated heads (y=-123,000m) , with representative particle tracks 28
Figure 5-1. Simulated pre-development water table contours (in feet) and model errors at wells (simulated - measured) 32
Figure 5-2. Distribution of model errors (simulated - observed) 32
Figure 5-3. Histogram of model errors for drawdowns due to pumping (simulated - observed, in feet) 33
Figure 5-4. Inverse estimates and prior data of permeability 34
Figure 5-5. Particle trajectories that correspond to the maximum and minimum y value at x= 18290. Blue dots are wells used in steady-state (predevelopment) calibration; red dots are wells used in transient calibration. Green x's are locations of hypothetical wells 36
Figure 5-6. Model parameters. Calibration results shown in green; parameters corresponding to mimum and maximum predictions shown in red and blue 37
Figure 5-7. Types of rocks particles travel through. 38
Figure 5-8. Cross-sectional view of particle paths 38
Figure 5-9. Sensitivity of model predictions to head measurements in hypothetical wells 39
Figure 5-10. Residuals (simulated - observed) for the two models 39
Figure 7-1. Two alternative water table contour maps, drawn using the same data 56
Figure 7-2. Locations with vertical gradient information 57
Figure 7-3. Particle tracking results, showing trajectories of particles released at the water table beneath source areas in Mortendad Canyon 59

Figure 8-1. . Semivariogram calculated from permeability data in well R-7 72
Figure 8-2. Semivariogram calculated from permeability data in well R-19 73
Figure 8-3. Semivariogram calculated from permeability data in well CDV-R-15 73
Figure 8-4. Location of wells (blue dots) and outcrop data (red dots 74
Figure 8-5. Location of wells used for Markov chain model conditioning and flow model calibration 82
Figure 8-6. Markov chain model, measured and simulated heads 85
Figure 8-7. The hydraulic conductivity fields with different resolutions 94
Figure 8-8. : The hydraulic head fields obtained from different resolutions of the hydraulic conductivity fields 95
Figure 8-9. The longitudinal velocity fields obtained from different resolutions of the hydraulic conductivity fields 96
Figure 8-10. Concentration fields corresponding to different resolutions of heterogeneous hydraulic conductivity fields 99
Figure 8-11. : Concentration fields corresponding to different resolutions of homogeneous hydraulic conductivity fields 100
Figure 8-12. Trajectories of the particle released at (0, 12,8m), for different resolutions of the hydraulic conductivity fields 101
Figure B-1. Local-scale grid, with elements colored according to hydrostratigraphy 113
Figure B-2. E-W cross-section of local-scale grid, beneath LANL 114

LIST OF TABLES

Table 2-1. Estimated E-W hydraulic gradients 6
Table 2-2. Estimated vertical gradients, ordered by magnitude 8
Table 2-3. Effective porosity estimates based on geophysics data 10
Table 2-4. Summary of recent hydraulic conductivity estimates from field-based testing (ft/day) 12
Table 3-1. Calculated travel times, assuming 2-D horizontal flow 14
Table 3-2. Permeability and porosity values used in velocity calculations (st_cap9) 17
Table 4-1. Model parameter estimates 21
Table 5-1. Results of predictive analysis 36
Table 8-1. Parameters used for Markov chain models 76
Table 8-2. Parameters used for 2-D Markov chain models 77
Table 8-3. Comparison of geophysical data and textural class in R-19 and CDV-R-15 83
Table A-1. Most recent water level data from wells in the vicinity of LANL 108
Table A-2. Permeability data for wells on the Pajarito Plateau, and average linear velocity estimates 110
Table C-1. Textural class data compiled from Waresback (1986) dataset 115
Table C-2. Textual class data compiled from drillers lithologic logs 115
Table C-3. Total thickness of the each material in wells and outcrop sections 116
Table C-4. Thickness of Totavi Lentil measured at outcrops (m) 117

ACKNOWLEDGEMENTS

Our work has benefited from the contributions of many people, including Charlie Nylander, members of the GIT, the ER project, the porous flow and geology teams of EES-6, and the field teams collecting the data from the R-wells. In particular, we would like to thank Dave Broxton, Bill Stone, David Rogers, Dave Vaniman, Bruce Robinson, and George Zyvoloski.

This work has been funded by DP programs as part of Los Alamos National Laboratory's Hydrogeologic Workplan.

1 EXECUTIVE SUMMARY

This report summarizes several projects related to data compilation and analysis (including flow and transport modeling) in support of regional aquifer characterization.
The primary goals of the FY01 work have been to update estimates of ***flow directions*** and ***velocities*** using the regional aquifer model, supplemented with new data collected from R-wells, to evaluate model uncertainty and prioritize new data collection accordingly, and to continue development of a facies-based model of heterogeneity for the Puye Formation.

The fundamental goal for the regional aquifer model is to provide estimates of three-dimensional groundwater flow directions and velocities, qualified by technically-defensible estimates of model uncertainty. The aspects of aquifer characterization necessary to accomplish this goal are water level data, hydrostratigraphic zone delineation, permeability and porosity estimates, and flux estimates (recharge/discharge). With the addition of recent R-well data, our ability to estimate lateral flow directions using existing water level data and flow modeling has improved significantly. Both measured hydraulic gradients and flow model predictions continue to indicate easterly flow. Our understanding of vertical gradients has improved as well. Strong downward gradients exist in several locations; near-neutral conditions exist, as well. To date, no strongly upward gradients have been measured in R-wells. A significant gap in our vertical gradient dataset is the northwestern portion of LANL. Lack of vertical gradient information in this area could compromise our ability to determine the correct depth for monitoring wells in Los Alamos and Pueblo Canyons.

The new water level data has been incorporated into flow model calibration and the resulting estimates of large scale permeability have become more certain. In particular, our estimates of permeability for the Puye Formation and basalt flows have become well-constrained by water level and flux data. Estimates for Santa Fe Group rocks continue to be fairly certain. The outstanding problem with regard to estimates of large-scale permeability is that model-derived estimates for the Santa Fe Group are substantially lower than field-based estimates (e.g. pump tests in Los Alamos Canyon). This may be due to scaling effects or structural features such as north-south trending low-permeability fault zones. Unfortunately, collecting data to conclusively prove or disprove this hypothesis would require very expensive multi-hole testing. Other possible reasons for the discrepency (dramatic underestimation of flux through the aquifer and/or overestimation of aquifer thickness) do not appear to be plausible at present but are worthy of further evaluation.

In-situ hydraulic testing in R-wells and geophysical estimates of permeability have provided more evidence of large variation in medium- and small-scale permeability within the Puye Formation. Unfortunately, at present we do not have a robust conceptual model that relates these permeability variations to lithology. Geophysical logs have also provided small scale estimates of effective porosity.

Geophysical logs indicate that a large proportion of the Puye Formation has very low porosity; these same zones also have very, very low permeability. This result should be tested by collecting core samples and conducting laboratory analyses; until they are verified in this way the porosity data will not be incorporated into flow and transport modeling.

We have continued to evaluate the adequacy of hydrostratigraphic zonation (defined by the 3-D geologic model) by comparing simulated and observed water levels under a variety of parameter combinations. The results are mixed. It appears that the delineation between basalt flows and sedimentary rocks has real hydrologic significance; the basalt flows appear to be substantially higher in permeability. Differing transport characteristics, assuming that flow in basalts occurs primarily through fractures, amplifies the importance of this delineation. At present, however, the delineation between the "Los Alamos Aquifer" and the lower Santa Fe Group does not appear to have hydrologic significance, nor does the delineation between the Puye fanglomerate and the Totavi Lentil. This result contrasts with previous studies (Rogers, Birdsell) which demonstrate a strong hydrologic significance of stratigraphy within the vadose zone.

Our calibrated flow models reproduce many of the general trends in water level data (drawdowns in wells over time, of approximately the correct magnitude, easterly gradients, downward gradients in the vicinity of R25, etc.). Our errors are unbiased. However, significant discrepancies exist between observed and simulated water levels in some wells. This result, in combination with the small- and medium-scale heterogeneity observed within the Puye Formation and the lack of apparent hydrologic significance of several defined hydrostratigraphic zones, has important implications. Clearly, small- and medium-scale heterogeneity exists that is not incorporated in the flow model and which compromises our ability to simulate local effects within the flow field. Large-scale heterogeneity, with the exception of basalt flows interfingering with sedimentary units, does not appear to be controlled by stratigraphy. Further characterization is necessary to determine if large-scale heterogeneity is present within the sedimentary rocks, and, if so, what (if any) relation it may have to lithology or stratigraphy.

We have completed two formal analyses for the effects of parameter uncertainty (permeability, recharge rates, and specific storage) on model predictions. The first is an analysis of the uncertainty in the predictions made using the basin model for lateral fluxes to the aquifer beneath LANL. This analysis showed that water level and flux data (baseflow discharge to the Rio Grande) is sufficient to support model predictions that little or no groundwater enters the aquifer from the north or leaves the aquifer to the south. In contrast, there is large uncertainty in flux estimates from the west (none or a relatively large amount relative to the total water withdrawn from municipal supply wells). Subsequent transport calculations were insensitive to these uncertain fluxes; however. The importance of this uncertainty will depend on the model application.

The second analysis was of uncertainty in flow directions downgradient from R25. This analysis demonstrated fairly low uncertainty in lateral flow directions (regardless of parameter values, calibrated models always predict generally easterly flow); however, much greater uncertainty accompanies the

vertical component of flow and the ultimate discharge point (PM-2 or the Rio Grande). Sensitivity analysis showed that of multiple possible locations for new water level data to reduce predictive uncertainty, multi-level data at or near R25 would be the most valuable. This analysis was completed before many of the recent water level data became available (including data from R25) and therefore may overestimate uncertainty.

Finally, we made substantial progress in our development of stochastic, facies-based models of the Puye Formation. Our goals for this project were to 1) integrate borehole and outcrop-derived geologic data into facies-based, Markov chain models of the Puye, 2) calibrate these models against water level data, and 3) develop methodology to preserve the transport characteristics of fine-scale models of heterogeneity when upscaling to a coarser-scale flow and transport model. We made substantial progress in areas (1) and (3). So far, our effort to calibration the models against water level data have not been successful. This may be because our initial models are overly simplistic (e.g. 2-D, two classes) or because our conceptual model of which facies are most hydrologically important within the Puye is incorrect. Making further progress in model calibration will require detailed analyses of existing hydrologic and geologic data from R-wells to determine which depositional facies have distinctive hydrologic properties. With this understanding, the methods we have developed for the Markov chain models should be easily applied and presumably model calibration will be much more successful.

2 DATA SUMMARY

This chapter describes water level, porosity, and permeability data for the regional aquifer. It draws heavily on data presented by Purtymun (1995), Broxton (2001a,b,c,d) and Longmire (2001)

2.1 Water levels

Significant progress has been made since Oct. 2000 in the collection and compilation of water level data. Table A-1 lists the most recent water level data available for all wells completed in the regional aquifer, including recent data collected in R-wells. Because of the increased density of water level data collected in test wells that penetrate only the uppermost portion of the aquifer, it is possible to construct a water table map for the plateau that does not include data from water supply wells. Figure 2-1 shows a contoured map of water levels in these wells (indicated in Table A-1). This figure demonstrates the slope of the water table is generally to the east. Table 2-1 shows calculated horizontal gradients for several well pairs; estimated gradients range from 0.01 to 0.03.

Figure 2-2 shows head data in in vertical cross-section; each well is projected onto a E-W plane. This figure illustrates the downward gradients to the west and the upward gradients to the east. In general, the gradients shown in Figure 2-1 and Figure 2-2 are gradients that would be expected in a relatively homogeneous aquifer with topographically-driven flow (recharge in high areas, discharge in low areas (Rio Grande).

Table 2-2 lists the vertical gradients estimates for the plateau. Some of these estimates are quantitative, calculated using water levels measured in R-wells completed with multiple screens. Others are qualitative, calculated using water levels measured in pairs of nearby wells. These estimates show that by far the strongest vertical gradients measured have been downward (R25, R19). Moderate downward gradients are also present near TW-1 and R22. Slight upward gradients have been estimated in the vicinity of R9 and TW-3. In general, all the measured upward gradients have been fairly small and are possibly within the margin of error for water level measurement accuracy. Significant downward gradients are important because they indicate possible zones of recharge and potential pathways for contaminant migration downward.

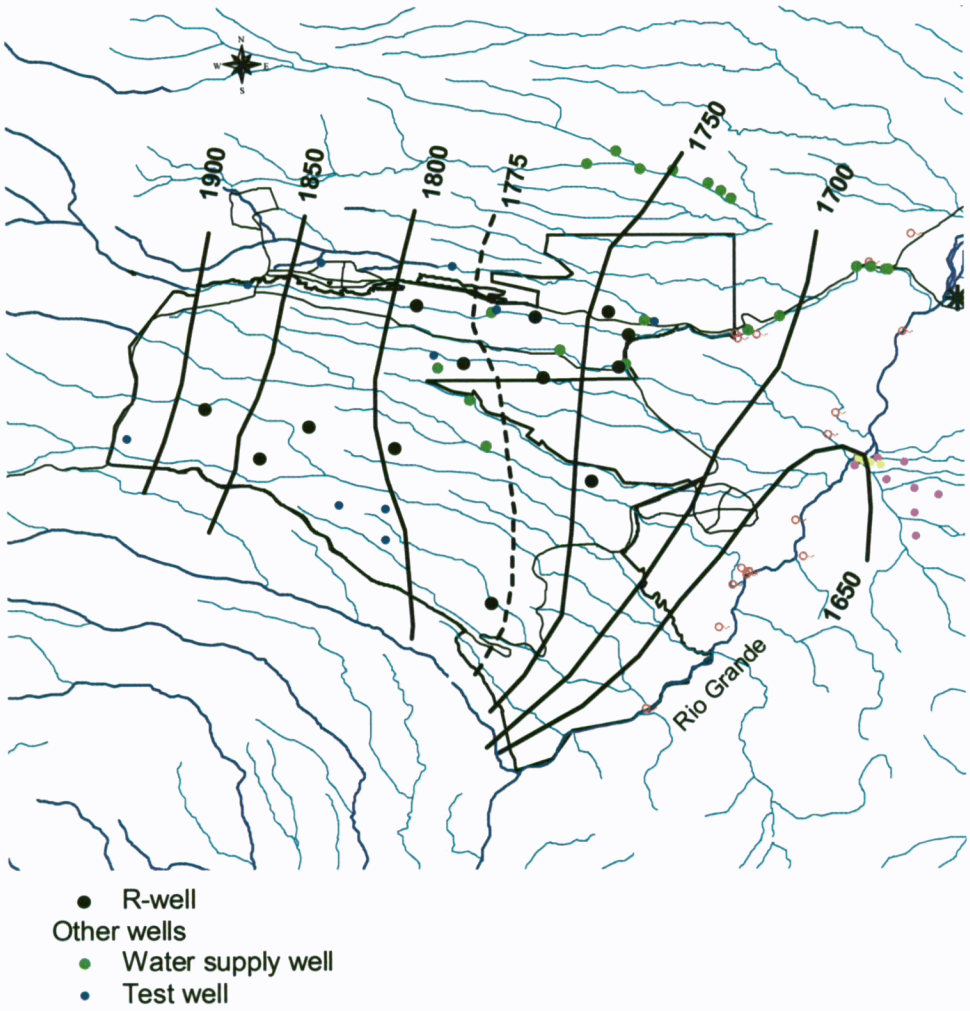

Figure 2-1. Water table elevation. Data used for drawing contours are listed in TableA-1.

Table 2-1. Estimated E-W hydraulic gradients

Pair of Wells				E-W Distance (m)	Gradient (m/m)
Upgradient Well	Water level (m)	Downgradient Well	Water level (m)		
R25	1836	CDV15-3	1833	2189	0.02884
CDV15-3	1833	R19	1795	4710	0.02149
DT-10	1805	R22	1747	5195	0.01121
R15	1785	R12	1738	3684	0.01283

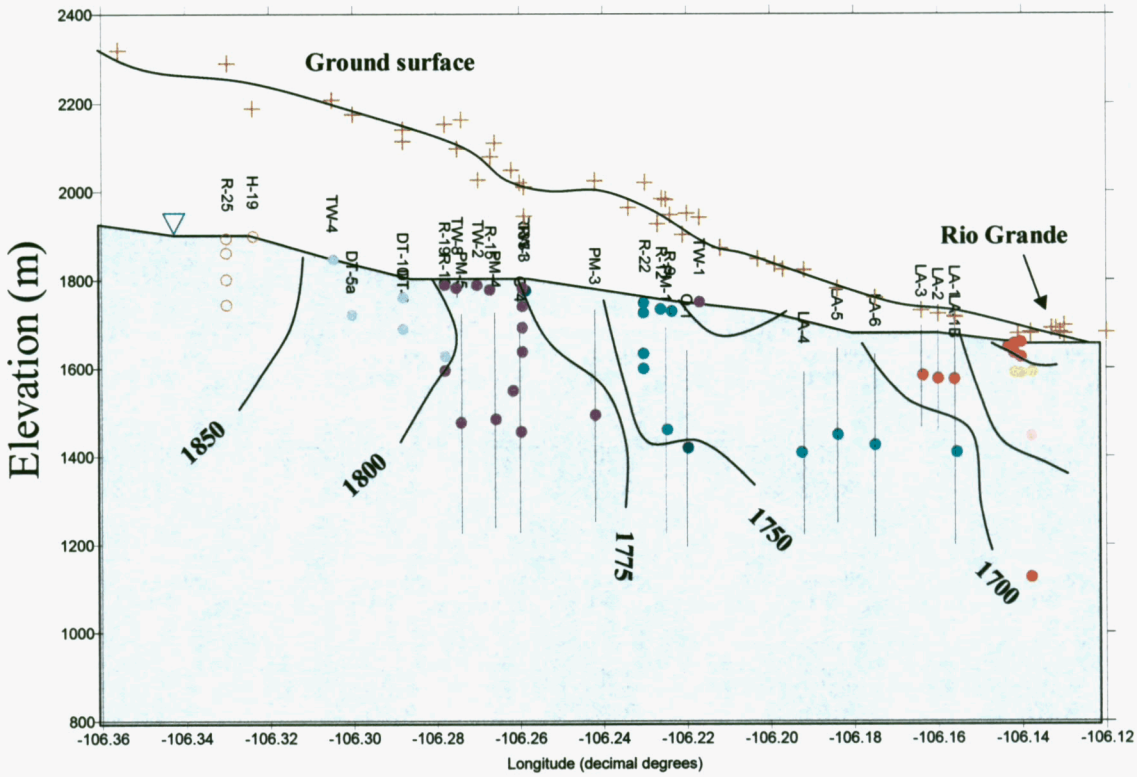

Figure 2-2. Heads projected onto a E-W cross-section through Pajarito Plateau

Table 2-2. Estimated vertical gradients, ordered by magnitude

Well	Vertical gradient	
R-19-6	0.08	Weakly upward
R9/PM-1	0.05	
TW3/O-4	0.05	
R9/O-1	0.03	
CdV-R-15-3-6	0.02	
R-31-4	0.01	Nearly neutral
R-31-3	0.01	
R-31-5	0.02	
R-22-2	0.07	
TW1/O-1	0.10	Weakly downward
R-22-4	0.11	
R-25-7	0.13	
R-25-8	0.13	
R-22-3	0.14	
R-25-6	0.15	
R-19-7	0.28	
R-25-4	0.86	
R-25-5	1.10	
R-25-3	1.72	Strongly downward

2.2 Porosity

Geophysics data provide us with our first site-specific estimates of effective porosity. The geophysical data are measured by Schlumberger using the Combinable Magnetic Resonance (CMR) tool. The CMR tool uses the nuclear magnetic resonance (NMR) technique to log porous aquifers. The NMR measurements can provide different types of porosity-related information. For example, they can tell how much fluid is in the formation and give detail information about the pore size distribution of the formation from which the porosity, bound and free water, and hydraulic conductivity are estimated. However, the estimated values depend on the choice of cutoffs for the so-called transverse relaxation time T_2. For instance, the volume of the clay-bounded water is usually determined from the distribution of the relaxation time using a cutoff value of $T_2 = 3$ms, and the value of the effective porosity corresponding to $T_2 > 33$ ms in the distribution of the relaxation time. Geophysical estimates of porosity are shown in

Table 2-3 and Figure 2-3. Effective porosity estimates for the Puye Formation, based on geophysical logs . Average effective porosity for the Puye ranges from .07 to .1, with some relatively small zones with significantly higher porosity. For the two zones in R19 that showed high permeability in hydraulic testing, the porosity estimates were approximately 0.2. Analyses for the same data, assuming different values of T_2. (12ms and 60ms) showed that these results are not sensitive to the value of this uncertain number.

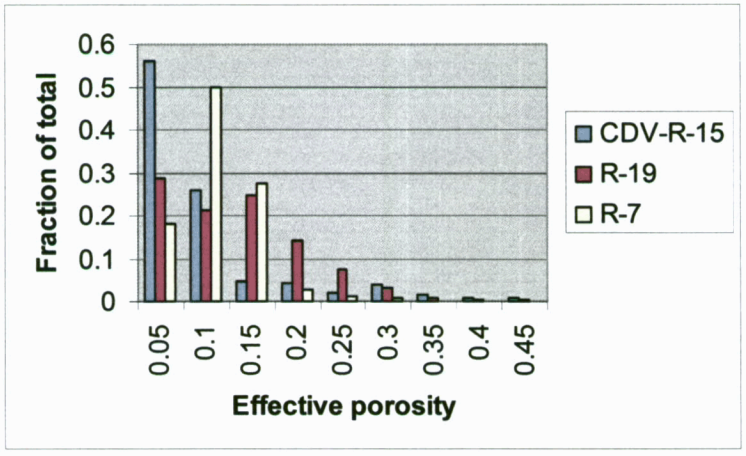

Figure 2-3. Effective porosity estimates for the Puye Formation, based on geophysical logs

Table 2-3. Effective porosity estimates based on geophysics data

Well	Interval	Mean	N
CDV-R-15	All data within Puye	0.07	744
CDV-R-15	Screen 4	0.06	87
CDV-R-15	Screen 5	0.01	13
CDV-R-15	Screen 6	0.16	15
R19	All data within Puye	0.1	1466
R19	SCREEN 6	0.2	14
R19	SCREEN 7	0.2	15
R7	All data within Puye	0.09	293

2.3 Permeability

Two field-based methods have been used to estimate permeability since Oct. 2000 hydraulic testing of wells and analysis of geophysical logs. In the case of geophysical logs, the permeability k is derived from porosity according to the following formula:

$$k = C\phi^4 T_{2,\log}^2 \qquad (2\text{-}1)$$

where ϕ is the CMR porosity, $T_{2,\log}$ is the logarithm mean of the T_2 distribution, and C is a constant, typically 4 for sandstones and 0.1 for carbonates. All the data from the Puye Formation is shown in Figure 2-4. Summary statistics are provided in Table 2-4. In two wells, both methods were used which provides an opportunity for comparison. Unfortunately, these two estimates in poor agreement, even in a relative sense. The most probable reasons for this include scaling effects, errors in data analysis, poor test performance, or some combination of both. In CDV-R-15 the two methods were of the same order of magnitude; in R19 hydraulic testing suggests a much higher permeability than geophysics. It is interesting to note, however, that geophysical logs (not shown here) suggests that a very permeable zone is present just below the zone of hydraulic testing; perhaps this lower zone impacted the hydraulic test results.

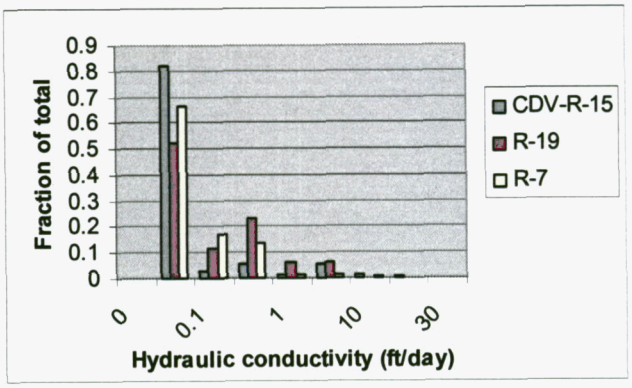

Figure 2-4. Hydraulic conductivity estimates for the Puye Formation, based on geophysical logs

Figure 2-5 shows all the field-based permeability estimates currently available for the plateau. Different symbols correspond to different methods. Strictly speaking, this dataset cannot be used to compare methods because in most cases (excepting those listed in table 2), the tests were conducted in different portions of the aquifer. The addition of injection test and geophysical data to the previous dataset shows that the range of permeability for both the Puye and the basalts is larger than pump test estimates suggested. These estimates clearly show the presence of low permeability zones within both the basalts and the Puye Formation.

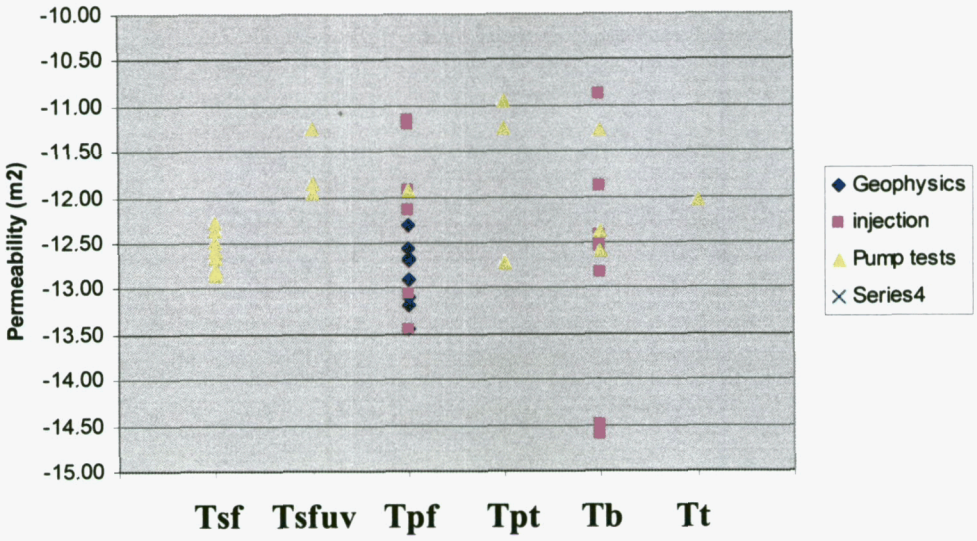

Figure 2-5. Permeability estimates from field-based methods

Table 2-4. Summary of recent hydraulic conductivity estimates from field-based testing (ft/day)

Well	Interval	Geophysics		Hydraulic testing	Formation
		Mean[a]	N		
R19	All data within Puye	0.35	1466		Puye
R19	Screen 6	1.4	14	17.5	Puye
R19	Screen 7	0.6	15	19.6	Puye
CDV-R-15	All data within Puye	0.56	744		Puye
CDV-R-15	Screen 4	0.22	87		Puye
CDV-R-15	Screen 5	0.18	13	0.25	Puye
CDV-R-15	Screen 6	0.74	15	0.1	Puye
R7	All data within Puye	0.1	293		Puye
R31	Screen 4			0.009	basalts
R31	Screen 5			0.007	basalts
R31	Screen 2			0.42	basalts
R31	Screen 3			3.6	basalts

[a] geometric mean

3 GROUNDWATER VELOCITY IN THE REGIONAL AQUIFER

In this chapter we compare three methods for estimating groundwater velocity in the regional aquifer. The first is a very simple method, which assumes that flow is horizontal and relies entirely on hydraulic conductivity estimates taken from pump tests in wells on the plateau. Purtymun (1995) used this approach; acknowledging spatial variation in permeability but assuming uniform porosity. We calculate a range of velocities for the plateau, using this method based on a slightly larger set of hydraulic conductivity estimates (including recent data from R-wells). Second, we use the very limited geochemical tracer data available to provide estimates which are completely independent from the first, although they share the simple assumption of two-dimensional flow. The third approach is based on calibrated flow models. This approach provides three-dimensional estimates of velocity and uses spatially distributed estimates of both permeability and porosity.

3.1 Estimates based on 2-D flow, measured hydraulic gradients and field-based hydraulic conductivity estimates

The regional hydraulic gradient is generally to the east, with a slight southerly component in some areas. As shown in Table 2-1, the gradient varies from approximately 0.03 to 0.01. Locally, gradients may depart from these larger scale estimates; however, uncertainty due to local variations at scales less than R-well spacing is probably larger than uncertainty due to measurement error. Permeability data (provided in Table A-2) show that considerable variation in permeability is present in the aquifer. By assuming a hydraulic gradient of 0.01 and a porosity of 0.1, we calculate a range of groundwater velocities from 0.1 to 363 m/yr, with a median value of 11 m/yr (see Table A-2). Using a similar method, Purtymun (1995) estimated that groundwater velocities vary from a minimum of 6 m/yr (Los Alamos well field) to 105 m/yr (near DT wells). We expect these velocities may be larger than a site-scale "average" velocity since many of the permeability estimates are derived from water supply wells which were presumably placed in the highlyt permeabile portions of the aquifer.

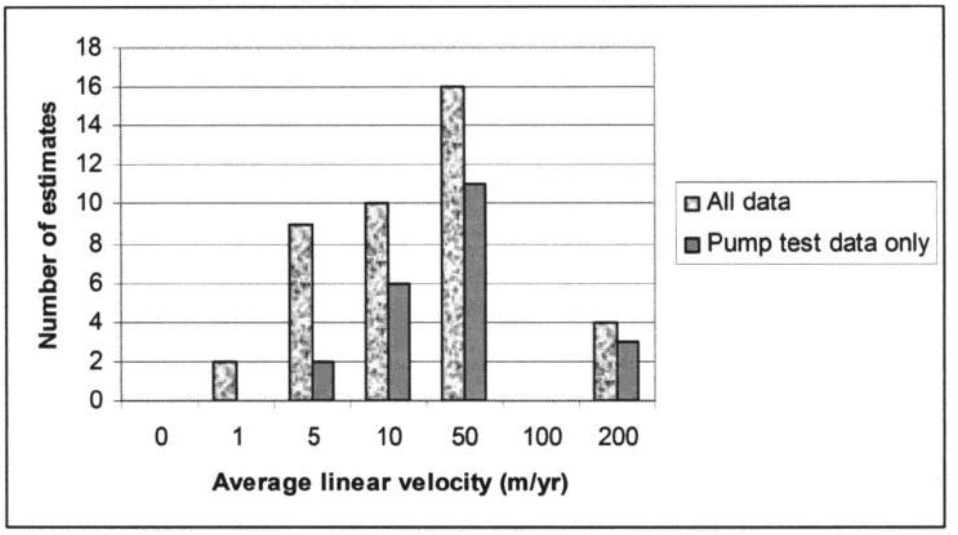

Figure 3-1. Histogram of velocity estimates, based on hydraulic testing and 2-D flow

Assuming 2-D, horizontal flow, approximate travel times would be as follows:

Table 3-1. Calculated travel times, assuming 2-D horizontal flow

Location	Horizontal distance	Assumed velocity	Travel time
R-25 to PM-2	6.2 km	11 m/yr	564 yrs
R-25 to Rio Grande	14.5 km	11 m/yr	1318 yrs

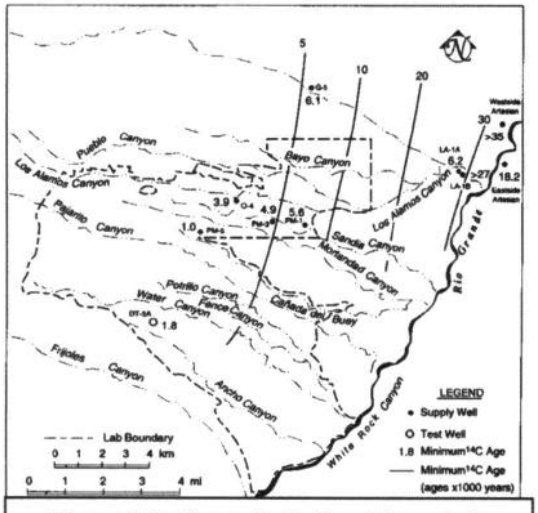

Figure 3-2. Figure 3. Carbon 14 age dates (Rogers et al., 1996)

Vertical gradients are well documented both on the plateau (both downward and upward) and near the Rio Grande (upward); hence flow paths are most certainly three-dimensional and therefore travel times may be longer than those calculated above.

3.2 Geochemical evidence

Carbon age dates presented by Rogers et al. (1996) suggest that waters are progressively older from

west to east. Again, assuming 2-D flow from west to east, we can calculate groundwater velocities. For the eastern portion of the plateau, assuming a distance of 7.8 km between PM3 (age = 4900 years) and LA-1B (age >= 27000 years), we calculate a *maximum* velocity of 0.35 m/yr. For the central portion of the plateau, assuming a distance of 3.2 km between O-4 (3900 years) and PM-1 (5600 years), we calculate a velocity of 1.9 m/yr. These calculations ignore the effects of 3-D flow, mixing in wells with long screens, and (near the Rio) mixing of waters converging near the regional discharge zone. As expected, these estimates,which reflect large-scale average velocities, are slower than those derived from hydraulic test data.

Unfortunately, we cannot use contaminant data (e.g. ^{3}H, HE, Ur) to estimate travel times. These data *do* demonstrate that relatively fast travel times exist within the vadose zone. However, we cannot estimate how much lateral transport occurred within alluvial or intermediate perched zones before the contaminants reached the regional aquifer and therefore the distance of travel within the regional aquifer is unknown.

3.3 Groundwater flow and transport modeling

Numerical modeling has both advantages and disadvantages in comparison to the simple methods described above. The primary advantages are that the model considers the full three-dimensionality of the aquifer including spatial variation in recharge rates, pumping rates, hydraulic conductivity and porosity. The resulting predictions of flowpaths and velocities are fully three-dimensional. The x component of velocities at the water table predicted by the regional model are shown in Figure 3-3. These estimates are very sensitive to assumptions about porosity. The values used for these calculations are shown in Table 3-2. The median value of velocity is 0.8 m/year. This estimate is lower than the mean estimate obtained by hydraulic testing data, and is similar to the estimate derived from geochemical data. One reason for the lower velocities is the fact that the model assumes a lower permeability for the Santa Fe group than hydraulic tests suggest. The reason for this is unclear, however, it may be that the large-scale effective permeability of this unit is impacted by north-south trending faults (Kelley 1978).

In some locations, particularly in basalt units which are assumed to have very low porosity (fracture-flow only), have much higher predicted velocities Another important aspect to the flow model results is that in a substantial portion of the water table, the vertical component of velocity is much larger than the horizontal. For approximately half the water table surface (within model

boundaries), flow is predominately horizontal. However, for approximately 10% of the area within the model, flow is nearly completely vertical (downward or upward).

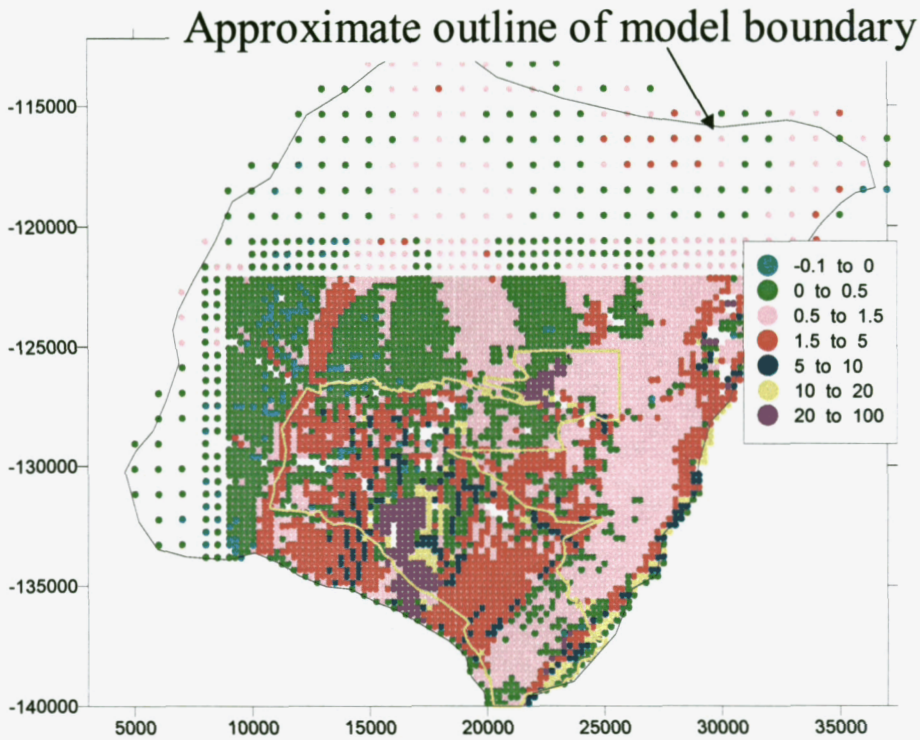

Figure 3-3. E-W component of velocity at the water table, in m/yr

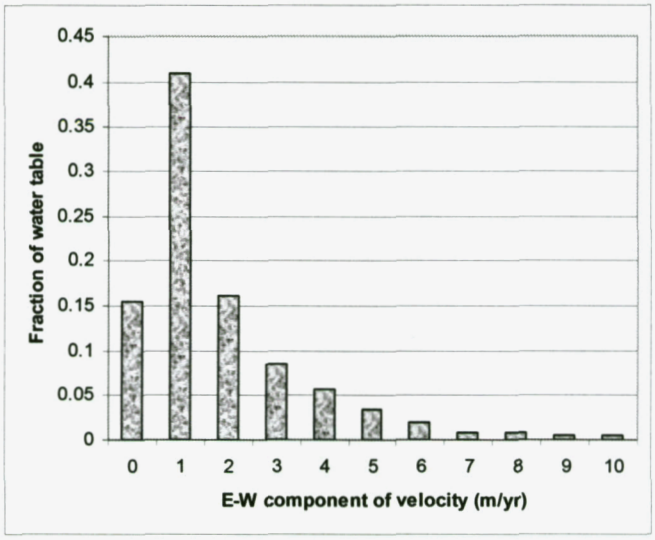

Figure 3-4. Histogram of E-W component of velocity at the water table, predicted by flow model

Table 3-2. Permeability and porosity values used in velocity calculations (st_cap9)

Hydrostratigraphic Unit			Permeability Log m^2	Porosity
Pre-tertiary units	Deep basement		15.0	0.02
	Paleozoic/Mesozoic	Deep	17.4	0.1
		Shallow	14.0	0.1
Volcanic rocks	Tschicoma Formation	Deep	15.3	0.05
		Shallow	15.2	0.05
	Cerros del Rio basalts	Tb1	11.0	0.05
		Tb2	12.3	0.05
		Tb4	11.4	0.05
Pajarito Fault zone			14.9	0.1
Sedimentary rocks	Santa Fe Group	Deep	15.5	0.15
		Shallow -xy	13.2	0.25
		Shallow -z	14.0	
	Los Alamos aquifer		13.3	0.3
	Puye formation	Totavi Lentil	13.5	0.3
		Fanglomerate - xy	12.9	0.25
		Fanglomerate - z	15.5	

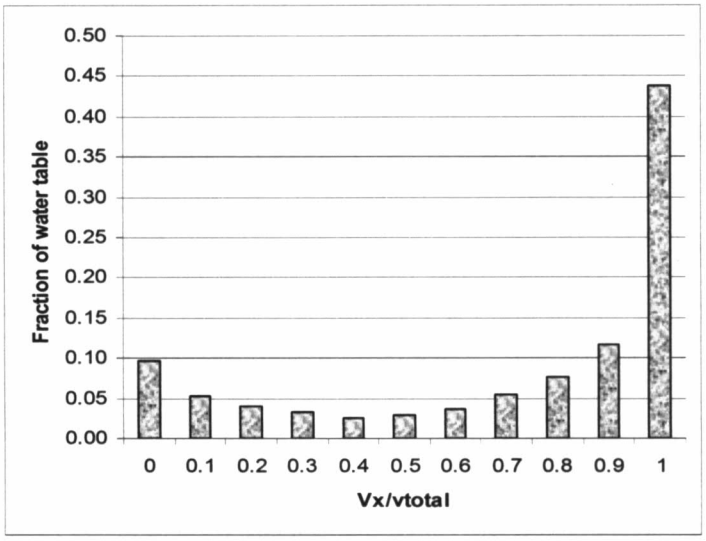

Figure 3-5. Ratio of horizontal to vertical velocity

4 MODEL DEVELOPMENT

Several significant model developments have been accomplished this year. One, the process of mapping geologic features onto the numerical grids (both basin and submodel) has been improved, providing more faithful renditions of the conceptual and numerical geologic models (see Appendix B). Second, new water level data (R-wells) have been incorporated into the model calibration process. This addition has caused a significant decrease in model parameter uncertainty, particularly with regards to the Puye Formation. Third, geophysical, geologic, and hydrologic data have been integrated into stochastic, facies-based models of the Puye Formation. This work is summarize in Chapter 8. This process, while providing some new insights into the hydrologic behavior of the Puye, has also highlights gaps in our understanding of geologic controls on hydrologic properties within the Puye.

We have also made substantial progress in evaluating model uncertainty and prioritizing new data collection that would most reduce model uncertainty. We have analyzed uncertainty in lateral fluxes that enter/exit the aquifer beneath LANL and uncertainty in flow path directions in the western portion of the aquifer. Both of these analyses evaluate the combined impact of parameter uncertainty (all parameters) under model calibration constraints; this process is much more powerful than traditional sensitivity analysis.

4.1 Computational mesh and hydrostratigraphy

The computational grids for our basin- and local-scale models were originally designed by Keating et al. (1999). In FY01, we have slightly modified and improved these grids.

The grids were generated using LaGriT (Trease et al., 1995) and debugged and visualized using GMV (Ortega, 1995) and Tecplot (Amtec, 2001). Basin- and local-scale grids have the same horizontal grid spacing. The grids include a zone of octree mesh refinement in the region of LANL. The fine horizontal grid spacing is 250 × 264 m in x and y direction, respectively; the course grid spacing is 1,000 × 1,055 m. The grids are structured except for the transitional regions between the fine and coarse griding. Outside these transitional regions the tetrahedral elements of the grid can be collapsed to hexahedral elements. For both basin- and local-scale grids, the vertical spacing is 500 m at the bottom and it changes to 50 m at elevation of 1,100 m. The local-space grid is further refined above elevation equal to 1,550 m where the vertical grid spacing is just 12.5 m (Keating et al., 1999).

In the new grids, the nodes are ordered based on their coordinates which simplifies the pre- and post-processing of model data. The shallow portions of the crystalline units are defined by a surface, which is 800 m below the model top boundary in the central regions and is thinning with the elevation along the mountain slopes. The shallow units of the Santa Fe group and Tschicoma formation are defined by a surface, which is 1,500 m below the model top boundary. We have also refined the discretization of basalts. Additional efforts were taken to better characterize the top model boundary.

Respectively for the new basin- and local-scale grids, the number of nodes is 277,951 and 172,741 and the number of tetrahedral elements is 1,528,407 and 949,835. The local scale-grid and a cross-sectional view beneath LANL are shown in Appendix B.

4.2 Model Calibrations, Using New Water Level Data from R-wells.

As described in Keating et al.(1999,2000), our models are calibrated using two datasets: one, predevelopment water levels, and two, drawdowns measured over time due to pumping in municipal wells. Our parameter estimation procedure seeks the parameter values (permeability, recharge rates) that provide the best fit to both these datasets simultaneously. Using these two datasets should provide the most accurate estimates of permeability and recharge, however, this process precludes the use of recent water level measurements in wells for which there are no corresponding "predevelopment" data. To take advantage of the many recent R-well measurements we modified our calibration dataset. We are now calibrating to every water level data available in 5-yr snapshots. Our flux calibration targets have not changed significantly.

Using parameter estimation code (PEST) we estimated permeabilities and recharge model parameters for both the basin model and the submodel. Table 4-1 shows the parameter estimates and corresponding confidence intervals. For the submodel, we used two different approaches to estimation of recharge rates. The first is the same elevation dependent model used for the basin model, as described in Keating et al (2000). The second is a more complex model emphasizing focused recharge along canyons, developed as part of the First Order Groundwater Assessment Project (ER Project). Recharge rates for this model are shown in Figure 4-1. The advantage of this approach is that since recharge rates are assumed *a priori* this reduces uncertainty in other model parameters (permeability). This may be misleading, however, since the recharge rates specified in this model are still quite uncertain.

Table 4-1. Model parameter estimates

Parameters	Short name	Units	Transient basin model		Transient sub model (1)		Transient sub-model (2)	
			Estimates	Conf. limits	Estimates	Conf. limits	Estimates	Conf. limits
Recharge								
dz	dz	[m]	1.00	(fixed)	1.00	(fixed)		
Z_{min}	zmin	[m]	2195.68	177.25	2195.68	773.10		
Recharge volume	infl	[m^3]	3844.56	511.89	208.67	(fixed)		
Pemeabilities								
Deep Basement	Basement	$log_{10}[m^2]$	a	a	a	a	-14.98	
Paleozoic/Mesozoic	P/M	$log_{10}[m^2]$	-15.01	3.18	-15.01	28.61	-17.44	
Shallow Paleozoic/Mesozoic (fractured)	Frac. P/M	$log_{10}[m^2]$	c	c	c	c	-14.0	
Pajarito fault zone	Paj.Fault	$log_{10}[m^2]$	-15.34	0.83	-15.34	18.32	-15.0	
Tschicoma Formation	Tt	$log_{10}[m^2]$	a	a	a	a	-15.0	
Tschicoma formation - shallow	Frac. Tt	$log_{10}[m^2]$	-12.99	0.20	-12.99	9.74	-15.3	
Cerros del Rio basalts	Tb1	$log_{10}[m^2]$	-12.16	0.19	-12.16	0.53	-11	6.75
Cerros del Rio basalts	Tb2	$log_{10}[m^2]$	b	b	b	b	-12.2	0.4
Cerros del Rio basalts	Tb4	$log_{10}[m^2]$	b	b	b	b	-11.4	1.35
Santa Fe group - West	Tsf (west, xy)	$log_{10}[m^2]$	-13.24	0.16	-13.24	0.20	-13.2	0.16
vertical	Tsf (west, z)	$log_{10}[m^2]$	-15.04	0.43	-15.04	0.31	-13.9	0.53
Santa Fe group - deep	Tsf (deep,xy)	$log_{10}[m^2]$	-15.56	8.64	-15.56	208.28	-15.49	(fixed)
vertical	Tsf (deep,z)	$log_{10}[m^2]$	-15.56	(fixed)	-15.56	(fixed)	-15.49	(fixed)
Puye fanglomerate	Tpf	$log_{10}[m^2]$	-14.20	1.35	-14.20	2.99	-12.6	0.52
Puye Totavi Lentil	Tpt	$log_{10}[m^2]$	f	f	f	f	-13.52	11.02
Chaquehui Formation	Tsfuv (xy)	$log_{10}[m^2]$	-13.24	0.27	-13.24	0.33	-13.35	0.71
vertical	Tsfuv (z)	$log_{10}[m^2]$	-15.53	0.87	-15.53	2.04	-12.34	
Shallow Sangres	Frac. PC (1)	$log_{10}[m^2]$	-12.62	0.24				
Frac. PC - Ojo Caliente vicinity	Frac. PC (2)	$log_{10}[m^2]$	-13.07	0.58				
Frac. PC - Penasco vicinity	Frac. PC (3)	$log_{10}[m^2]$	d	d				

Agua Fria fault zone	AF fault	$\log_{10}[m^2]$	e	e				
Santa Fe group – East	Tsf (east,xy)	$\log_{10}[m^2]$	-14.08	0.41				
vertical	Tsf (east,z)	$\log_{10}[m^2]$	e	e				
Santa Fe group – Airport	Tst (SF, xy)	$\log_{10}[m^2]$	-12.58	0.79				
vertical	Tst (SF, z)	$\log_{10}[m^2]$	-12.58	(fixed)				
Santa Fe group – Pojoaque	Tst (Poj., xy)	$\log_{10}[m^2]$	e	e				
vertical	Tst (Poj., z)	$\log_{10}[m^2]$	e	e				
Ancha formation	Ancha (xy)	$\log_{10}[m^2]$	-12.26	0.51				
vertical	Ancha (z)	$\log_{10}[m^2]$	-12.26	(fixed)				
Santa Fe group – North	Tsc	$\log_{10}[m^2]$	-13.44	0.49				
Santa Fe - Ojo Caliente sandstone	Tso	$\log_{10}[m^2]$	-13.26	0.18				
Santa Fe - Penasco embayment	Tst (Pen)	$\log_{10}[m^2]$	-12.36	0.28				
Specific Storage	Sy	$\log_{10}[m^{-1}]$	-3.86	0.38	-3.86	0.59	-4.0	0.5

a combined with Santa Fe group –deep

b combined with Tb1

c combined with Paleozoic/Mesozoic

d combined with Frac. PC - Ojo Caliente vicinity

e combined with Santa Fe group – East

f combined with Puye fanglomerate

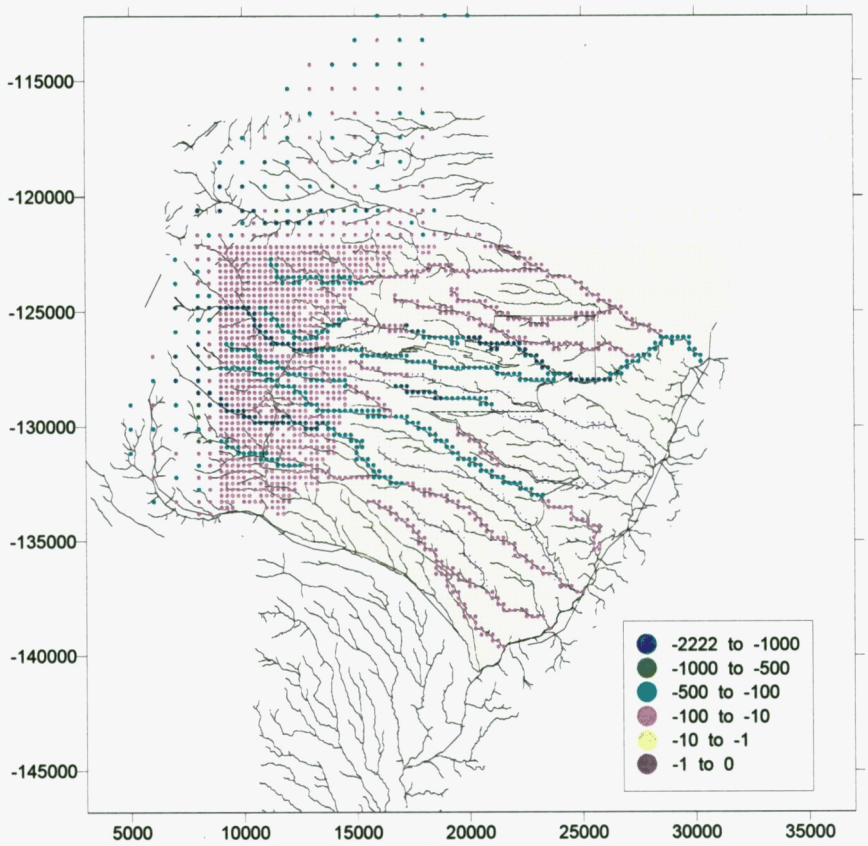

Figure 4-1. Recharge rates, in mm/yr

Figure 4-2 shows that for Santa Fe Group rocks (Tsf and Tsfuv), Totavi Lentil, and Tshicoma formation rocks, inverse model estimates are lower than field-based test data. The local, fixed recharge model estimates a very low permeability for the Tshicoma Formation; this permeability may be unrealistic and suggests that recharge rates in the western portion of the model are underestimated. For the Puye fanglomerate (Tpf) and Cerros del Rio basalts (model estimates for Tb4 are shown here), model estimates are near the average field-based estimate. Figure 4-3 shows the confidence limits associated with model estimates. These confidence limits demonstrate the degree to which the calibration data (water levels and fluxes) constrain the possible values of permeability. For all three models, estimates for the Tsf and Tb are quite reliable; estimates for Totavi Lentil are very uncertain. Of the two models with calibrated recharge rates, the basin model provides much parameters estimates with much greater degree of confidence. In particular, estimates for Tsfuv, Tpf, and Tt (Tschicoma Formation) are very good. The uncertainty in the estimate for the Puye Formation is much lower than was reported in

Keating et al. (Keating, Kwicklis et al. 2000), this improvement is due to the new water level data from the Puye collected in R-wells.

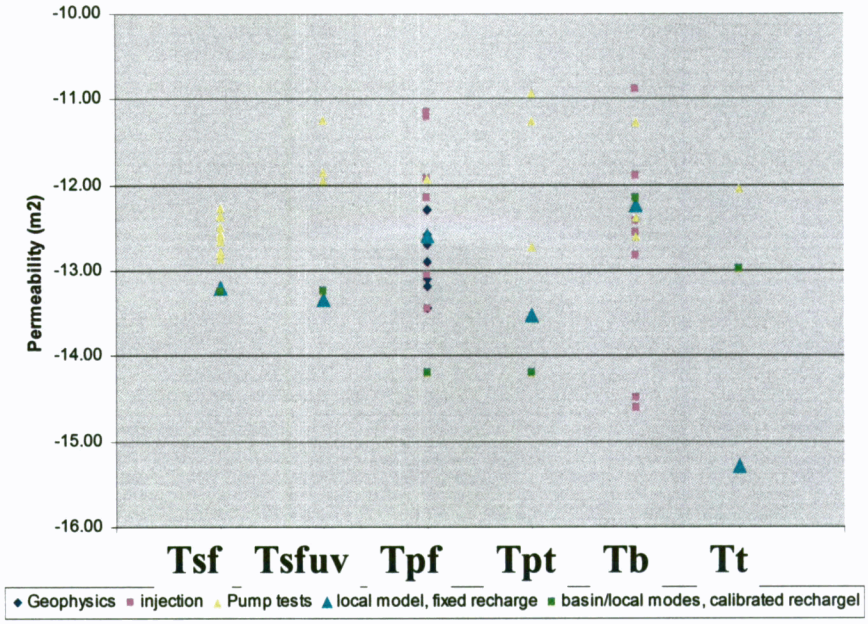

Figure 4-2. Inverse model estimates of permeability, compared to field-based estimates

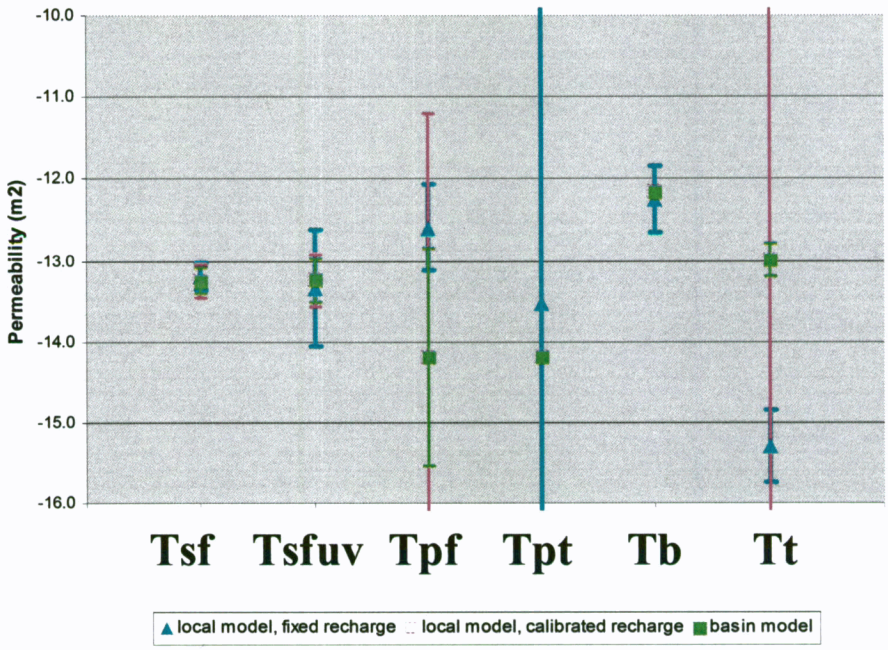

Figure 4-3. Confidence limits for inverse model estimates

The parameter estimates from the submodel, using an *a priori* distribution of recharge rates (Figure 4-1), differ from the other model estimates in several important ways. In general, since there are less parameters to estimate in this inverse model, we would expect that parameter uncertainty would be lower. This is generally true, particularly in the case of the Puye Formation where the parameter estimate has a one-order-of-magnitude 95% conference interval, falling well within the range of observed variability in the field-based estimates (Figure 2-5). The estimate for the Tschicoma Formation is very low (less than 10^{-15} m^2) and has very little uncertainty. This result is somewhat difficult to explain at present; we are currently investigating possible reasons.

Figure 4-4 shows the simulated present-day water table elevations, according to the submodel results (*a priori* recharge distribution). The purple dotted lines indicate the correct location of contours; the 1800m and 1750m simulated contours are too close together.

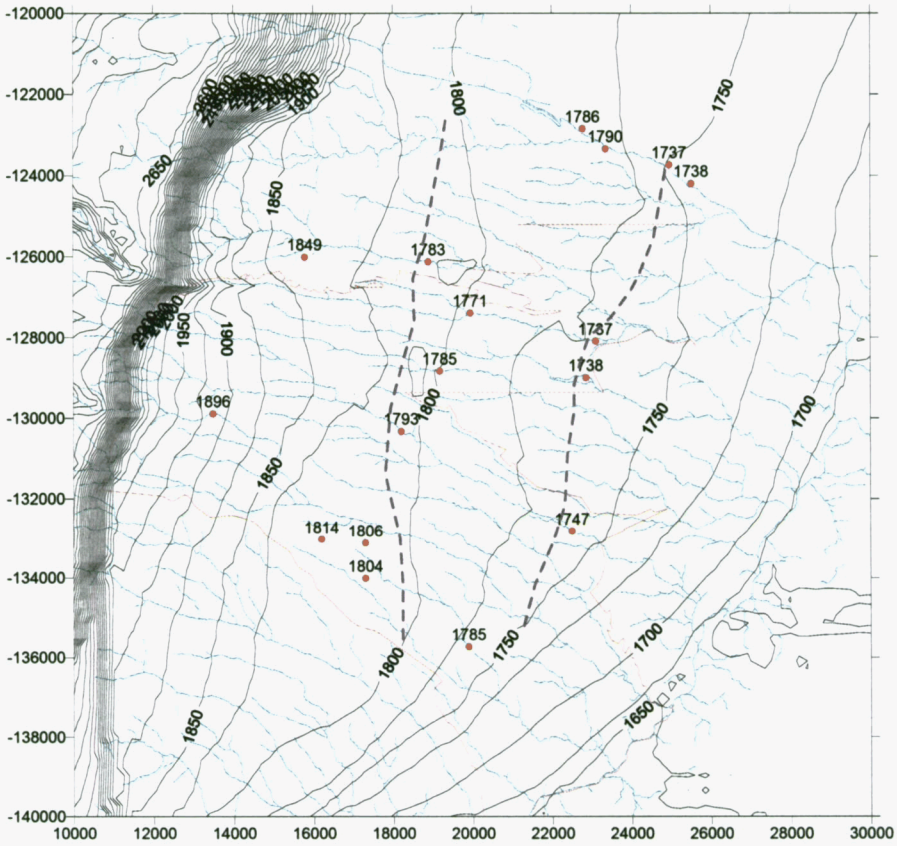

Figure 4-4. Simulated water table contours. Measured water levels are indicated next to red dots. Dotted lines show contours indicate locations of model error, where simulated and measured contours differ Contour interval = 25m

Figures 4-5,6, and 7 show simulated heads in three-dimensions. Figure 4-7 includes representative particle tracks. This figure illustrates the relatively complex flow paths that can be exist with relatively simple hydrostratigraphy. The flowpaths are strongly influenced by the Pajarito fault zone (low permeability) and the basalt flows (high permeability).

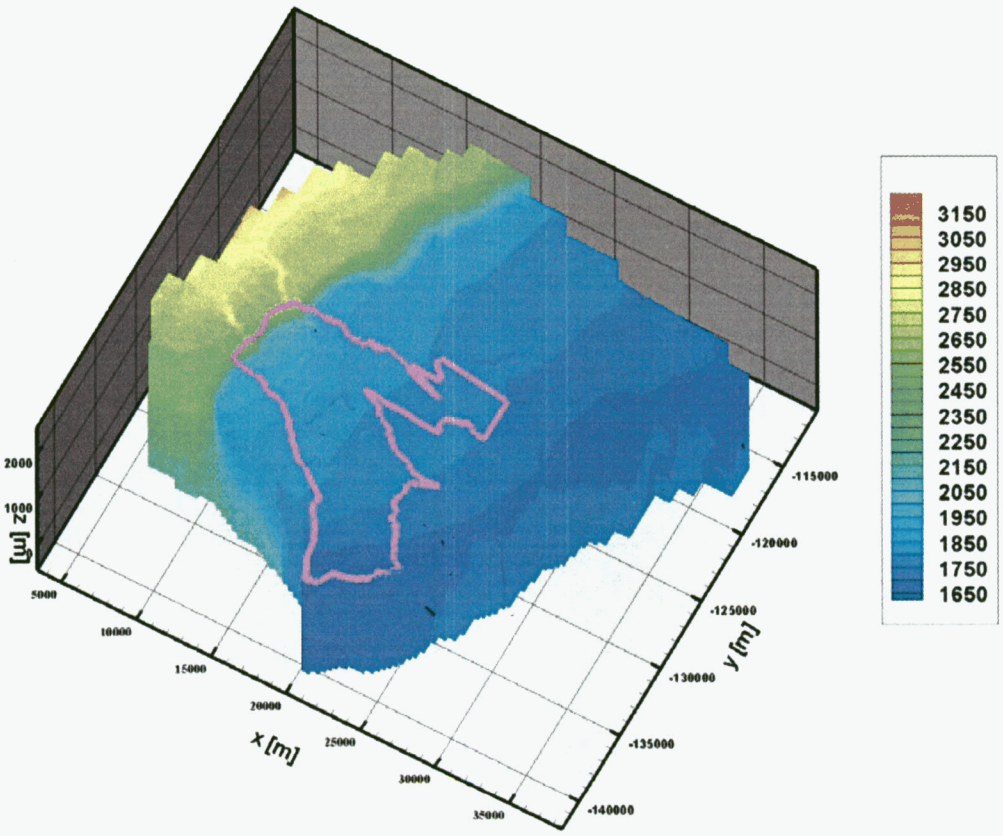

Figure 4-5. Simulated heads for local-scale model (2)

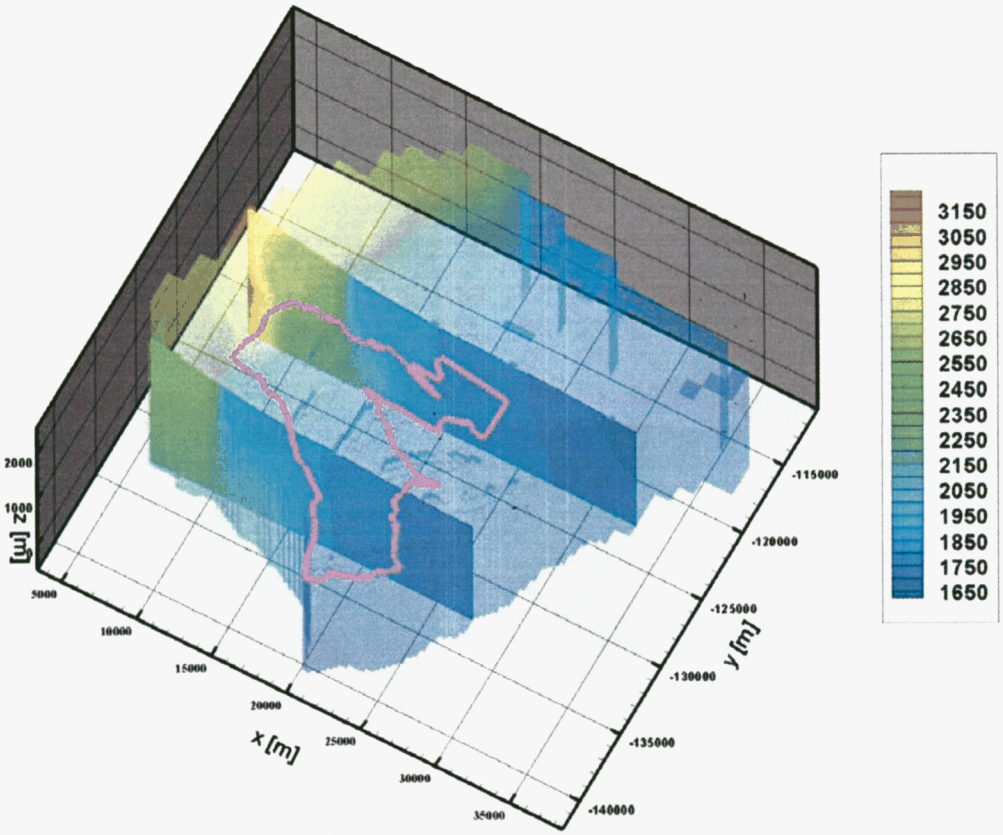

Figure 4-6. Simulated heads for local-scale model (2)

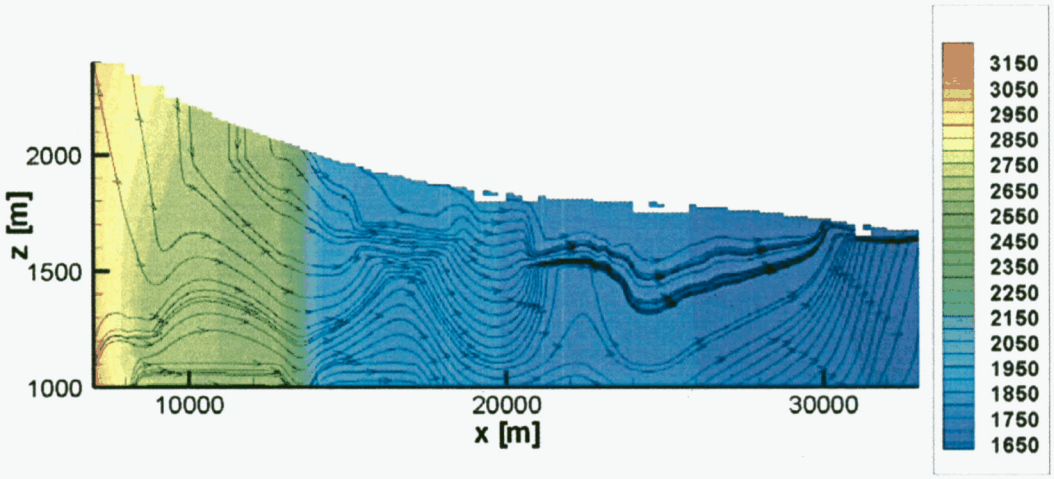

Figure 4-7. Cross-section of simulated heads (y=-123,000m), with representative particle tracks

4.3 Predictive Uncertainty

While it is important to evaluate parameter uncertainty (e.g. Figure 4-3), it is much more valuable to evaluate the impact of parameter uncertainty on key model predictions. Typically, sensitivity analysis (varying uncertain parameters, one-by-one) is used to accomplish this goal. However, sensitivity analysis results can be misleading if correlation between parameters is significant and/or if the model is extended out of the range of calibration. The predictive analysis capability within PEST searches for extreme values of the prediction of interest by varying all uncertain parameters while keeping the model in calibration.

Our first analysis was designed to evaluate the uncertainty in flow directions in the western portion of the aquifer. In this analysis, we posed two questions. For particles originating at the water table near R-25, what is the most northerly possible trajectory? What is the most southerly

possible trajectory? The predictive analyzer in PEST searched a wide range of parameter combinations to determine the answer to these questions, given the data available to the model (water levels, fluxes). The analysis, presented in Chapter 5, demonstrated that particle paths trajectories do not vary widely in plan view (flow directions range from slightly to the northwest to slightly to the southeast). However, significant uncertainty exists in the vertical direction; particles can either stay fairly shallow in the aquifer or travel quite deep. These two pathways have very different travel times and different discharge points (water supply well or Rio Grande). We tested various locations of "hypothetical" wells where new water level data could be collected to reduce the uncertainty in these predictions. This analysis demonstrated that knowledge of vertical head gradients in the vicinity of R-25 would be the most beneficial dataset. These data, which, in fact, do exist should be incorporated in a future update of this analysis.

Our second analysis was designed to evaluate the uncertainty in fluxes entering/exiting the aquifer beneath LANL. As described in Keating (2000) we use the fluxes predicted by the basin model to establish lateral boundary conditions to the submodel. We used predictive analysis to determine the minimum and maximum possible fluxes across the northern, western, and southern boundaries, given the information available to the basin model (water levels and discharge to the Rio Grande and its tributaries). Our methods and results are described in Chapter 6. Interestingly, this analysis suggests that the predictions of very little inflow/outflow across the northern and southern boundaries is very certain. No combination of parameters could be found that would place large fluxes across these boundaries and still honor water level and flux data. In contrast, there is large uncertainty in predicted fluxes across the western boundary. This uncertainty, however, proved to be insignificant in our ability to estimate travel times in the western portion of the aquifer. We expect this uncertainty to be more significant for model predictions that require estimates of solute concentrations

5 UNCERTAINTY IN GROUNDWATER FLOW DIRECTIONS

In a homogenous aquifer with primarily two-dimensional flow, it would be possible to derive flow directions from a potentiometric map (see Figure 2-1). However, due to the effects of vertical gradients (see Figure 2-2), heterogeneity within the aquifer (Figure 2-5), and the effects of municipal pumping, flow directions derived from such a simple approach may be quite misleading. Groundwater flow modeling offers the advantage of being able to incorporate these three-dimensional effects, yet model predictions such as flow directions will be uncertain due to a number of factors.

Our ability to estimate groundwater flow directions accurately is impacted by several types of uncertainty. The most important are 1) sparse water level and flux data, 2) uncertainty in hydrostratigraphy of the regional aquifer, and 3) uncertainty in permeability of the various hydrostratigraphic units. In the past decade, numerical tools have been developed to provide quantitative measures of the impact of (1) and (3) on model predictions. We have applied these tools to our predictions of groundwater flow directions; results are presented below. Unfortunately, quantitatively evaluating the effects of (2) is impossible at present, since our model of hydrostratigraphy (as expressed in the 3-D geologic model (Carey, Cole et al. 1999)) is deterministic. We hope in the future multiple working hypotheses can be incorporated into the 3-D geologic model and then the effect of hydrostratigraphic uncertainty can be included in our uncertainty analyses.

5.1 Model uncertainty

We have used inverse approaches to parameter estimation (see Keating (2000)), adjusting both recharge rates and permeability values to provide the best possible fit to water level data. This process provides parameter estimates that should be used as the basis for any model predictions, however, even more importantly it provides quantitative estimates of parameter uncertainty. Figures 5-1 through 5-3 show the predicted water level elevations for an inverse model result, along with model error calculations (colored dots in Figure 5-1, histogram of model errors in Figure 5-2 and Figure 5-3). The head errors are unbiased (see Figure 5-2), yet there are significant discrepancies between simulated and observed heads in several wells. These errors

are evidence of either errors in the permeability structure (overly simplified hydrostratigraphy and/or incorrect positioning of contacts between hydrostratigraphic layers) ,errors in the recharge distribution, or measurement errors (Carrera and Neuman 1986). We have been able to explore alternative models of recharge (smoothly increasing recharge rates with elevation; focused recharge along canyons) but have not been able to significantly reduce the errors in simulated heads. It is likely, therefore, that errors in the permeability structure (as defined by the 3-D geologic model) are the primary cause of these head errors.

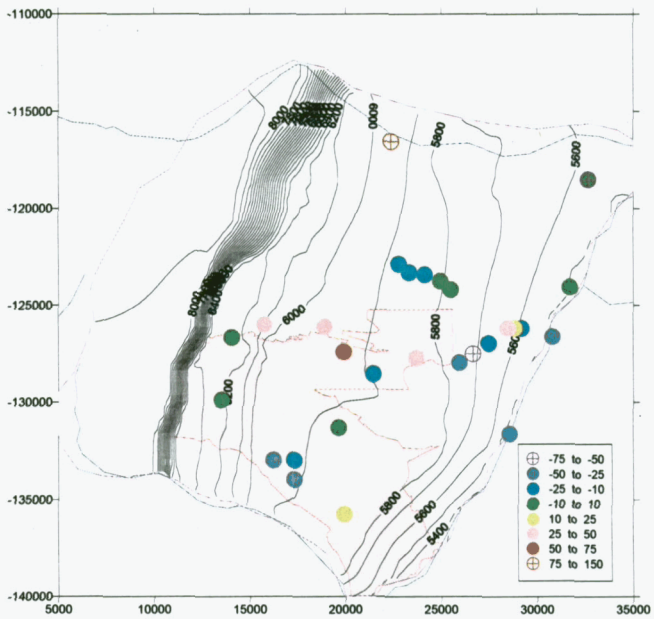

Figure 5-1. Simulated pre-development water table contours (in feet) and model errors at wells (simulated - measured)

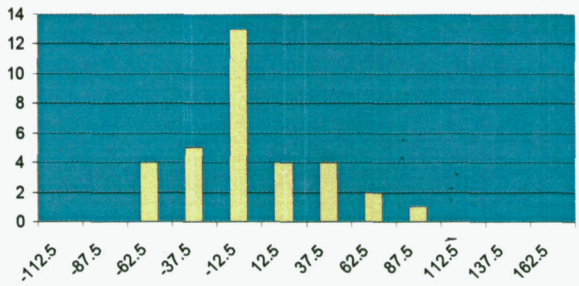

Figure 5-2. Distribution of model errors (simulated - observed)

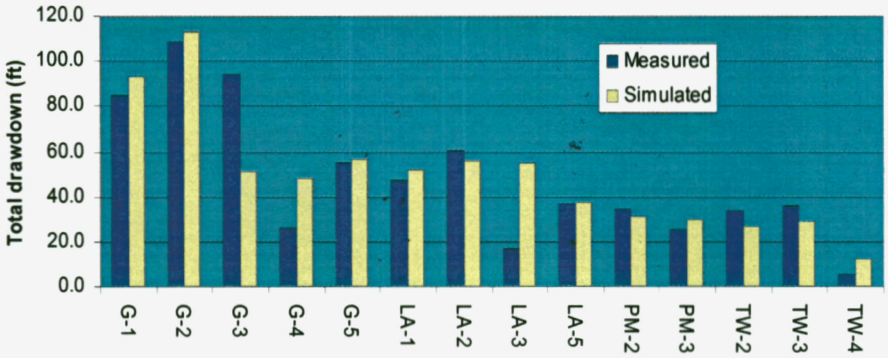

Figure 5-3. Histogram of model errors for drawdowns due to pumping (simulated - observed, in feet)

Parameter estimates derived from model calibrations are shown in Figure 5-4. These results suggest that the permeability of the Santa Fe Group is fairly well constrained by water level data, particularly transient data. Far more uncertainty is present in permeability estimates for the Puye Formation and Tb4.

5.2 Impact of parameter uncertainty of predicted flow directions

It is unclear how the parameter uncertainty indicated in Figure 5-4 impacts our predictions of groundwater flow directions. We have estimated uncertainty in the model predictions by constrained nonlinear optimization of our inverse model (e.g. Vecchia and Cooley, 1987) using PEST. The predictive algorithm searches for the maximum/minimum in the model prediction within pre-defined limits of the objective function. The analysis allows efficient way to determine the impact of parameter uncertainty on the model predictions. It differs from the sensitivity analysis of model predictions in respect to model parameters, which considers only the calibrated parameter set and assumes that the model is linear.

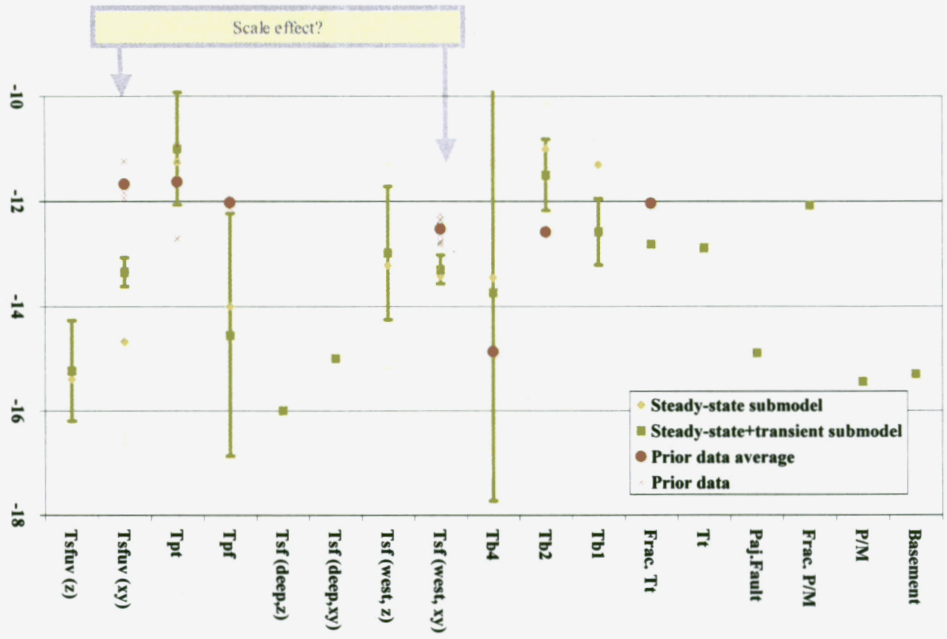

Figure 5-4. Inverse estimates and prior data of permeability

5.3 Theoretical basis

There are many possible factors which may affect the reliability of model predictions: conceptual model errors, parameterization errors, discretization (grid-resolution) errors, uncertainty in parameters. Due to low model sensitivity and correlations among parameter estimates there may be multiple parameters sets that produce equally-well calibrated results (as measured by our objective function), but provide quite different predictions. Our method for estimating uncertainty in the model predictions utilizes constrained nonlinear optimization (e.g. Vecchia and Cooley, 1987); this method is available in the parameter estimation code, PEST (Doherty 1997). The predictive algorithm searches for the maximum/minimum in the model prediction within pre-defined limits of the objective function. The analysis allows efficient way to determine the impact of parameter uncertainty on the model predictions. It differs from the sensitivity analysis of model predictions in respect to model parameters, which considers only the calibrated parameter set and assumes that the model is linear. Let the objective functions is defined as:

$$F = [c - f(b)]_T Q[c - f(b)]$$

where c is a vector [N×1] of optimization targets, b is a vector [M×1] of model parameters, Q is a cofactor matrix [N×M], and f is our model. Let f' is the same model under predictive conditions, and the prediction p is defined as

$$p = f'(b)$$

We search for b such that maximizes/minimizes p subject to

$$[c - f(b)]_T Q[c - f(b)] = \partial F_{\min}$$

where F_{min} is defined for the maximum-likelihood estimates b_{ML}. For the maximum-likelihood case,

$$\delta = \frac{N}{N-M} F_{\alpha}(N, N-M) + 1$$

where F is the F distribution. The nonlinear constrained optimization can be replaced by iterative solving of Lagrangian problem as proposed by Vecchia and Cooley (1987).

5.4 Application to flow direction uncertainty

We applied this method to analyze uncertainty in flow directions downgradient from R25. We define the model "prediction" in this case to be the y value of the predicted particle trajectory as it passes x=18290. Using the methodology described above, PEST searches for the combination of parameters which simultaneously produce an acceptable match with calibration criteria (heads and flux measurements) and produce a maximum (or minimum) value of the prediction.

Figure 5-5 and Table 5-1 show the results of this analysis. The best "calibrated" model predicted a particle trajectory indicated by the purple line (particle is captured by PM-2). Parameter combinations that produces the most northerly and most southerly departures from this line are indicated by blue and red lines. The values of permeability used to obtain these three particle paths are shown in Figure 5-6. The water table elevations predicted by the models for these two pathways are indicated by black and blue contour lines. It is interesting to note that despite fairly large difference in water table elevations (see difference between blue and black 1750m contour line) groundwater flow directions do not vary substantially. It is also interesting to note that even small differences in flow direction can change the predicted discharge location (either water supply well PM-2 or the Rio Grande).

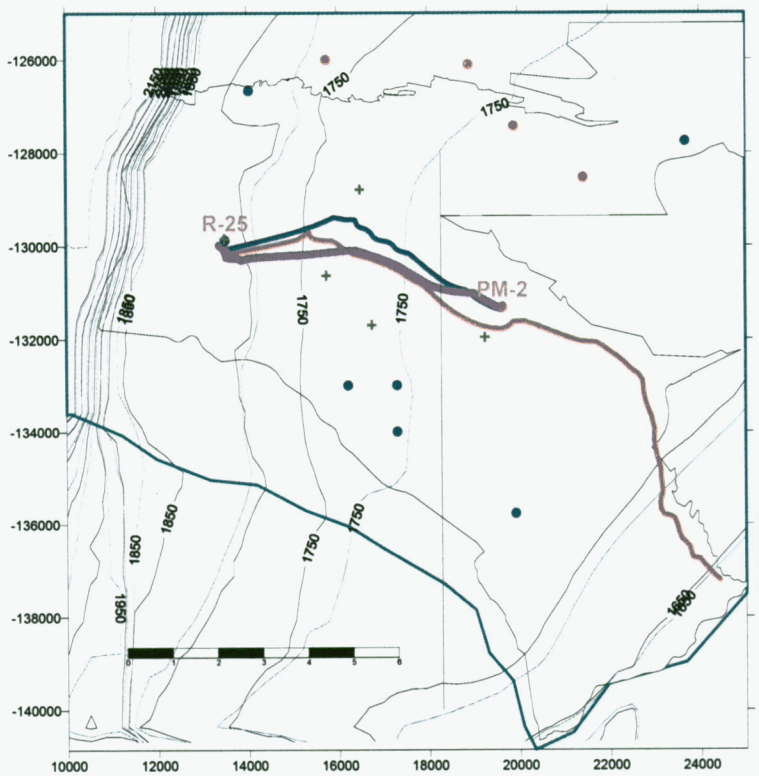

Figure 5-5. Particle trajectories that correspond to the maximum and minimum y value at x= 18290. Blue dots are wells used in steady-state (predevelopment) calibration; red dots are wells used in transient calibration. Green x's are locations of hypothetical wells

.

Table 5-1. Results of predictive analysis

	Inverse model	Objective function (Φ)	Predicted Y (m)	Predicted travel time (to x=18290)	Predicted travel time (total)
Optimized	Optimized	5.85E+4	131001	1,424	1445
Predictive analyst	Minimum 1	7.98E+4	131448	1,425	1629
	Maximum 1	7.27E+4	130937	1,774	1785

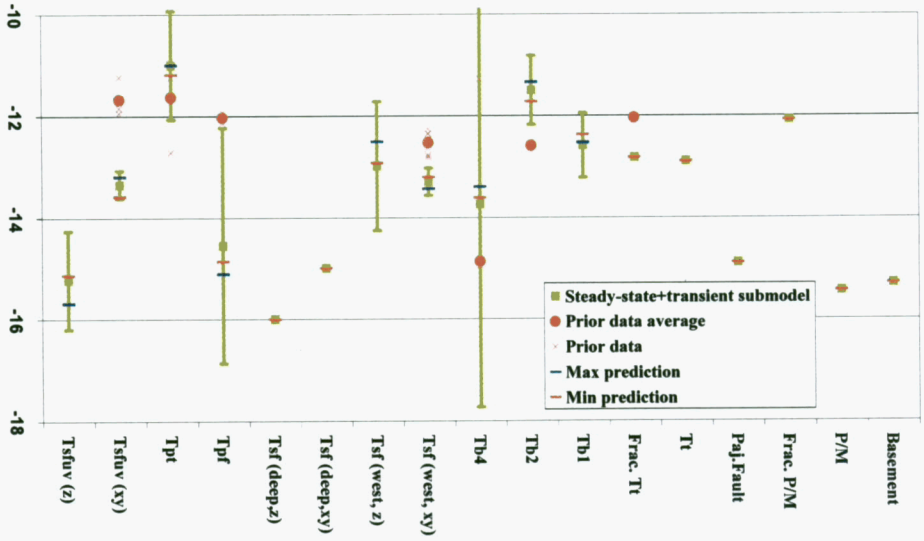

Figure 5-6. Model parameters. Calibration results shown in green; parameters corresponding to mimum and maximum predictions shown in red and blue

Figure 5-7 illustrates that despite relatively constrained flow directions, the rock types that the particles pass through are quite different. The more northerly trajectory enters the Los Alamos aquifer (Tsfuv) as it flows east; the southerly trajectory enters the Puye Formation. This difference could have substantial impact on contaminant transport, if effective porosity and geochemical characteristics of the two rocks types were different.

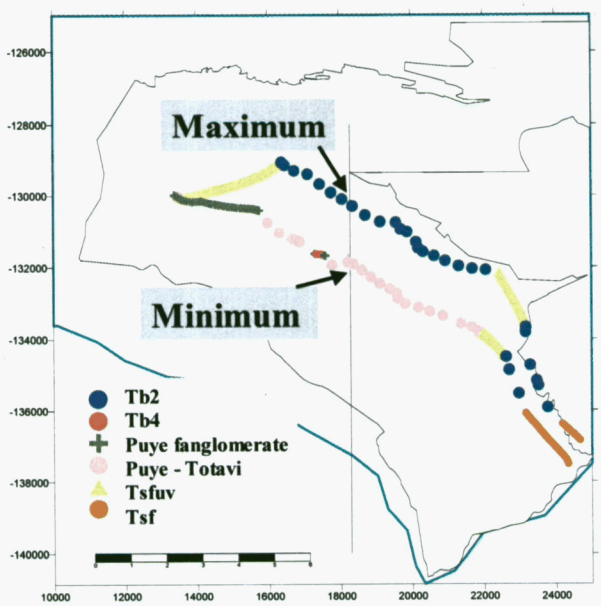

Figure 5-7. Types of rocks particles travel through.

Figure 5-8 shows the particle paths in cross-sectional view. This view illustrates that the two path differ substantially in the vertical direction. The pathway that goes deeper (corresponding to maximum Y) travels much slower than the shallow pathway.

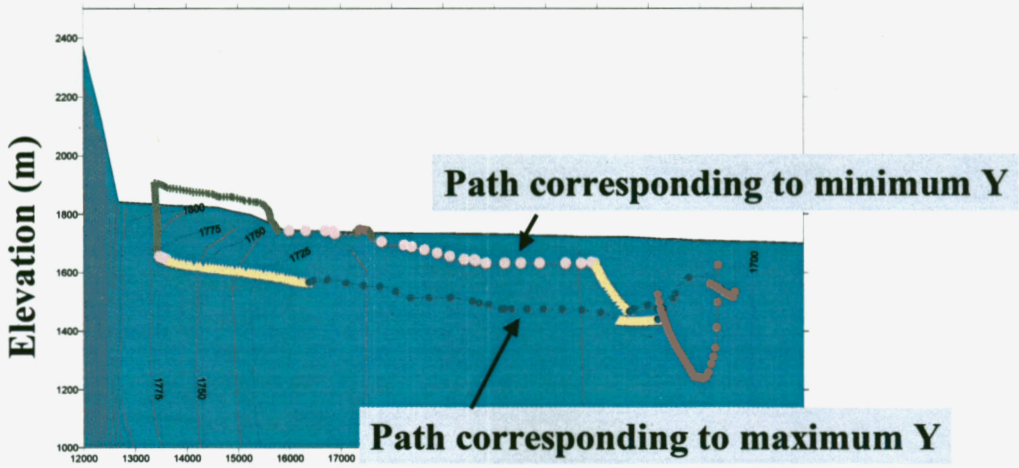

Figure 5-8. Cross-sectional view of particle paths

5.5 Benefit of new data to reduce model uncertainty

We used a very simple method of analysis to determine what locations new wells could be placed to most reduce the uncertainty in our predicted flowpaths. We proposed 5 well locations (one exactly at R25), indicated by green markers in Figure 5-5. Four of these wells are multiple completion wells. The R25 well is considered "hypothetical" for the purposes of this analysis because at the time of the analysis (November, 2000) water level data from all the R25 screens were not available to us. We used the calibrated model to define the "measured" heads

For each of the hypothetical locations (and depths of screens below the water table) we determined the sensitivity of the predictions to the head measurements at these locations. This is a simple way to evaluate how important a measurement would be to the model prediction. Figure 5-9 shows the calculated sensitivities. The sensitivity of maximum prediction does not show a strong spatial pattern; many of the locations and depths are approximately equally important. In contrast, the sensitivity of the minimum prediction is much more sensitive to heads at R25 (dw4) than to heads at any other location.

Another comparison is shown in Figure 5-10. This figure shows the error in simulated heads for the hypothetical wells. (Error = 0 for calibrated model). The greatest benefit should be in locations where the simulated head is quite different between the two models. According to these results, this location is R25 (dw4).

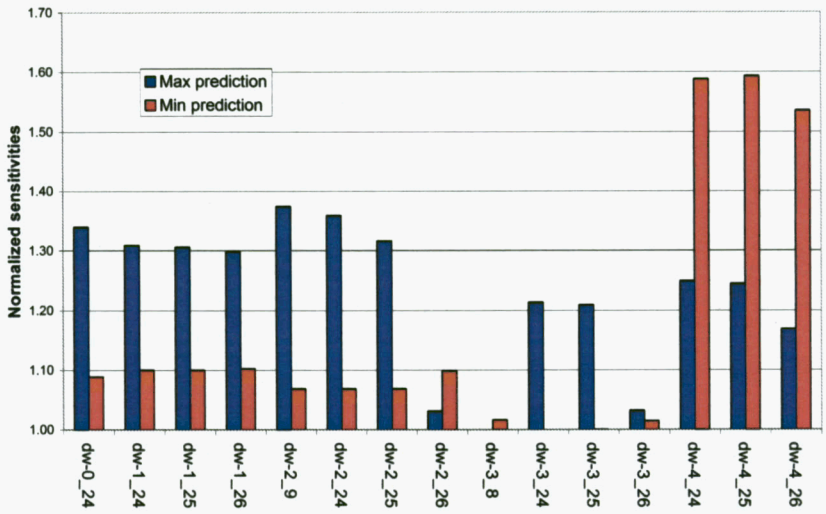

Figure 5-9. Sensitivity of model predictions to head measurements in hypothetical wells

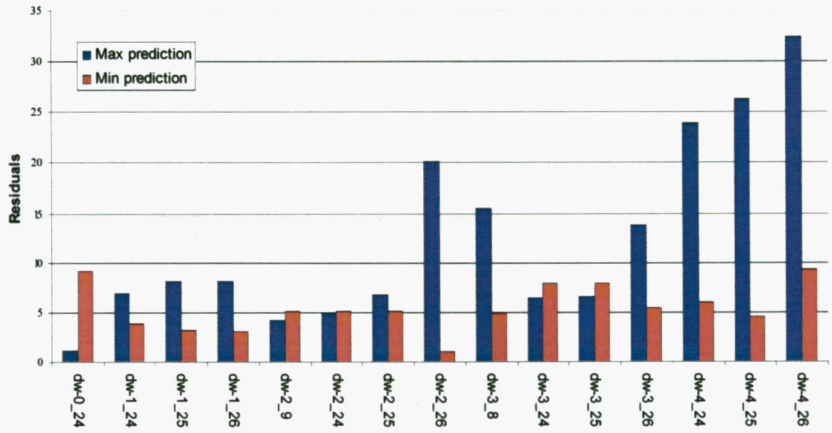

Figure 5-10. Residuals (simulated - observed) for the two models

5.6 Summary

There are several important implications of this analysis. The uncertainty in lateral groundwater flow directions downgradient of R25 *due to model parameter uncertainty* is fairly low. Other sources of uncertainty (errors in hydrostratigraphy, conceptual model errors, etc.), while potentially important, are difficult to evaluate.

Although the easterly flow direction is fairly well-constrained by existing water level data (model calibration targets), vertical flow directions are less well constrained. In addition, even small differences in flow paths can determine whether or not a particle is captured by a supply well. There is also substantial uncertainty as to which rock units the water will flow through. If significant differences exist in the transport characteristics of these rocks, this uncertainty could have a big impact on predictions of contaminant transport.

These analyses were performed before the addition of recent R-well data into the model calibration process. Presumably, if the analyses were repeated today there would be a somewhat smaller range of possible flowpaths. For the most accurate results, these analyses should be repeated with the most current water level data set and updated 3-D geologic model (when it becomes available).

6 UNCERTAINTY IN LATERAL FLUXES TO AQUIFER BENEATH LANL

We used predictive analysis to determine the degree of uncertainty present in our ability to estimate lateral fluxes to the aquifer beneath LANL. The source of uncertainty we considered were parameter uncertainty in the basin model (permeability of all hydrostratigraphic units and recharge model parameters). The predictive analyzer found the minimum and maximum fluxes across submodel boundaries that were consistent with water level and flux (baseflow to rivers) calibration targets.

The following paper describes this work; it was presented at a groundwater modeling conference in September 2001, was published in conference proceedings (Keating, Vesselinov et al. 2001), and has been requested for January 2002 submission for publication in a special issue of Journal of Groundwater, publication of National Water Well Association.

Coupling a large-scale basin model with a high resolution local model using a finite-element flow and transport solver (FEHM) and an automated parameter estimator (PEST)

Elizabeth Keating, Velimir V.Vesselinov, Ed Kwicklis, and Zhiming Lu

6.1 Abstract

In support of the hydrogeologic characterization program at LANL we have developed a groundwater model of the Española Basin in Northern New Mexico. This large-scale model takes advantage of regional water-level and stream-flow data and provides reasonable constraints on fluxes through the aquifer beneath LANL. However, even using selective grid refinement in the vicinity of LANL we were unable to achieve the fine discretization required to support local, high-resolution transport simulations. We extracted a sub-model from the basin model for the LANL site which has finer vertical resolution in the most shallow hydrostratigraphic units which are very heterogeneous. We use automated parameter estimation (PEST) to calibrate both models and independently estimate medium properties and aquifer recharge. We couple the basin- and local-scale models through flux specification at sub-model lateral boundaries. Using predictive analysis, we are able to estimate the uncertainty of these fluxes within specified calibration criteria. The calibrated sub-model was used to simulate advective transport of high explosives

through the aquifer. The sub-model grid resolution is sufficient to allow geostatistical characterization of the medium properties within those hydrostratigraphic units important to transport predictions. Transport results were shown to be relatively insensitive to the uncertainties in lateral fluxes across sub-model boundaries, but sensitive to the uncertainties in model parameters.

6.2 Introduction

In our efforts to evaluate groundwater flow directions and velocities in the deep aquifer beneath Los Alamos National Laboratory on the Pajarito Plateau in northern New Mexico we face a scale problem that is inherent to many groundwater investigations. In order to capture the significant details of sedimentary hydrostratigraphy at the site scale, we must build a flow and transport model with very fine grid resolution, particularly in the vertical direction. Due to computational limitations, this high resolution requirement prevents us from extending the spatial extent of the model to natural hydrologic boundaries (in our case, the margins of the Española Basin). Therefore, we must impose lateral model boundaries which are closer to the area of interest than we would like and our transport results may therefore be very sensitive to the boundary conditions we apply. In this paper we discuss a process of linking a basin-scale model (relatively low grid resolution) to a site-scale submodel (relatively high grid resolution) to provide better constraints on sub-model parameterization and boundary condition specification than would be possible using the site-scale model alone. We are particularly interested in evaluating the uncertainty associated with the flux estimates provided by the basin-scale model, in order explore fully the range of possible boundary conditions to the lateral boundaries in the sub-model. Using transport calculations from the sub-model as a measure of model sensitivity, we can then assess the importance of the uncertainty in fluxes at model boundaries.

6.3 Model development

3-D flow and transport models for the basin and submodel have been developed using FEHM (Finite Heat and Mass Transfer Code (Zyvoloski, Robinson et al. 1997)); computational meshes were generated using LaGriT (Trease, George et al. 1996) (see Figure 6-). Hydrostratigraphic zonation was established according to a geologic framework model (Carey, Cole et al. 1999)

constructed using Stratamodel (Landmark 1998) (see Figure 6-). Major rivers within the basin are simulated as specified head. Most lateral boundaries in the basin model are specified as no-flow.

The lateral boundaries of the submodel were chosen to correspond to hydrologic features (north and south boundaries: perennial stream channels; western boundary: topographic divide, eastern boundary: Rio Grande). It is possible that all of these boundaries are approximately no-flow; however, because of sparse water level data the fluxes are uncertain and we would like to evaluate the impact of this uncertainty on transport calculations within the sub-model. Presently, we are only evaluating the impact of uncertainty in flux estimation across the northern, western, and southern boundaries. Since the Rio Grande is the regional discharge boundary, the vertical boundary parallel to the river is assumed to be no-flow, except at the surface where constant head nodes allow groundwater/surface water exchange. Along this boundary, sufficient water level data is available to suggest that a groundwater divide exists, thus lending credence to the no-flow assumption.

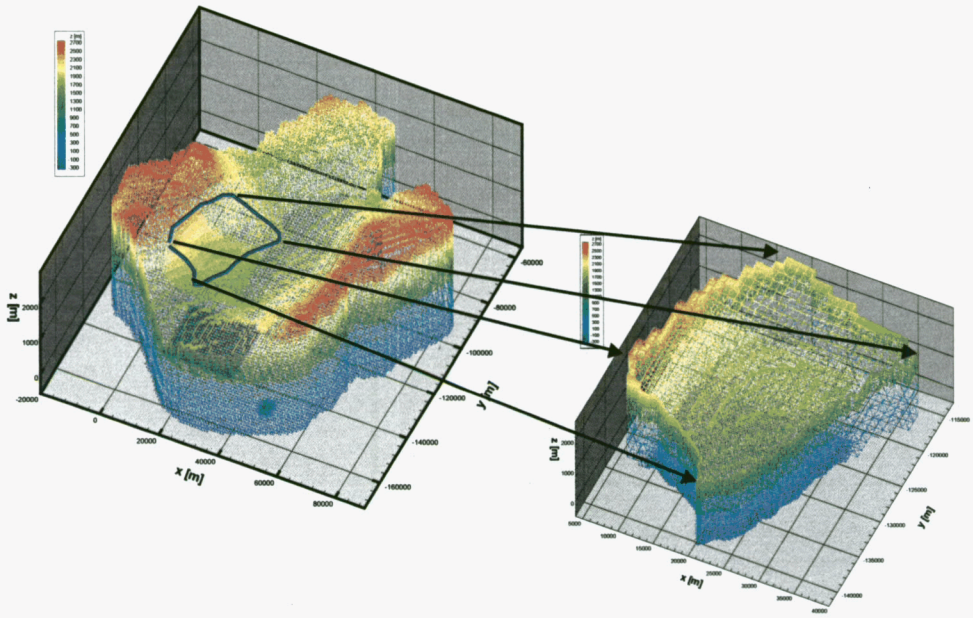

Figure 6-1. Computational grids.(left: Española Basin, right: sub-model of Pajarito Plateau

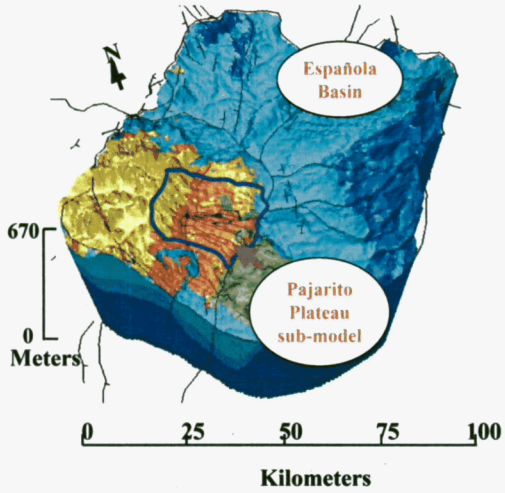

***Figure 6-2**. Hydrogeologic framework model.*

We use the basin model to estimate fluxes between each pair of nodes that crosses the surfaces defining the lateral boundaries of the submodel. These fluxes cannot be mapped directly onto the submodel boundaries because of the increased grid resolution in the submodel. Our mapping algorithm preserves the total flux across the boundary and the proportion of that flux that flows through each hydrostratigraphic unit in the models. Within each hydrostratigraphic unit, we allow small discrepancies between the spatial distribution of fluxes predicted by the basin model and those applied to the sub-model boundary.

6.4 Parameter estimation

Using PEST (Doherty, Brebber et al. 1994), we have estimated both aquifer recharge rates and permeability, k, of the various hydrostratigraphic units for both the basin and sub-models. The details of our procedure and results are described in Keating et al. (2000). To a large extent, we have decoupled the parameter estimation process for the two models. One reason for this is that by doing so we can learn to what extent grid resolution and scaling effects (in the case of permeabilities) influence the parameter estimation process. In addition, by allowing the recharge rates to differ between the two models we can determine the degree to which local recharge patterns may differ from regional trends.

For each model, we have used two different approaches to parameter estimation. The first approach is based on an inverse steady-state model representing the "pre-development" (with no significant withdrawals) aquifer condition. We evaluated the model parameters as well as their uncertainty and sensitivity, given the pre-development water levels (93 basin-wide, 34 of which fall within the sub-model boundaries) and flux estimates along rivers (10 reaches). The second inverse approach combines a steady-state and a transient models. Since 1945, the water levels have declined due to intensive development of the aquifer. To incorporate this information in the calibration process, we developed a new inverse model that estimates the parameters simultaneously against (1) steady-state "pre-development" data (as described above) and (2) the transient drawdowns due to the pumping. The steady-state+transient inverse model includes one additional parameter, the specific yield, which, for the moment, is defined to be equivalent for all the hydrostratigraphic units. The transient data is available for each year since 1945 in 14 wells on the Pajarito Plateau. For the moment, to increase the computational efficiency, we performed the transient simulations using not 1 but 10 year time steps. To do so, ten-year average pumping rates were derived from the annual pumping data for all the wells in our model.

6.4.1 Steady-state basin model results

The steady-state basin inverse model estimated 37 model parameters which include 3 recharge parameters and 34 permeabilities . The residuals between simulated and observed measurements are unbiased (centered around zero) but clearly not normally distributed. Our parameter estimation errors ranged widely; for example, the permeabilities of the two largest hydrostratigraphic units in the basin were very well constrained; estimates for several smaller units were very poorly constrained. We were able to demonstrate that the high uncertainty is predominantly due to the cross-correlations of estimation errors rather than low parameter sensitivities to the observations. We also compared the *k* estimates to data derived from pump tests, which were not included in the model calibration process. For most units, the pump-test *k* values are very close to the estimates or within their uncertainty limits. For some units, including several important units on the Pajarito Plateau, pump-test k values were significantly higher than inverse estimates. The inverse *k* estimates and the pump test *k* data represent the rock properties at very different scales. The *k* estimates represent the large-scale effective

permeabilities for the whole rock unit, while the *k* data is defined from small-scale field tests representing rock properties in the close vicinity of test boreholes. We should also take into account the fact that the pump test *k* data is predominantly collected from water supply wells which are placed in highly permeable portions of the aquifer in order to achieve higher pumping rates. Therefore, the pump test *k* data could be biased towards higher estimates. Another possible source of inconsistency is in the conceptualization of hydrogeologic conditions not only in the numerical model but also in the pump test analyses.

6.4.2 Steady-state sub-model results

The sub-model calibrations were only partly dependent on basin-model calibration results. As described above, we use basin-model results to apply fluxes at sub-model lateral boundaries. For reasons of simplicity, during the sub-model calibration process we did not allow these flux estimates to vary. A more rigorous approach could be developed which would consider the effects of permeability changes on flux estimation. We also examined two alternative approaches concerning the recharge. The first approach assumes that the basin model calibration will produce the most reliable recharge estimates, since the basin model provides the best possible constraints on global water balance. Thus, the recharge model parameters are taken from the basin model results and applied directly to the sub-model. The second approach assumes that the recharge rates on the Pajarito Plateau might be different than "average" rates at the basin-scale and thus recharge parameters are re-estimated for the sub-model.

The steady-state inverse sub-model estimated 20 model parameters which include 3 recharge parameters and 17 permeabilities . Sub-model and basin-model permeability estimates are very similar; the largest discrepancies are for two relatively small hydrostratigraphic units. For one of these, the sub-model estimate was closest to the pump test data, for the other, the sub-model estimate was the farthest. More importantly, however, the two models obtained substantially different recharge parameters. Since both models provided reasonable simulation of the head and flux measurements it is impossible to discriminate between these two recharge models at this point.

6.4.3 Transient results

The addition of transient observations in the inverse process improved significantly the uncertainty of estimated parameters. For the sub-model, the steady-state+transient inversion allowed an improvement in the steady-state flux and water level matches. The steady-state model failed to converge to a global minimum due to the high cross-correlations between the estimation errors. We have demonstrated that these cross-correlations have been significantly decreased by the addition of the transient data. A comparison between the steady-state and steady-state+transient estimates shows that the major changes are associated with the *k* of two potentially important hydrostratigraphic units. The uniform specific storage estimated by the transient inverse model is close to independent estimates derived from hydraulic testing.

6.5 Uncertainty of fluxes across lateral boundaries of the submodel

As described above, using the calibrated basin model we estimated fluxes into/out of three lateral boundaries of the submodel (north, south, and west). However, due to parameter uncertainty our calibrated model is non-unique and thus these flux estimates are also uncertain. One way to address this problem is through sensitivity analysis. However, sensitivity analysis of basin-model parameters to the flux predictions across the sub-model domain boundaries provides us only with information about the degree of dependence between the parameters and the predictions in the close vicinity of the optimal estimates. Therefore, sensitivity analysis has limited applicability due to non-linearity of the forward problem and the cross-correlations between estimates. A better approach is prediction analysis, which does not depend on these assumptions and allows estimation of a set of model parameters which not only reproduce observations within a specified tolerance but also maximization/minimization of the analyzed predictions. We used the predictive analysis capability within PEST to estimate the maximum and minimum fluxes across each of these three boundaries that could be achieved by varying parameters while still requiring the model to meet specified calibration criteria.

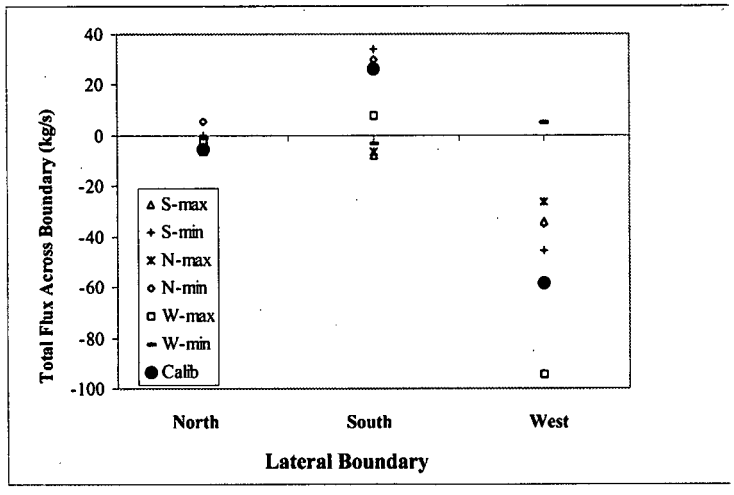

Figure 6-2. Predicted maximum and minimum fluxes acr across three lateral boundaries

We performed six predictive analyses, searching for the maximum and minimum total flux across each of the three boundaries. Figure 3 shows the resulting range of predictions, all compared to the "best calibration" result (solid circles). This figure illustrates the relatively low degree of uncertainty for the predicted north and south fluxes and the relatively high degree of uncertainty for the predicted flux across the western boundary, it is interesting to notice that the predicted fluxes across these boundaries are generally negatively correlated (e.g. large flux along one boundary tends to be associated with small flux along the other two), reflecting the degree to which flux calibration targets are constraining the range of possible results.

6.6 The influence of flux uncertainty on transport calculations

Using the calibrated sub-model, we simulated advective transport of dissolved high-explosives away from a contaminated site near the western boundary of LANL. We used the particle tracking capability within FEHM to estimate pathways and travel times through numerous of stochastic realizations of the Puye Formation (Keating, Kwicklis et al. 2000). Elsewhere, we have demonstrated (Keating et al., 2000) that the travel times are very sensitive to the uncertainty in the model parameters (recharge and permeability). Here, we investigate sensitivity to fluxes at model boundaries. Table 6-2 presents the predicted mean travel time for HE "particles" to reach the Rio Grande, assuming different flux boundary conditions, all using a

Table 6-1. Mean travel times

Boundary condition	Mean travel time (yrs)
N-max	750
N-min	882
S-max	730
S-min	866
W-max	643
W-min	871

single realization of the Puye Formation. Overall, we find that the predicted travel times are relatively insensitive to the uncertainty in fluxes at the boundaries; much less sensitive than to uncertainty in model parameters. This result will allow us to focus future sensitivity analyses on parameter uncertainty and to emphasize data collection that will provide the most reduction in parameter uncertainty. In future contaminant transport calculations, to provide conservative predictions (i.e. "worst case" scenarios) we must apply the W-max boundary condition.

7 HYDROLOGIC DATA COLLECTION PRIORITIES FOR REGIONAL AQUIFER CHARACTERIZATION

This summary attempts to provide an overview of outstanding data needs regarding 1) *groundwater flow directions* and *velocities*, and 2) contaminant transport in the regional aquifer; however, we emphasizes data needs regarding (1). This emphasis is reasonable since it addresses basic characterization requirements and also gives us the necessary information to predict migration of highly mobile contaminants which could pose the greatest threat to water quality. Characterization of aquifer properties that control retardation of contaminant migration (essential to (2), for some contaminants) is best addressed on a site- and contaminant-specific basis and is outside the scope of this document.

There are four types of data that should be collected from R-wells so that groundwater flowpaths and velocities can be better defined in the regional aquifer: head, permeability, storativity, and porosity. A fifth type of data, flux data, is important as well. The guiding principles for setting priorities are to emphasize measurements in the following categories: 1) the "least well characterized" hydrostratigraphic unit(s), 2) the units where fluxes and/or velocities are potentially the greatest and therefore most important for transport, and 3) the locations where spatial data coverage is poor.

7.1 Flow directions

Flow directions in the regional aquifer are determined by hydraulic gradients and permeability variations within the aquifer. Variations in both gradients and permeability are expected to be scale-dependent. Characterizing large-scale flow directions (at the scale of the LANL site: kilometers to tens-of-kilometers) is the highest priority; followed by medium-scale flow (hundreds to thousands of meters). The importance of quantifying small-scale variations (tens to hundreds of meters) should be evaluated on a case-by-case basis according to site-specific monitoring and/or environmental restoration issues.

7.1.1 Permeability characterization

Figure shows the current estimates for large, medium, and small-scale permeability for various hydrostratigraphic units within the regional aquifer. Each category is discussed separately below.

7.1.1.1 Large-scale permeability variations

The best indicators of large-scale permeability variations (over 100's to 1000's of meters) are water level responses to long-term pumping, spatial variation in water levels across the plateau, and multi-hole pump tests. No multi-hole pump tests have been conducted to date.

If the total flux of water through the aquifer is reasonably well-known, water level data can be analyzed using a numerical flow model to estimate large-scale permeability of hydrostratigraphic units within the aquifer. Analysis of historical streamflow data along the Rio Grande has provided both an estimate of mean flux and associated uncertainty. Combining this flux information and water level data (both present and historical) with our flow model for the aquifer, we have estimated large-scale permeability of the major aquifer units. For the sedimentary rocks, there are relatively small differences between units (less than one order of magnitude). .

Unit	Estimated permeability (m^2)	95% Confidence Limits	Model
Santa Fe Group (lower)	13.32	+/- 0.16	Local (2)
Santa Fe Group ("Los Alamos aquifer")	-13.4	+/- 0.71	Local (2)
Puye Formation - fanglomerate	12.6	+/- 0.52	Local (2)
Basalts	-12.16	+/-0.19	Basin

7.1.1.2 Medium-scale permeability variations

Our estimates of medium-scale permeability are derived from single-hole pump tests in water supply wells screened over ~2000'. These estimates are representative of the rock within

within tens of meters to a few hundreds of meters of the boreholes. Estimates are only available for the Santa Fe Group (both lower and "Los Alamos Aquifer" facies). Other units such as basalts and Puye were present in many of these boreholes; the effect of these units on test results is unknown.

Unit	Mean permeability (m^2)	Max/Min	Number of tests
Santa Fe Group (lower)	-12.5	-12.26/-12.84	12
Santa Fe Group ("Los Alamos aquifer")	-11.2	-11.94/-11.67	3

These estimates are noticeably higher than the large-scale estimates (described above). Possible reasons for this discrepancy are 1) large-scale features that single-well pump tests cannot detect, such as low-permeability faults (trending N-S), 2) the fact that pump test data are entirely derived from water supply wells, which may have been purposely sited in relatively high-permeability zones within the Santa Fe Group, and flow model errors such as 3) underestimation of total flux through the aquifer, and/or 4) overestimation of the total thickness of the aquifer. We are using sensitivity analyses to evaluate the plausibility of (3) and (4); preliminary results indicate that neither of these factors can explain the discrepancy. Additional pump test data, particularly 2 or 3-hole pump tests, are needed to evaluate (1) and (2). These data clearly suggest that there are relatively high-permeability zones within the Santa Fe Group. At present, we do not have a geologically-based conceptual model of the structure of these high-permeability zones.

7.1.1.3 Small-scale permeability variations

Hydraulic test data from wells screened over relatively short intervals (e.g. R-wells) demonstrates variability over 4 orders of magnitude exists within the Puye Formation and the basalt flows. Although no such data exist for the Santa Fe group, it is reasonable to assume that similar variability exists within these rocks.

7.1.1.4 Definition of hydrostratigraphic zones

The grouping of data presented in Figure 2-5 by rock type and the model estimates presented in Table 4-1 are based on a conceptual model that different rock types (stratigraphic unit) will have different hydrologic properties. Given the similarity of the mean permeabilities (both as evidenced by field-based testing and by inverse modeling) between rock units, it is reasonable to question this conceptual model, at least for the sedimentary rock units (Puye (fanglomerate and Totavi Lentil) and Santa Fe Group ("Los Alamos aquifer" and older rocks). Inverse models demonstrate an unbiased set of model errors for simulated heads, yet errors for any given well on the Plateau can be quite large (greater than 50m, for example). The unbiased head errors and the similarity of the permeability estimates for the major hydrostratigraphic units suggests 1) substantial heterogeneity exists within the aquifer that is not captured by the 3-D geologic model, and 2) the zones defined by the 3-D geologic model do not necessarily have hydrologic significance. This is a very different result than those reported for the vadose zone (Rogers and Gallaher 1995; Birdsell, Wolfsberg et al. 2000)

7.1.1.5 Data/analysis needs

At large-scales, our estimates of the permeability of sedimentary units are very well constrained. There are two important unresolved issues regarding sedimentary rocks: one, the large-scale permeability of Santa Fe group rocks is lower than single-hole pump tests , and two, there are small and medium-scale variations within these units that we do not understand. There are two important aspects to addressing this problem. First, we need larger-scale hydraulic tests (multi-hole tests) that can help us understand the discrepancy between permeability estimates derived from water level data and those derived from single hole tests. Second, we need to continue our efforts to develop a conceptual model and eventually a numerical model of permeability variation within sedimentary rocks. This model will be critical to our ability to accurately simulate water level gradients in the aquifer and to our ability to accurately determine flow directions at medium and local scales. Although more medium and small-scale permeability data may be helpful in this regard, we recommend emphasizing more detailed analysis of *existing* data (water level, geophysical and geologic logs, mineralogy data, hydraulic testing data) to develop a conceptual model relating our geologic understanding to permeability

variation at small and medium scales. This analysis is critical to ensure that we are collecting the appropriate types of data in the remaining R-wells.

Permeability data for the basalt units clearly shows a very large variability, presumably due to various lithologies lumped into the "basalt" category such as fractured and unfractured lava, inter-flow breccia, and inter-flow paleosols. It is unclear how important it will be to gather more detailed knowledge of the spatial distribution of these various lithologies.

7.1.2 Hydraulic gradients

7.1.2.1 Horizontal gradients

As evident in Figure 2-1, in plan view the spatial distribution of wells on the plateau is sufficient to determine that flow is generally east (although a slight southerly component is present in some areas) in the uppermost portion of the aquifer. Although deeper head data is more sparse and (in some wells) ambiguous (e.g. some heads are composite measurements over long screened-intervals and some heads are heavily influenced by nearby pumping), deeper head data also suggests easterly flow. This result is consistent with regional hydraulic gradient data, which suggests that flow is generally east-west, towards the Rio Grande, despite the well-documented fact that considerable geologic complexity exists within aquifer rocks. The radiocarbon ages of water from deep wells beneath the Pajarito Plateau increase from west to east, supporting this conceptual model of easterly flow indicated by water level data.

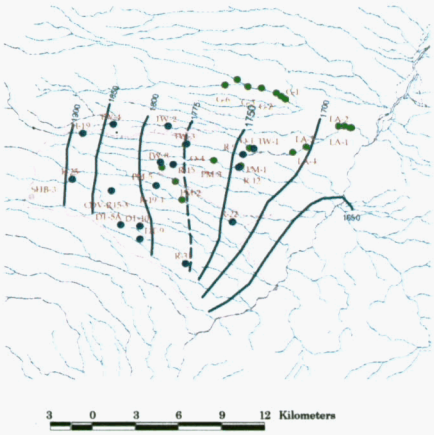

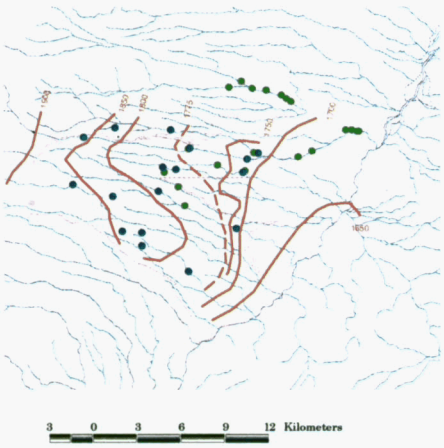

Figure 7-1. Two alternative water table contour maps, drawn using the same data

Although all the available data suggests easterly flow, departures from this trend may occur at scales smaller than typical well spacing. Figure 7-1 shows two alternative water table maps, both matching all the head data. At present, our data (hydrologic and geologic) and modeling results suggest that the map on the left, exhibiting a relatively smooth gradient, is much more plausible than that on the left. If, during drilling of the remaining R-wells, either 1) new water level data are collected that demonstrate departures from smooth regional gradients, or 2) geologic features are identified *with measured influence on permeability* that would cause either local perturbations in hydraulic gradients and/or cause bending in head contours, maps such as the one on the right side of Figure 7-1 may become more credible.

7.1.2.2 Vertical gradients

Figure 2-2 shows head contours along a cross-sectional slice through the plateau. Figure 7-2 shows the location of LANL wells (or well pairs) that indicate vertical gradients (size of circle is proportional to magnitude of gradient). This figure shows that the largest gradients are all downward. Upward gradients are evident in Los Alamos water supply wells (LA1-6) and wells in the Buckman wellfield (not shown). It is evident from this figure that we have no information about vertical gradients in the northwestern portion of the laboratory. This is an important area, since it is upgradient from potential contaminant sources such as Los Alamos and Pueblo Canyons.

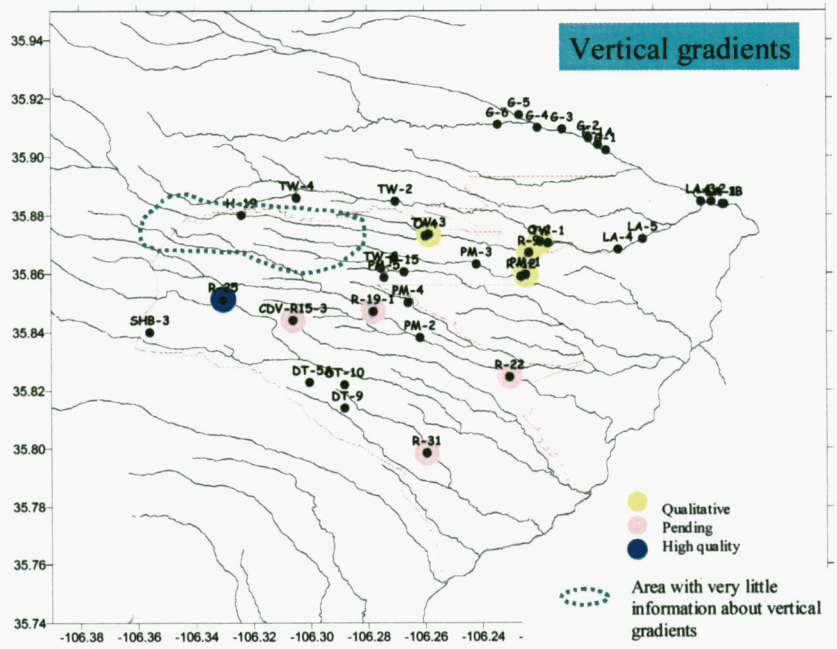

Figure 7-2. Locations with vertical gradient information

From the vertical cross-section Figure 2-2 it is evident that the R-wells are considerably more shallow that our water supply wells. This may preclude the use of an R-well as a sentry well, since in the vicinity of vertical gradients, contaminants may dive well below the water table and escape detection by shallow wells. This would be a problem in wells that draw a substantial portion of their water from deep zones; spinner logs could be used to identify wells with this type of vulnerability.

Data needs

In summary, spatial coverage is reasonable for estimating lateral plateau-scale flow directions. Vertical gradient information is also adequate, except for the northwestern portion of LANL where no such data exist. The relatively shallow depth of R-wells, compared to the depths of water supply wells, may limit their ability to detect contamination downstream of source areas with strong downward gradients.

7.2 Groundwater velocity

Estimation of groundwater velocity requires the same data as for flow directions (described above); current estimates are summarized in Chapter 3. The estimates described in this chapter are very sensitive to assumptions about effective porosity, for which we only have very small-scale data (derived from geophysical logs). The types of data that would be most helpful to

reducing the uncertainty in our estimates are 1) larger-scale estimates of effective porosity, and 2) conservative geochemical tracers. Unfortuantely, contaminants that have been detected in the regional aquifer, such as ^3H, Sr90, HE, cannot be used to calculate velocities because we do not know whether they have been transported from the source primarily in alluvial, vadose zone (including perched aquifers) or primarily in the regional aquifer. Either cross-hole tracer tests or single-hole "huff-puff" tests could provide valuable information about groundwater velocity.

7.3 Recharge/discharge

The Rio Grande is the main discharge area for the regional aquifer. Estimates of discharge are based on springflow data (although it is unclear whether springs in White Rock Canyon discharge perched aquifer(s) or the regional system) and streamflow gain along the Rio Grande. These data suggest that the regional system discharges approximately 15 cfs between Otowi Bridge and Cochiti Reservoir. Statistical analysis of streamflow data suggest that this estimate is associated with a standard error of 4.3 cfs.

The largest component of recharge occurs as underflow of groundwater from the Sierra de los Valles, to the west of the Pajarito Plateau. Recharge also occurs by leakage from mesas and from alluvial groundwater in canyon bottoms on the Pajarito Plateau. While it may be insignificant volumetrically, local recharge on the Pajarito Plateau is important because it provides pathways for contaminants that originate from effluent discharges. The exact volume of recharge occurring on the plateau is *impossible* to measure; however, using the regional aquifer discharge estimate (described above) to place bounds on the total amount of recharge that can possibly occur on the plateau we use sensitivity analyses and flow and transport modeling to evaluate the effect of various plausible recharge scenarios. For example, to predict a "worst-case" scenario, we can simulate aquifer quality assuming all recharge occurs within those canyons that are most contaminated. Water budget, chloride-mass balance estimates, and vadose-zone flow model calibration can also be used to place bounds on recharge rates. Model sensitivity analyses have shown that our uncertainty in hydrostratigraphic zonation, permeability, and porosity are much more important than the uncertainty in recharge rates, therefore we would not recommend a high priority be placed on collecting new data to better estimate these fluxes.

7.4 Montoring

Although the primary purpose of the R-wells is to provide basic characterization data, many of the wells have been located downgradient of potential contaminant sources so that they may serve as monitoring wells in the future. We used transport modeling to help site R-13 downgradient of contaminant sources in Mortendad Canyon. The particle tracking results, shown in Figure 8-12, suggest that the ideal location of a monitoring well would be slightly southeast of the source area.

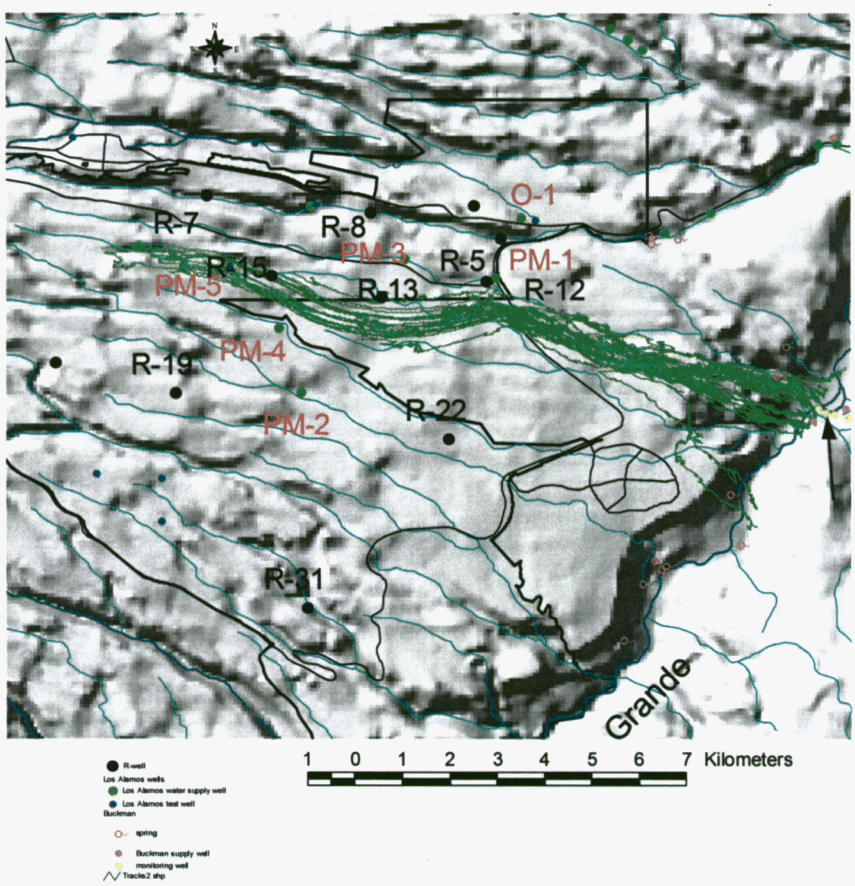

Figure 7-3. Particle tracking results, showing trajectories of particles released at the water table beneath source areas in Mortendad Canyon

8 DEVELOPMENT OF FACIES-BASED MODELS OF THE PUYE FORMATION

The Puye Formation is perhaps the most important hydrostratigraphc unit in the regional aquifer, because of its relatively large volume and the indication that there are very permeable zones within the Puye that may provide fast pathways. At present, our 3-D flow and transport models have relied primarily on assumptions of uniformity within the Puye. This assumption is the most likely cause for the mismatches between measured and simulated heads in wells completed within the Puye (see Chapter 4). The assumption of a uniform Puye Formation not only compromises our ability to correctly reproduce hydraulic gradients (and thus induces errors in our groundwater flowpath predictions) but also compromises our ability to predict fast pathways which might exist.

Keating et al (2000) presented a compilation of data regarding the depositional facies of the Puye (as observed in outcrop). These data were used to create gaussian-based heterogeneous models of the Puye, which in turn formed the basis for Monte Carlo simulations of HE transport downgradient of R25. Gaussian models, while relatively easy to construct, have been widely criticized because they fail to reproduce depositional structures within sedimentary rocks. Our more recent work has focused on building more realistic models of the Puye Formation, using a facies-based method (Markov chain). Our approach has been three-fold:

- To integrate geophysical, hydrologic, and geologic data from the R-wells into facies-based models of heterogeneity
- To test these models against recently collected water level data in the R-wells
- To develop and test methods of upscaling, since the important scales of heterogeneity within the Puye may be much smaller than can be accommodating in site-scale flow and transport models
-

It is widely recognized that sedimentary rocks can be very heterogeneous and that even detailed hydrologic investigations using very closely-spaced wells cannot produce a unique "map" of the subsurface. Therefore, it is more realistic to think of images of the subsurface in a probabilistic framework, where many possible "realizations" of the subsurface are equally likely. A large body of literature exists to generate stochastic realizations of sedimentary rocks; we

review this literature in the first section of this chapter. Relatively little research, however, has been devoted to the issues of 1) calibrating stochastic models to water level data and 2) upscaling fine-scale models of heterogeneity to coarser-scale models of flow and transport. We have made quite a bit of progress on the upscaling issue. The calibration issue has not been solved; however, we feel that the most likely reason for this is the descrepencies that exist in the hydrologic and geologic data from the R-wells regarding the Puye, and a lack of a clear conceptual model for which facies within the Puye are most important hydrologically. Until these issues are resolved, little more progress can be expected in flow model calibration.

8.1 Overview Of Stochastic Approaches To Modeling Heterogeneity

Spatial statistical methods using random field generators attempt to represent the range of possible spatial patterns in the subsurface by generating multiple, equally likely images of facies or hydraulic properties, where facies refers to an assemblage of like characteristics that severs to differentiate the unit from neighboring units. These multiple images are then used as input to flow and transport models to assess the effect of uncertainty in hydraulic properties fields on predictions of mean head and mean concentration, among other variables.

The traditional geostatistical approach to generating maps of hydraulic properties treats the true aquifer or any statistically homogeneous part as a single realization of a stochastic process. The lack of knowledge of the one true hydraulic property field requires using an assumed model of spatial structure, such as a covariance model or variogram, inferred from measurements [Journel and Huijbregts, 1978; Dettinger and Wilson, 1981; Gelhar, 1986]. In applying the stochastic theory to the real world, two concepts have been introduced: statistical homogeneity (stationarity) and ergodicity. Because complete characterization of a medium property requires knowing the joint probability density function (pdf), which is impossible, it is commonly assumed that the property of interest in the medium is stationary, i.e., the joint pdf is invariant with respect to translation in space. The term "stationary" is often referred to second-order stationary, that is, the mean of the property is constant over the space and the covariance between two locations depends on the their separation distance rather than their actual locations. By assuming that a stationary property follows some kind of distribution, we mean that the property has the same distribution at any location. However, at any location, we can have only one value of the property, thus we have to assume that the field is "ergodic", i.e., the distribution of the

property at any point can be obtained from observing the distribution of this property at different points. This is the reason why we derive distribution of the property by taking measurements at different locations and calculating statistics of the property. When measurements at some locations are available, a simulation may be performed such that the simulated values should be exactly the same with measurements at these locations. This is called "conditional" simulations.

In the case that the mean is not constant, the trending should be removed such that the mean-removed residuals (the difference between value of the hydraulic property and its mean at a given location) may be treated as a stationary process. The removed mean is then added later to the generated fields. The trending may be recognized by performing hand contouring or using some geostatistic methods, such as kriging or cokriging.

The simulation methods can be divided into Gaussian and non-Gaussian methods. *Gaussian approaches* produce the continuous log hydraulic conductivity field directly, without first creating a geologic image. Geologic information is considered in developing a trend map. Many types of soft information are difficult or impossible to consider with Gaussian methods. Gaussian approaches have been used extensively in hydrologic community, not only because this distribution is simple and convenient, but also because it has been recognized that the saturated hydraulic conductivity follows log normal distribution [for example, *Freeze*, 1975; *Hoeksema and Kitanidis*, 1984; *Gelhar*, 1993]. Many algorithms have been developed for generating Gaussian random fields, including nearest neighbors [Journel, 1974; Smith and Freeze, 1979]; turning bands [Matheron, 1970; Mantoglou and Wilson, 1981; Tompson et al., 1989]; lower-upper (LU) decomposition [Davis, 1987, Neuman, 198X]; fast Fourier transformation methods [Gutjar, 1989]; sequential Gaussian simulation [Gomez-Hernandez and Journel, 1993; Deutsch and Journel, 1998]. Sequential Gaussian simulation is the most powerful of the Gaussian random field generator algorithms. In addition to conditioning during the map generation process, it can generate very large random fields, requires only that the covariance is positive definite, can treat irregular as well as regular grids, and does not require the covariance or the mean to be stationary.

These Gaussian random generators have some limitations. LU decomposition method, for example, is usually restricted to relatively small domain. Turning bands methods itself is not suitable to generate random fields with conditioning points. Of course, through postprocessing the generated fields, one may obtains conditional fields. The fast Fourier transformation method

is also restricted to a relative small domain (512 x 512), and the field generated has to be at the size of 2^Nx 2^N, where $N \leq 9$ (a domain with a size other than 2^Nx 2^N can be cut from a larger field). In addition, conditioning fields have to be obtained through postprocessing.

To represent geological facies using Gaussian approaches, the generated fields are truncated using a set of cutoff values (thresholds). For a stationary random field, the proportions of facies are controlled by the choice of the thresholds. One of the problems is that the facies generated from truncation will have a fixed order in both the upper and lower threshold boundaries, i.e., the facies with a higher (or lower) value of the property is always adjacent to the facies with a next higher (or lower) value. However, in reality, the highly permeable gravel, for example, may be just above the lowly permeable clay.

There are many other cases for which Gaussian methods are not the best choice. First, since fields generated using Gaussian methods are usually continuous in space, abrupt transitions in hydraulic properties or discontinuities such as faults that juxtapose different rock types are often best handled using a non-Gaussian approach or a deterministic trend or zonation. Variations within each rock type or around the trend can then be generated using Gaussian approaches and added to the field generated by non-Gaussian approaches. Second, Gaussian spatial statistical models do not necessarily reproduce patterns of connected extreme values, considered one of the most important factors affecting subsurface fluid flow and transport [*Journel and Alabert*, 1987]. In addition, the assumption of multivariate Gaussianity allows for only one spatial covariance relation within an aquifer. Some complex patterns of spatial variability, such as buried channels formed by meandering streams, cannot be adequately represented solely with a variogram function and a constant mean (Fogg 1989). If the geologic pattern can be treated as deterministic through detrending, then Gaussian methods can be used for the residuals. However, if the locations of geologic features such as channels are unknown, then a non-Gaussian algorithm that considers geologic features as stochastic is preferable. Third, non-Gaussian algorithms can handle complex geologic shapes through consideration of higher-order statistics and geometric relations, provided these can be inferred. Finally, non-Gaussian methods have many more options for inclusion of soft geologic and geophysical information.

Non-Gaussian methods include indicator-based methods, Boolean methods, simulated annealing, and Markovian chains. *Indicator-based methods* rely on indicator variograms that are computed on a transformation of the original data given threshold values or categories (Journel

1983) and produce maps that are quite different from those produced using Gaussian methods. One of the advantages of indicator-based methods is that there are no limitations on distribution. In addition, indicator algorithms allow including hard and soft data. Here the term "hard data" is what can be described with some specificity, which usually means that it is quantified, such as a measured porosity value at a location, or observed hydrostratigraphic unit (e.g., sandstone) at a location. While the term "soft data" means at a location the property takes a certain value at some probability. For example, in some old wells that penetrating the Puye Formation, the formation is classified as fanglomerate. Though we are not sure what the particular unit is, this classification does give us some prior information about the unit: it is not Totavi Lentil, and it is one of units in the Puye Formation (except for Totavi Lentil) with probabilities equal to their volumetric proportions. Any soft information that can be quantified and turned into a prior local probability value in terms of a threshold or category type can be used [*Journel*, 1986a, b; *Zhu and Journel*, 1993]. The ability of indicator-based methods to consider soft data has important implications for successful simulation of groundwater flow and transport. One of the limitations is that cross covariances between different classes of indicators are generally ignored. In addition, the maps produced by indicator-based methods are sensitive to the form and parameters of the indicator variograms. For example, given the same conditioning data, anisotropic and isotropic indicator variograms produce very different maps. Indicator-based algorithms include indicator kriging, sequential indicator simulation, and indicator principal components.

Simulated annealing is an optimization problem in which an objective (or energy) function minimizes the difference between features desired in maps of the subsurface and the statistics calculated from the current image. Any geologic feature that can be specified quantitatively in the objective function can be included. In simulated annealing, either an initial map of node values is generated by another spatial statistical method, or an initial map is generated by assigning hard data to their nearest nodes in a grid and drawing from a data histogram to assign all remaining node values. An iterative procedure ensues in which pairs of nodes not associated with hard data are swapped to reduce an objective function that minimizes the difference between the desired spatial structure and the structure currently exhibited by the map. The iteration procedure stops when further swaps would not lower the value of the objective function, or when a target objective function is achieved. The final map maintains the data histogram and the conditioning data, but has rearranged the values assigned to the initial image.

Boolean algorithms have been used in generating sand/shale fields [*Haldorsen and Chang*, 1986]. Simple shapes (ellipsoids, parallelepipeds, semicircles or half moons) are generated and placed randomly onto a background. Geologic information is used to establish probabilistic rules and geometric constraints that govern the distribution, geometry, direction of elongation, and connectedness of objects in space. Smaller-scale variability within each rock type can be superimposed using Gaussian methods. For each rock type, however, probabilistic and geometric rules must be defined. Although Boolean images can be conditioned by specifying, in a nonrandom manner, the locations of rock types in well logs at the start of the generating procedure and then randomly selecting the object geometries in the other dimensions [*Haldorsen et al.*, 1988], conditioning is particularly difficult with closely spaced well data. *Deutsch and Journel* [1992] list additional problems with Boolean methods: (1) lithofacies do not conform to the simple geometric shapes commonly used; (2) lithofacies are not randomly distributed in nature; and (3) these algorithms are difficult to generalize and must be custom-designed for each depositional pattern.

Markov chains have been used to predict preferential facies successions and deduce repetitive patterns of sedimentation. This approach generates a synthetic stratigraphy by ordering discrete facies types and bed thicknesses in a sequence. Doveton [1994] notes that vertical transition frequencies can be used for prediction in the horizontal dimension by invoking Walther's law, which states that facies that succeed each other in a conformable vertical sequence were deposited in adjacent depositional environments. In this study, we will employ Markovian chain model, partially because the code is available, partially because it can be easily incorporated with Gaussian methods to generate combined realizations, in which the distribution of different materials are generated using Markovian model while the variation within each material is produced using Gaussian methods.

8.2 Markov Chain Theory

Markov chains offer an interpretable and mathematically simple yet powerful stochastic model for categorical variables. In time-series applications, the Markov chain model assumes that *the future depends on the present and not the past.* Analogously for one-dimensional spatial applications, the Markov theory assumes that spatial occurrences depend entirely on the nearest data. The Markov chain method has been applied to geological formations with different materials [*Harbaugh and Bonham-Carter*, 1970; *Agterberg*, 1974; *Lin and Harbaugh*, 1984; *Polltis*, 1994; *Carle*, 1996; *Carle and Fogg*, 1997; *Carle et al.*, 1998]. The distribution of materials is characterized by the transition probability between different materials. It has been shown [*Carle*, 1996; *Carle* and *Fogg*, 1997] that, in characterizing the structure of the indicator random functions, the transition probability between different classes is equivalent to covariance of the indicator random functions and the former can be easily derived from field measurements.

It is assumed in a three-dimensional Markovian chain model that spatial variability in any direction can be characterized by a one-dimensional Markovian chain model [*Lin and Harbaugh*, 1984; *Politis*, 1994]. For a one-dimensional Markovian chain model, the continuous-lag transition probability matrix T for any lag can be written as [*Carle*, 1996; *Carle and Fogg*, 1997]:

$$T(h) = e^{Rh} \text{)Equation 8-1}$$

where R is an $M \times M$ (for more general cases, M being the number of materials) transition rate matrix whose entry r_{ij} represents the rate of change from category i to category j per unit length of category i in the given direction. If the transition rate matrix R is known, the transition probability matrix T can be evaluated by the eigenvalue analysis. Let η_i, $i = 1,2, \ldots, M$, be eigenvalues of the transition rate matrix R, and Z_i, $i = 1, 2, .., M$, be their corresponding spectral component matrixes that are evaluated by

$$Z_i = \prod_{m \neq i} (\eta_m E - R) \Big/ \prod_{m \neq i} (\eta_m - \eta_i) \qquad \text{(L2)}$$

where E is the identical matrix, then (L1) becomes

$$T(h) = \sum_{i=1}^{M} e^{\eta_i h} Z_i \qquad \text{(L3)}$$

which means that the transition probability is summation of a series of exponential terms.

Now we focus on how to evaluate R and relate the covariance of the indicator random variables to the statistics of different materials in a porous medium. Suppose we have a transition probability matrix T measured at a discrete lag Δh in a direction ϕ, the transition rate matrix R_ϕ can be computed [*Agterberg*, 1974; *Carle*, 1996; *Carle and Fogg*, 1997]

$$R_\phi = \frac{\ln[T(\Delta h_\phi)]}{\Delta h_\phi} \tag{L4}$$

which again involves an eigenvalue analysis. In this case, the transition probability matrix for the direction ϕ at any lag can be calculated using (L1) to (L3), and the proportions of all categories can be calculated by multiplying the transition matrix to itself a number of times until the product is stablized.

In reality, the discretized-lag transition probability matrix in the vertical direction may be obtained, for example, from borehole data. Thus transition rate matrix R can be computed using (L4). However, in the lateral directions, sparse data may prevent directly measuring discretized-lag transition probability matrix. In this case, one is unable to calculate R using (L4), thus, some alternative ways for deriving R are needed. Taking derivative of (L1) with respect to h and let $h = 0$, we have

$$R = \left.\frac{dT(h)}{dh}\right|_{h=0} \tag{L5}$$

Since the transition probability t_{ij} has to satisfy $\sum_{j=1}^{M} t_{ij} = 1$ and $\sum_{i=1}^{M} p_i t_{ij} = p_j$, $j = 1,2,\ldots M$, it follows immediately that transition rate r_{ij} satisfies

$$\sum_{j=1}^{M} r_{ij} = 0 \qquad i = 1,2,\ldots M \tag{L6}$$

$$\sum_{i=1}^{M} p_i r_{ij} = 0 \qquad i = 1,2,\ldots M \tag{L7}$$

Equations (L6) and (L7) imply that $det(R)=0$, therefore, one of the eigenvalues of R, say η_1, must be zero. The spectral component matrix Z_1 corresponding to this zero eigenvalue has special meaning, i.e., any row of Z_1 represents the proportions of all categories.

For a given porous medium, proportions of categories are the same in any direction. Therefore, once the transition matrix T (and so R) in one direction $\phi 0$ is known, R in any other direction ϕ may be estimated with some additional information. Carle [1996] shows that the diagonal terms of the transition rate matrix $R\phi$ is related to mean lengths:

$$r_{ii,\phi} = -\frac{1}{L_{i,\phi}} \tag{L8}$$

In practice, if the mean length of one category, say $L_{1,\phi}$, in direction ϕ is known, the mean lengths for all other categories in this direction can be calculated from $L_{i,\phi}, = p_i L_{1,\phi}/p_1, i = 1,2,\ldots,M$.

For a bimodal porous medium, either knowing proportions (maybe from other directions) and one mean length or knowing two mean lengths in the direction ϕ is enough for solving R in this direction. It is seen that, if the mean lengths in a given direction are L_1 and L_2, respectively, the transition rate matrix is in the following form

$$R = \begin{bmatrix} -1/L_1 & 1/L_1 \\ 1/L_2 & -1/L_2 \end{bmatrix} \tag{L9}$$

Two eigenvalues are $\eta_1 = 0$ and $\eta_2 = -1/p_2L_1 = -1/p_1L_2$, and their corresponding spectral matrixes are

$$Z_1 = \begin{bmatrix} p_1 & p_2 \\ p_1 & p_2 \end{bmatrix} \qquad Z_2 = \begin{bmatrix} p_2 & -p_2 \\ -p_1 & p_1 \end{bmatrix} \tag{L10}$$

From (L3), the transition probability t_{ij} can be written as

$$t_{ij}(h) = p_j + (\delta_{ij} - p_i)\, e^{-h/\lambda_I} \tag{L11}$$

where the parameter λ_I is defined as

$$\lambda_I = p_1L_2 = p_2L_1 = L_1L_2/(L_1 + L_2) \tag{L12}$$

It should be emphasized that, if the mean lengths depend on directions, the correlation length λ_I is also direction-dependent, and so is the transition probability (L11).

Once the three-dimensional transition probability model has been generated, then conditional (or unconditional) simulations can be performed through a two-step procedure: (1)

generating an initial configuration using a cokriging-based version of the sequential indicator simulation algorithm (Deutsch and Journel, 1992), and (2) iteratively improving the conditional simulation in terms of simulated and modeled transition probability using simulated annealing. The initial configuration use a transition probability-based indicator cokriging estimate to approximate the local conditional probability:

$$\Pr\{k \text{ occurs at } x_0 \mid i_j(x_\alpha); \alpha = 1,2,...N; j = 1,2,...K\} \approx \sum_{\alpha=1}^{N}\sum_{j=1}^{K} i_j(x_\alpha) w_{jk,\alpha} \qquad (**)$$

where N is the number of data, K is the number of categories, $i_j(x_\alpha)$ is the value of the indicator variable, and $w_{jk,\alpha}$ represents a weighting coefficient which is obtained by solving the following equation:

$$\begin{bmatrix} T(x_1 - x_1) & \cdots & T(x_N - x_1) \\ \vdots & \ddots & \vdots \\ T(x_1 - x_N) & \cdots & T(x_N - x_N) \end{bmatrix} \begin{bmatrix} W_1 \\ \vdots \\ W_N \end{bmatrix} = \begin{bmatrix} T(x_0 - x_1) \\ \vdots \\ T(x_0 - x_N) \end{bmatrix} \qquad (**)$$

where $W_k = (w_{ij,k})$. The obtained field is iteratively adjusted by minimizing the object function:

$$O = \sum_{l=1}^{M}\sum_{j=1}^{K}\sum_{k=1}^{K}\left[t_{jk,MEAS}(h_l) - t_{jk,MOD}(h_l)\right]^2 \qquad (**)$$

The iterative improvement procedure continues until the object function O is minimized, or a limit on the number of iterations is reached. Conditioning is maintained by not allowing change of categories at conditioning locations.

8.3 Derivation Of Statistical Properties For Puye Formation

We have been compiling and interpreting geologic and geophysical data from boreholes, outcrops, and geologic maps. Much of the preliminary work is described in Keating et al. (2000

8.3.1.1 Spatial analysis of geophysical data

The geophysical data were collected by Schlumberger for R-7, R-19, and CDV-R-15, and have been summarized in Chapter 2. We have analyzed parameters derived from geophysical logs (permeability, water content, and porosity) to determine if distinctive spatial structures exist. The basic analytical tool for this analysis was generation and interpretation of variograms and semivariograms.

8.3.1.2 Variogram overview

The variogram is an alternative way to measure the spatial variability of a regional variable Z and is defined as

$$2\gamma(\mathbf{h}) = \mathrm{var}\{Z(\mathbf{u}+\mathbf{h}) - Z(\mathbf{u})\}^2 \qquad \text{(S2)}$$

where u is a location and h is the separation vector. In general, the separation vector h is specified with some direction and distance (lag) tolerance. For a variable sampled at regularly spaced locations in a direction, the semivariogram may be calculated using the following formula

$$\gamma(h) = \frac{1}{2N(h)} \sum_{i=1}^{N(h)} \{Z_i - Z_{i+h}\}^2 \qquad \text{(S3)}$$

where N(h) is the number of possible data pairs that are separated at distance h. For instance, if $h = 10$, then all pairs of points in this direction with distance 10 units are used in calculating $\gamma(10)$. The expected form of the semivariogram is that γ should increase as h increases. This is because points that are close together should be more similar than points that are widely separated. Eventually a lag (h) is reached, above which γ does not increase. This is called the sill. When a variogram is extrapolated back to zero distance, it may not approach zero variance. The amount by which the variance differs from zero is known as the nugget effect. In a special case that the attribute of interest is periodical in the direction, it is expected that the variogram shows a sharp decrease at the separation distance that is equal to the multiple of the length of the period. In an ideal case, if two materials repeat in a sequence, the variogram will show a quickly

increase from zero till some value at the separation distance of L1/2, and then variogram continuous to increase slowly until the separation distance at L2/2. Further increase of separation distance will cause a suddenly decrease on semivariogram until separation distance at (L1+L2)/2. Though, in realty, we will never see such an ideal case, the semivariogram does give us some indication about the mean lengths of different materials.

R-Well data

Semivariograms for permeability data from R7, R19, and CDV-R-15 are shown in Figures 8-1- 8-3. It is interesting to note that all three of these figures show evidence of a two-material system. In addition, in all three wells there is indication that the mean length of the lesser material (volumetrically) is approximately 5m. We estimate the mean length of the more prominent material to be approximately 40-60 m.

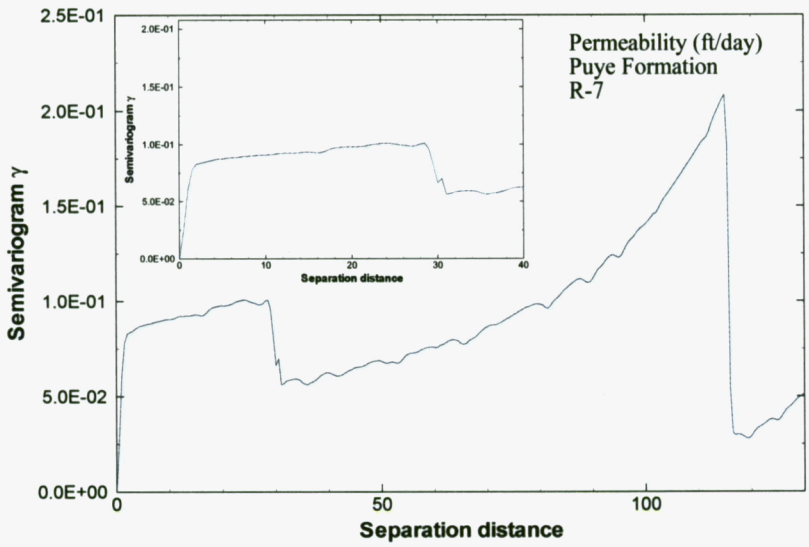

Figure 8-1. . Semivariogram calculated from permeability data in well R-7

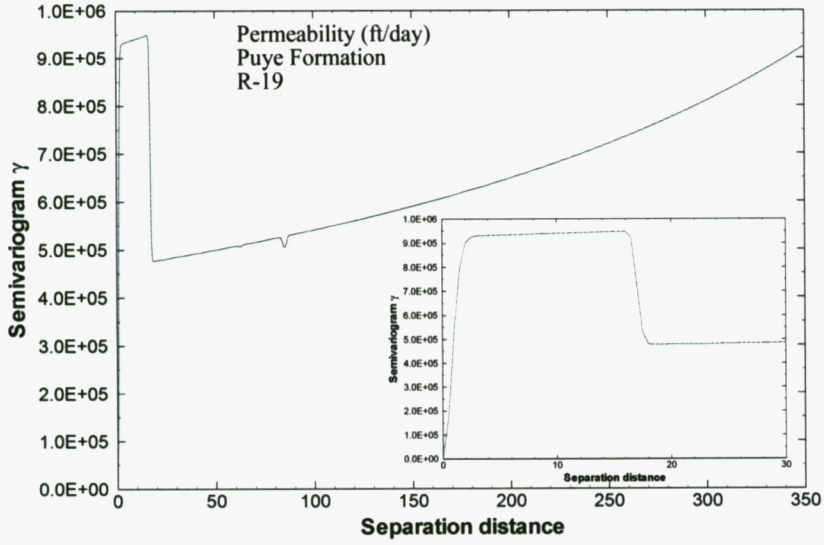

Figure 8-2. Semivariogram calculated from permeability data in well R-19

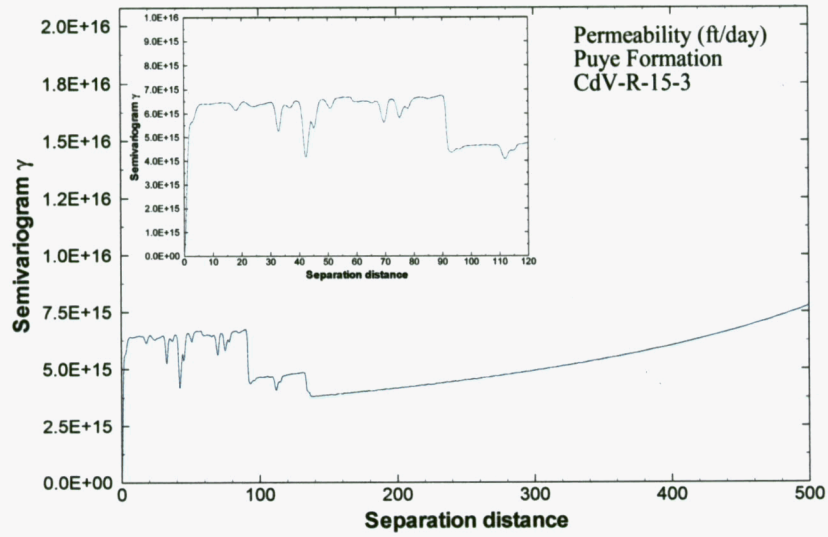

Figure 8-3. Semivariogram calculated from permeability data in well CDV-R-15

8.3.1.3 Analysis of textural classes identified in well logs and outcrops

We have compiled textural class data from well logs in well completion reports (list here), Purtymun (1995), and Waresback (1986). The locations of these wells are shown in Figure 8-4.

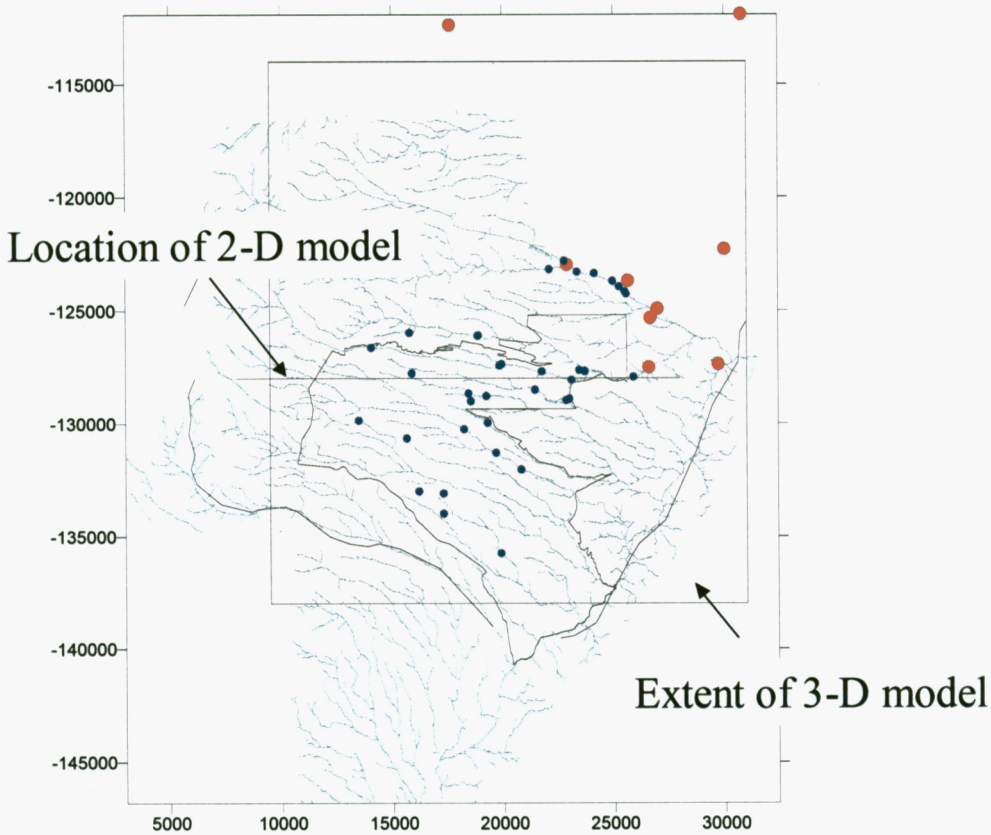

Figure 8-4. Location of wells (blue dots) and outcrop data (red dots

Based on description in well completion reports (R-9, R-12, R-15, and R-19?), we have divided the Puye formation into five categories: gravel, coarse sandstone, fine sandstone, clay, and Totavi Lentil. We used a very simple method to determine the classification. A material is classified as "gravel" if terms "gravel", "gravelly" or "conglomerate" appear in its description. The class "coarse sandstone" refers to those materials with "coarse sandstone" in their description. The class "fine sandstone" represents those core segments with terms "fine" or "fine-grained" in their description. Though the fraction of the clayey material is very small, we separate it from other classes because it may have great effect on flow and solute transport. This class also includes "mudstone" as appearing in the outcrops. Intervals with descriptions that do not fall into any of the above classes are lumped together as "unclassified"

In well logs presented in Purtymun (1995), the Puye Formation is classified into fanglomerate and Totavi Lentil. Though there is no detailed classification within fanglomerate, this kind of information can be used in the future as soft data in conditioning simulations in such a way that the probability of the fanglomerate being any one of the above four types is proportional to their volumetric proportions. In total, we analyzed data from 39 wells. Detail classification for each outcrop section and well is shown in Table C-3and Table C-4, respectively. The total thickness and percentage of each material are listed in Table C-5.

8.4 Generation Of Markov Chain Models

We have genererated both three and two-dimensional Markov chain models. The three-dimensional models are very large, encompassing the full extent of the saturated Puye Formation on the Pajarito Plateau. We generated two sets of realizations according to two different approaches to parameter estimation, both derived from site-specific geologic data for the Puye

In order to develop methodology for calibration to water level data, we also developed smaller, two-dimensional models In the two-dimensional models, we generated one set of realizations generated using site-specific data for the Puye; the other set was generated using synthetic data. Model development is described in the sections below.

8.4.1 Parameter derivation

Markov chain models require 3 (2-D models) or 4 (3-D models) parameters to be specified for each material class: the fraction of the total volume occupied by that material (f) and the mean length of that material in each axis direction (l_x, l_y, and l_z). Of these parameters, the most difficult to estimate are the mean lengths, particularly in the lateral directions (l_x and l_y). For a model with *n* material classes, parameters only need to be specified for *n-1*materials; parameters for the last material can be derived from the others.

The initial models presented in this report are based on a simple two-class approach. We divided the Puye into Totavi and non-Totavi materials, since for many of the original wells on the plateau these are the only two materials identified (Purtymun, 1995). Starting with a two-class is approach is reasonable considering the sparseness of the dataset and the difficulty of estimating l_x and l_y for any classes. Our conceptual model is that Totavi deposits, being much

coarser grained and *possibly* better sorted than other Puye (fanglomerate) deposits, may be more permeable.

The volumetric proportions of two materials are calculated from Table C-5. For the three dimension models, we used all the available well data to derive volumetric proportions and mean lengths in the vertical direction; for the 2-D models we used a subset along an E-W transect (R-25, R-19, R-15, R-12, and R-9). The resulting parameters are shown in Table 8-1and Table 8-2. Using the well data, our estimate of mean length (vertical direction) for the Totavi Lentil (18m) is in very close agreement with estimates reported in (Keating, Kwicklis et al. 2000) from outcrop data (12-24 m).

We use several different methods to estimate lateral mean lengths, which are far less certain. The first (Model 1) is to assume that data collected in outcrop are reasonable approximations; this method should underestimate true lateral mean lengths and thus serves as an end-member. The second (Models 2 and 3) are based on a conceptual model that the Totavi deposits are long, thin, fluvial deposits approximately parallel to the modern Rio Grande channel, on average approximately the same width as the modern channel (Reneau 2001). To derive l_x, we estimated the width of the channel alluvium using a geologic map (Puye Quadrangle, 7.5 minutes series). We set up 80 equally-spaced measurement points along the length of the river in the vicinity of the Puye and measured the width of the river and surrounding alluvium (average = 97.5m). This estimate is somewhat smaller than those reported for outcrops in Keating (2000) (50 – 560 m). The parameter lz_y corresponds to the length parallel to the Rio Grande. We use two estimates for this parameter, for which we have no data (2000 m (Model 2) and 500m (Model 1)

Parameters for the non-Totavi class were derived from the Totavi class, since this is a two-class model.

Table 8-1. Parameters used for Markov chain models

Parameter	Totavi	Non-Totavi
Volumetric fraction	0.13	0.87

Mean	Totavi			Non-Totavi		
Length (m)	Model 1	Model 2	Model 3	Model 1	Model 2	Model 3
l_x	345	97.5	97.5	2309	652.5	652.5
l_y	560	2000	500	3748	13385	3346
l_z	18	18	18	120.5	120.5	120.5

Table 8-2. Parameters used for 2-D Markov chain models

Parameter	Gravel	Sand
Volumetric fraction	0.552	0.448
Mean lengths (m)		
l_x	1109	900
l_z	37	30

8.4.2 Model domain and grid resolution

The extent of the domain for the 3-D models is 9500~ 31000 meters in the x direction (East-West), -13800~ -114000 meters in the y direction (North-South), and 1600~2088 meters in the z direction (vertical). This encompasses the entire saturated Puye Formation on the Pajarito Plateau. The vertical resolution of measurements at the outcrop locations is typically about a few centimeters, while the vertical resolution of the well data is about 5 ft. The vertical resolution of both these datasets is much greater than the vertical resolution of the flow and transport model (12m). Nevertheless, we chose to create Markov chain models of the aquifer at a resolution fine enough to capture the heterogeneity present in the dataset. Issues related to upscaling (mapping properties onto a coarser flow and transport grid) will be addressed separately.

Many factors have been considered in designing the Markov chain grid: the grid size used in the flow and transport model, the correlation lengths of the formation in three directions, and the balance between accuracy and computational efforts. It is commonly required that the grid size in any direction should be small enough such that each correlation length should be larger than 4 or 5 grid elements. Some researchers suggested that the grid resolution δ should satisfy the relationship: $\delta / \lambda \leq 1/(1+\sigma^2_{\ln K})$, where$\lambda$ is the correlation length in the given direction and $\sigma^2_{\ln K}$

is the variance of the log hydraulic conductivity. The relationship may be used only for generating permeability field for saturated flow simulations. For unsaturated flow simulation, it is generally required that the grid size should be less than $1/\alpha$, where α is the pore size distribution parameter. Assuming the covariance of permeability follows an exponential model, we can estimate the correlation lengths by dividing the mean lengths (Table 8-1) by a factor of three (λ_x= 32.5m, λ_y= 667m, λ_z= 18.7m).

Another consideration on the choice of the grid size is the current grid size in the basin model. To avoid unnecessary interpolation of the generated fields, the size of the finer grid should be selected such that after several steps of upscaling the grid should fit the coarser grid in the basin model. Because of the large extent of the Puye Formation, the computational effort will be very large if the spatial discretization is too fine.

Based on these arguments, we choose a grid with a resolution of 31.25 m, 250 m, and 1.5 m in the x, y and z directions. The total number of nodes in this grid is 688×96×328 (= 21,159,936 nodes).

The 2-D models are based on a grid resolution of dx = 100 m and dz =5 m. The model extends approximately from the topographic divide west of LANL to the Rio Grande (see Figure 8-4). The bottom of the model is 915m MSL.

8.4.3 Conditioning

We require each of our statistical realizations to fit the measured data exactly. This is accomplished using a process called "conditioning". Although both well and outcrop data were used to develop the statistical parameters for the simulations, our initial simulations are only conditioned to the well data; these are listed in Table C-1.

8.5 Images.

The following three images are one realization from each of the three model sets (see Table 8-1)

Model 1

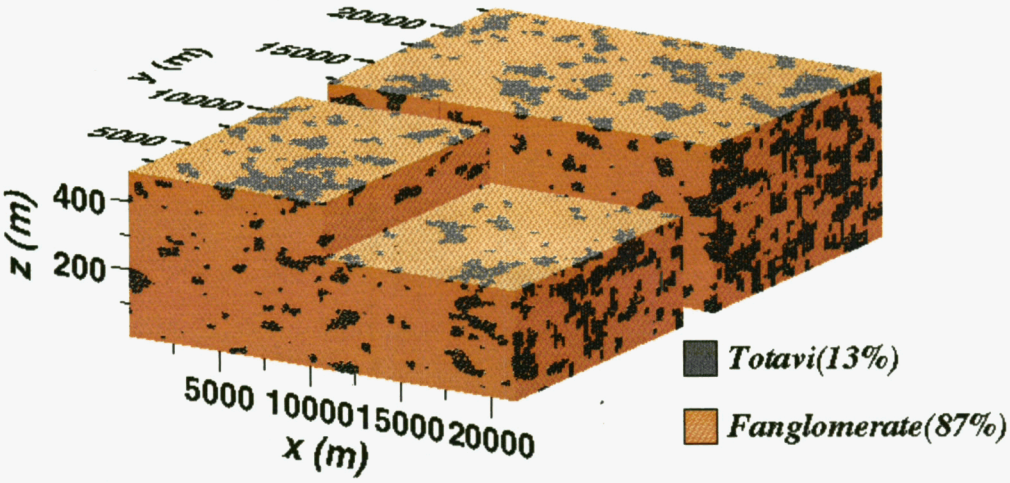

Model 2

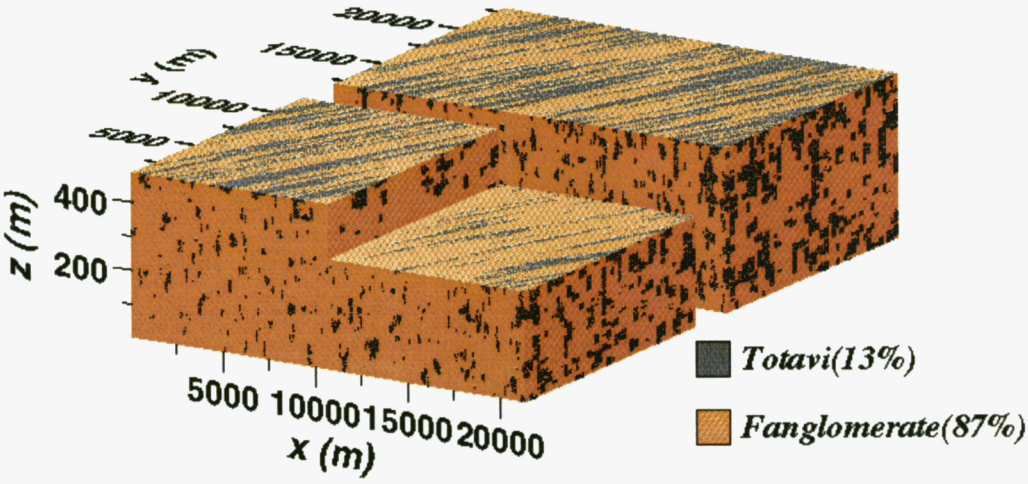

Model 3

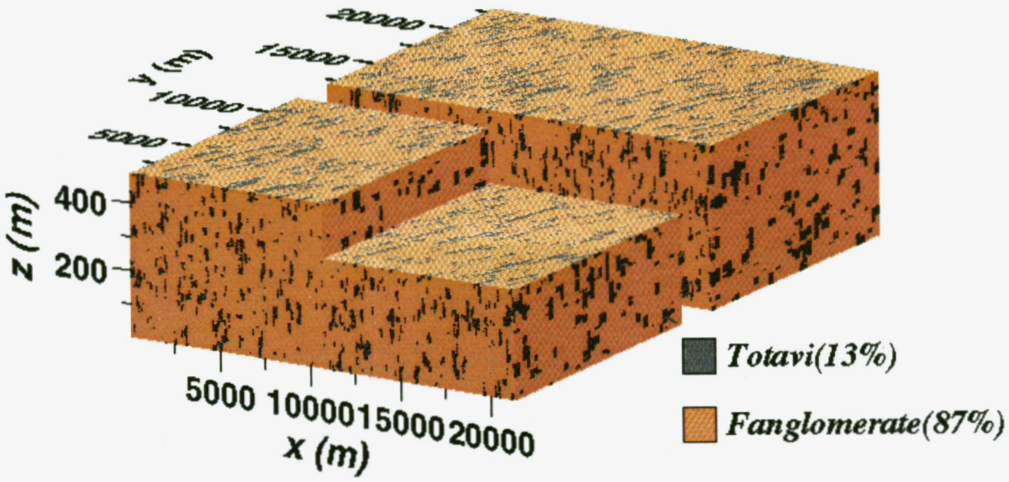
20000
15000
y (m)
10000
5000
400
z (m)
200
5000 10000 15000 20000
x (m)
Totavi(13%)
Fanglomerate(87%)

3

8.6 Calibrating 2-D Markov chain models to head data

We use a stochastic approach to modeling heterogeneity within the Puye because wells are sparsely spaced and multiple hydrostratigraphic models can be constructed, all of which honor with data collected in each well. Of these hundreds/thousands of plausible geologic models, only a subset will be compatible not only with geologic data but also with hydrologic data (water levels). If our aquifer model is correct, we should expect very small or zero differences between simulated and measured heads at each well. Since our model errors assuming uniform permeability within the Puye are substantial in certain wells, we should expect a heterogeneous model of the Puye to improve the model fit.

Since three-dimensional stochastic modeling is very computationally intensive, we developed two-dimensional models of the Puye Formation that could be used to develop and test methodology for calibration of stochastic models. For these models, we selected wells that were approximately along a two-dimensional cross-section (R25, R15, R19, R9, and R12). Using the classes derived from drillers lithologic logs (see Table C-4), 1000 Markov-chain realizations of the Puye Formation were generated, conditioned to data in these 5 wells.

For model calibration, we used water level data from selected wells on the plateau (locations are shown in Figure 8-5). In the calibration procedure, all of these data were collapsed onto an E-W cross-section. This is a reasonable assumption for the wells used for the Markov chain models (solid circles), since these are located approximately on an E-W transect. We justified collapsing the water level data onto an E-W cross-section based on the approximately E-W gradient evident in the water table map (see Figure 2-1). The validity of this assumption remains to be tested.

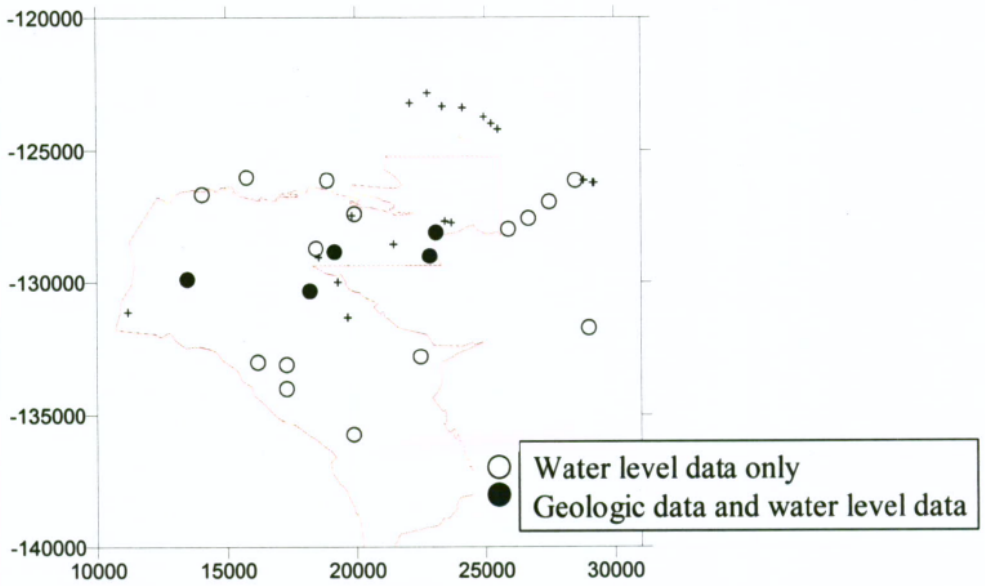

Figure 8-5. Location of wells used for Markov chain model conditioning and flow model calibration

Figure 8-6 depicts one realization of a Markov chain model, conditioned to geologic data at the five wells indicated in Figure 8-5. The model domain extends to the Rio Grande, including portions of the aquifer that are Santa Fe Group. These models, therefore, assume that the type of heterogeneity present in the Puye Formation is similar to that in the Santa Fe Group. Like many other assumptions in this analysis, this one remains to be tested.

Figure 8-6 also shows measured heads in wells along the cross-section (open circles in Figure 8-5). This figure demonstrates the clear downward gradient in the vicinity of R25 and upward gradients close to the Rio Grande. The bottom frame in the figure shows the result of a steady-state flow model for this cross-section. We used the parameter estimate code (PEST) to estimate the permeability of each of the two classes of rock to provide the best fit to measured heads. For this simulation, the upper boundary is a recharge boundary (rates are determined by an elevation-dependent model); the western and lower boundaries are no-flow. The eastern boundary is also no-flow, except a small group of nodes near the upper east-most corner of the grid which are designated specified head (elevation of the Rio Grande

Qualitatively, the measured and simulated heads are similar. However, significant disparities exist in matches to individual wells, particularly heads in R22. To improve the match, we used a number of strategies: 1) excluding data from the calibration dataset that may be influenced by pumping (there is no pumping in the model), 2) relaxing the 'no-flow' assumption

at lateral boundaries, 3) replacing the water table boundary (specified flux) with a specified head boundary. Unfortunately, none of these strategies resulted in a significantly better model.

We also performed a series of model calibrations to this 2-D dataset using a more simple model of heterogeneity: a two parameter anisotropic model (kx ≠ky). In general, these models performed as well as the Markov chain models.

Despite that lack of agreement between simulated and measured heads in some wells, all of these calibrations suggested that there is little question that the Puye Formation is strongly anisotropic. Simple models of heterogeneity (two parameter anisotropic models) suggested that k_z is approximately two orders of magnitude lower and k_x. Calibration of Markov chain models suggested that the permeability of "low k" zones is approximately 2.5X lower than "high-k" zones.

We analyzed geophysical datasets to determine if there is a relation between permeability estimates derived from geophysical logs and textural classes (according to drillers lithologic log).

Table 8-3 shows the results of this comparison for two wells. This result suggests that the textural class "fine sandstone" has clear hydrologic significance, having a much lower permeability than coarse sandstone or gravel. However, the distinction between coarse sandstone and gravel does not appear to be significant.

Table 8-3. Comparison of geophysical data and textural class in R-19 and CDV-R-15

Classes	# of data	Mean K (ft/day)	Variance of K
Gravel	345	0.453	7.10
Coarse sandstone	1323	0.579	6.16
Fine sandstone	316	0.008	0.0006

8.7 Conclusions and suggestions for future work

We consider these results to be very preliminary. However, these models do suggest that there is little doubt that the Puye Formation is strongly anisotropic. At present, however, Markov chain models do not produce a significantly better agreement between simulated and measured heads, compared to uniform models (2-D or 3-D). There are many possible reasons for the lack of agreement between measured and simulated heads in these 2-D flow fields, such as three-dimensional effects (both in water levels and in the heterogeneity of the Puye) that

cannot be approximately with a 2-D model, the effects of pumping (not considered in these models), the number of classes in the Markov chain models (perhaps more than 2 are necessary), the parameters used for the Markov chain models (recall that lateral mean lengths are quite uncertain). It is also possible that the Markov chain approach is inappropriate for the Puye. Until these various possibilities are tested, it is difficult to draw firm conclusions about the nature of heterogeneity within the Puye.

The conceptual basis for the Markov chain model is that the most important high permeability facies within the Puye is the Totavi Lentil. At present, hydraulic testing results suggest that the Totavi Lentil contains both high and low permeability zones (see Figure 2-5); thus, our conceptual model may be flawed. We recommend that further analysis of geologic, hydrologic, and geophysical data be conducted so that our Markov chain models are based on a defensible conceptual model. At that point, these model calibrations can be continued and improved.

Because the mean length of Totavi Lentil in the x direction is about 100 meters, the grid size of 250 meters in this direction in the current model is too large and should be reduced.

Large variation of the hydraulic conductivity has been observed within each facies, it is therefore recommended that the variation within the facies be considered in the future work. This can be done by the following way. For each realization of Markovian chain model with *ncat* categories, instead of assigning a constant hydraulic conductivity value to each category, we can generate *ncat* continuous realizations with specified means, variances, and correlation scales corresponding to these categories. Each realization used in the flow simulation is obtained by combining *ncat* continuous realizations, based on the Markovian chain realization. More detail description on this method can be found in *Lu et al.* [2001].

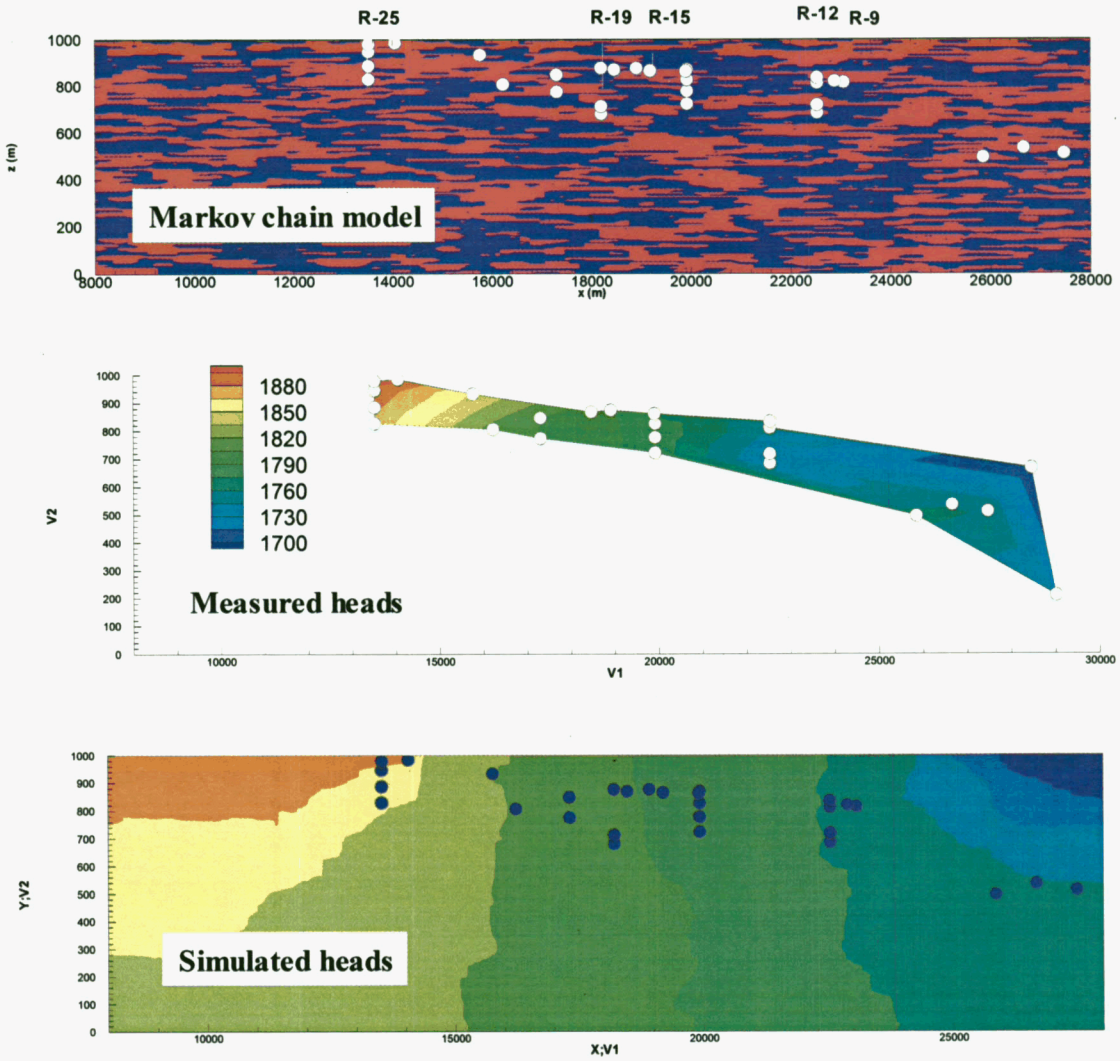

Figure 8-6. Markov chain model, measured and simulated heads

8.8 Equivalent/Effective Permeability

One important challenge inherent in imbedding a geostatistically-based model of heterogeneity within a flow and transport model is calculating the effective permeability of a geostatistical representation. The permeabilities of materials within the geostatistical domain should be adjusted so that the overall equivalent permeability of the domain is equal to that which is obtained through analysis (e.g. pump test interpretation, inverse modeling) of the same rock unit assuming homogeneous properties.

By equivalent permeability we mean a constant permeability tensor taken to represent a heterogeneous medium. Because a complete equivalent between the real heterogeneous medium and the fictitious homogeneous one is impossible, it is therefore required to defined some criteria that must be the same for both media. The most commonly used criterion is the equality of flow. Under the same head gradient, the flow at the boundaries of the domain should be identical for the real heterogeneous medium and the equivalent homogeneous medium. The term "effective permeability" is used for a medium that is statistically homogeneous on the large scale and is defined as

$$\langle u \rangle = -\mathbf{K}_{ef} \langle \nabla h \rangle \qquad \text{(E1)}$$

where $\langle\ \rangle$ represents expectation. The effective permeability is an intrinsic property, independent of the macroscopic boundary conditions. Many models have been developed to estimate the equivalent/effective permeability of the binary medium. *Hashin and Shtrikman* [1963] gave bounds for the isotropic binary medium as

$$\mu_a - \frac{f_1 f_2 (k_2 - k_1)^2}{(D - f_1)k_1 + f_1 k_2} \le K_{ef} \le \mu_a - \frac{f_1 f_2 (k_2 - k_1)^2}{(D - f_1)k_2 + f_1 k_1} \qquad \text{(E2)}$$

where f_1 and f_2 are the fractions of material 1 and material 2 in the medium; k_1 and k_2 ($k_1 < k_2$) are the permeability of two materials, and $\mu_a = f_1 k_1 + f_2 k_2$ is the arithmetic mean of the permeability of two materials. Using the self-consistent approach (or embedded matrix method), in which the heterogeneous medium consisting of homogeneous blocks placed side by side is replaced by a single inclusion of K permeability embedded in a homogeneous matrix with an unknown permeability, *Dagan* [1979] derived the formula for the effective permeability as

$$\mathbf{K}_{ef} = \frac{1}{D}\left[\int_0^{\infty} \frac{f(\mathbf{K})d\mathbf{K}}{\mathbf{K} + (D-1)\mathbf{K}_{ef}}\right]^{-1} \tag{E3}$$

where f(K) is the probability density function of the permeability, D is the space dimension. For a binary medium, (E3) simplifies to

$$K_{ef} = \frac{1}{D}\left[\frac{f_1}{K_1 + (D-1)K_{ef}} + \frac{f_2}{K_2 + (D-1)K_{ef}}\right]^{-1} \tag{E4}$$

To take into account of anisotropy of permeability field, *Neuman* [1994] derived the formula:

$$\mathbf{K}_{ef} = K_g \exp\left[\sigma_Y^2\left(\frac{1}{2} - \frac{\beta}{D}\right)\right] \tag{E5}$$

where $0 \le \beta \le D$, and $Kg = \exp(\langle Y \rangle)$. Ababou [1995] gave $\beta = l_h / l_i$, where l_h is the harmonic mean of the correlation lengths in the principal directions of anisotropy, l_i is the correlation length in the considered direction.

Now we consider horizontal flow in a two-dimensional vertical cross-section with a size of 200 m in the horizontal direction and 100 m in the vertical direction. The element size is 1.0 m by 1.0 m. Two vertical wells are located at x = 65 m and 135 m, with a depth of 70 m. The porous medium consists of two materials, with volumetric fractions of 0.85 and 0.15, respectively. The mean lengths of two materials are 30 m and 70 m in the horizontal direction, and 6 m and 14 m in the vertical direction. The medium is therefore anisotropic. An unconditional Markovian realization is generated and the material types at the wells are considered to be known in the sequential generation of the conditional Markovian realizations. Figure E1 shows the unconditional realization and one conditional realization. At the wells, material types are the same in both realizations.

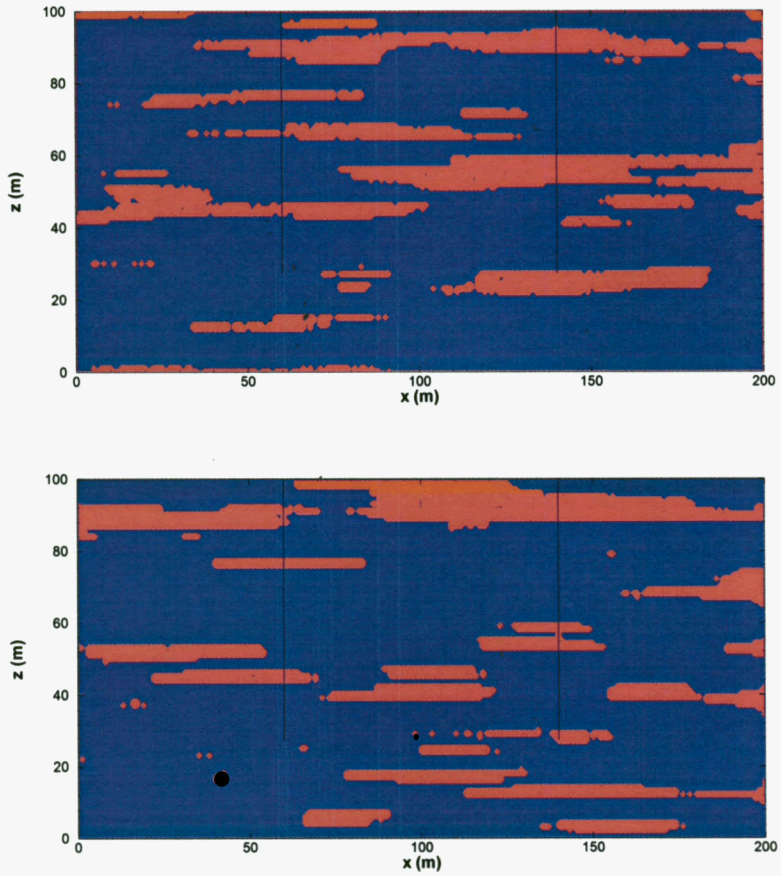

Figure E1. The conditional realization (upper) and one conditional realization (lower)

We first perform a flow simulation with a homogeneous permeability of lgK =-12.5 (the unit of K is m^2), under constant heads at left and right vertical boundaries and no-flux at the upper and lower boundaries. For each Markovian realization, the log (10-based) permeability of the less permeable material is assigned to be –13.0. The permeability of the higher permeable material is determined using an inverse approach (PEST) such that the flux at the boundaries are the same as those in the flow simulation with a homogeneous permeability. The histogram of the permeability of material 2 for all 100 realizations is shown in Figure (E2). It is seen from the figure that the distribution is more-or-less normal. The mean and variance of $\lg K_2$ is –11.49 and 0.0089, respectively.

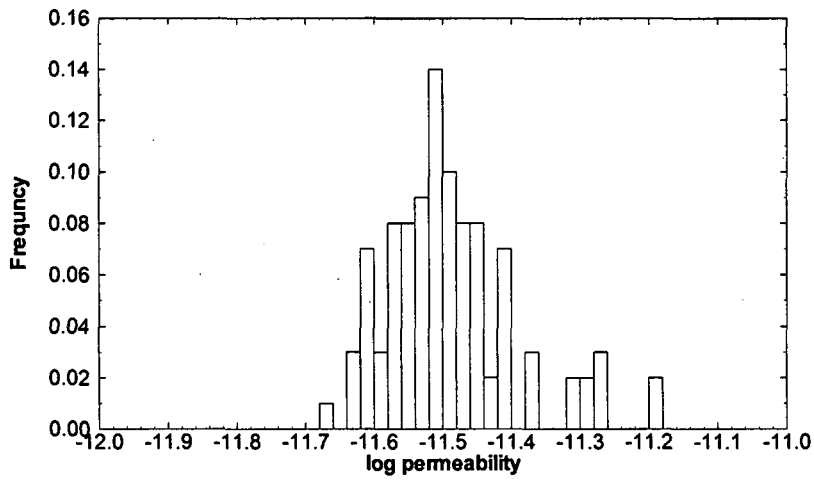

Figure E2. Histogram of the log permeability for material 2

The mean of the $\lg K_2$ can also be determined analytically using (E5). For a binary medium, the mean and variance of the composite medium can be expressed as

$$\langle Y\rangle = \langle \ln K\rangle = f_1\langle Y_1\rangle + f_2\langle Y_2\rangle = \langle Y_1\rangle + f_2(\langle Y_2\rangle - \langle Y_1\rangle) \tag{E6}$$

$$\sigma_Y^2 = f_1 f_2 (\langle Y_2\rangle - \langle Y_1\rangle)^2 \tag{E7}$$

Substituting (E6)-(E7) into (E5) and taking the natural log on both sides of (E5), one has

$$\ln K_{ef}^{(i)} = \langle Y_1\rangle + f_2(\langle Y_2\rangle - \langle Y_1\rangle) + f_1 f_2\left[\frac{1}{2} - \frac{1}{D}\frac{l_h}{l_i}\right](\langle Y_2\rangle - \langle Y_1\rangle)^2 \tag{E8}$$

Solving for $\langle Y_2\rangle$ yields

$$\langle Y_2\rangle = \langle Y_1\rangle + \frac{-f_2 \pm \sqrt{f_2^2 - 4 f_1 f_2 A(\langle Y_1\rangle - \ln K_{ef}^{(i)})}}{2 f_1 f_2 A} \tag{E9}$$

where A = $1/2 - l_h/Dl_i$. In our case, the correlation length of the indicator variable in the horizontal direction, using (L12), is $\lambda_I^{(x)} = 7.0m$, and that in the vertical direction is $\lambda_I^{(x)} = 1.4m$, thus $l_h = \lambda_I^{(x)}\lambda_I^{(y)}/(\lambda_I^{(x)} + \lambda_I^{(y)}) = 1.167$. For flow in the horizontal direction we have $l_i = 7.0$. Substituting these data into (E9) gives one feasible solution $\langle Y_2\rangle$ = -11.5, which is almost identical to the value of –11.49 from Monte Carlo simulations.

8.9 Upscaling

An important issue in the numerical simulation of groundwater flow and solute transport is the problem of scale. Data are collected at a scale different from the scale considered in field-scale flow and transport models.. For instance, the hydraulic conductivity obtained from core measurements, slug tests or packer tests, support scales in the order of centimeters to meters, whereas numerical models for groundwater flow requires conductivity values representative of tens to hundreds of meters. The process that transfers data from a small scale to a larger is called upscaling. The purpose of the upscaling procedure is to obtain a description of conductivity spatial variability at the numerical scale that reproduces same average behavior of the conductivity field at the measurement scale.

Hydraulic conductivity is not an additive property. It is well known that the equivalent conductivity for a group of cells serially arranged is equal to their harmonic average, whereas if the cells are arranged in parallel the equivalent conductivity is equal to their arithmetic mean. It has been shown that the equivalent conductivity of a heterogeneous block, which consists a number of cells that are at the support scale, is bounded above and below by the arithmetic and harmonic averages, respectively.

The block conductivity is defined from an extension of Darcy's law as:

$$\frac{1}{V}\int_V \boldsymbol{K}_\omega(x)\nabla h_\omega(x)dx = \boldsymbol{K}_V\left(\frac{1}{V}\int_V \nabla h_\omega(x)dx\right) \qquad \text{(U1)}$$

where V represents the block support, $\boldsymbol{K}_\omega$ is hydraulic conductivity at the support scale ω, and h_ω is the piezometric head at cell ω. A number of methods have been developed for computing the block conductivity. One of the commonly used methods is the power-averaging which is defined as [*Journel et al.*, 1986]:

$$\mu_p = \left(\frac{1}{V}\int_V [k(x)]^p\right)^{1/p} \qquad \text{(U2)}$$

where p depends on the spatial distribution of permeability and ranges from –1 to 1. When p = -1.0, the equivalent conductivity is equal to the arithmetic mean of conductivities of the elements in the block; when p = 1.0, the equivalent conductivity is equal to the harmonic mean of conductivities of the elements in the block. If p approaches to zero, the derived conductivity is the geometric mean.

Simplified renormalization was proposed by Le Loc'h. The calculation is done by successive grouping a number of finer meshes to form a coarser mesh. If the finer meshes are in series relative to their flow direction, the element permeabilities are averaged with a harmonic mean. If they are in parallel, an arithmetic mean is used. At each iteration, the direction of grouping is changed. In two directions, for example, a grouping along the x direction is followed by a grouping in the y direction, as illustrated in upper part of Figure U1. Alternatively, one may start from a grouping in the y direction first and then a grouping in the x direction (as shown in the lower part of Figure U1. The final resulting permeability values depend on the order of groupings.

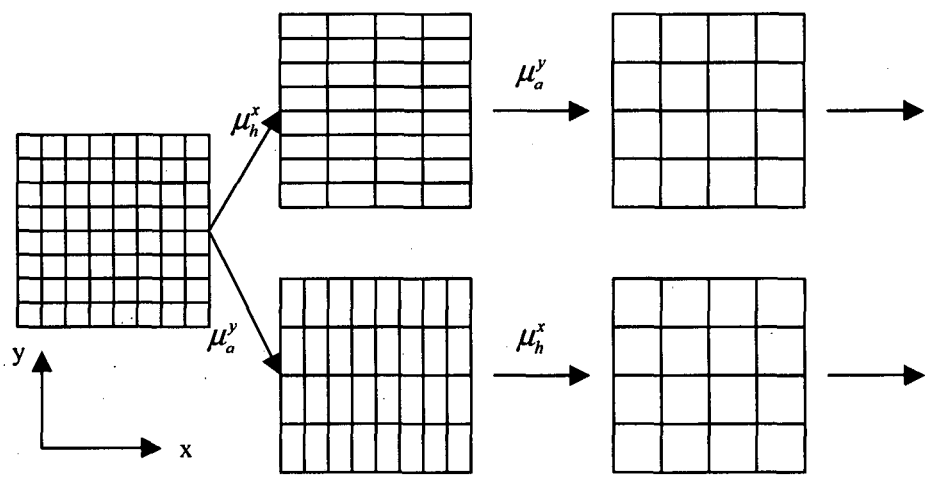

Figure U1: Scheme of a simple renormalization

We have explored the scaling of flow and transport behavior by considering the scale-average of hydraulic conductivity at multiple scales in the numerical aquifer system. We considered a two-dimensional square domain of a size 25.6 m by 25.6 m in the x and y directions. Five different levels of resolutions were considered: the number of uniform grid elements along each of two principle directions N = 256, 128, 64, 32, and 16. The grid with N = 256 corresponds to the fully resolved baseline hydraulic conductivity field and the grid with N = 16 corresponds to the greatest degree of spatial averaging considered. The baseline hydraulic conductivity field was generated using GCOSIM (*Gomez-Hernandez*, 1991), with a zero mean, a unit variance, and a correlation length of $\lambda = 5.0$ m.

The simple renormalization method was used to derive the hydraulic conductivity fields for different level of upscaling (Figure 8-7). The finite element numerical code was employed to solve for the flow field. It is seen that there is no significant difference on hydraulic head between different levels of upscaled hydraulic conductivity fields (Figure 8-8).

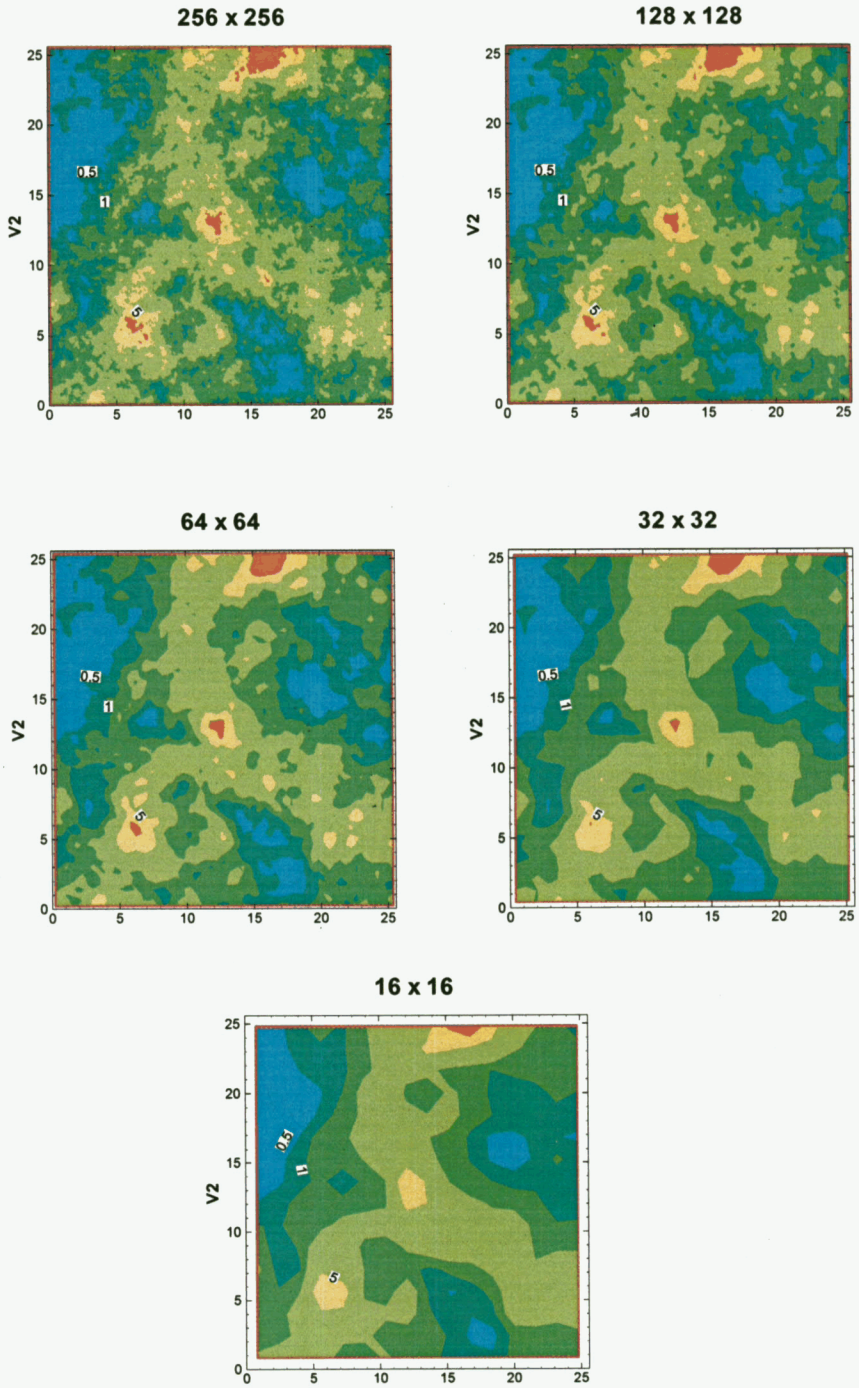

Figure 8-7. The hydraulic conductivity fields with different resolutions

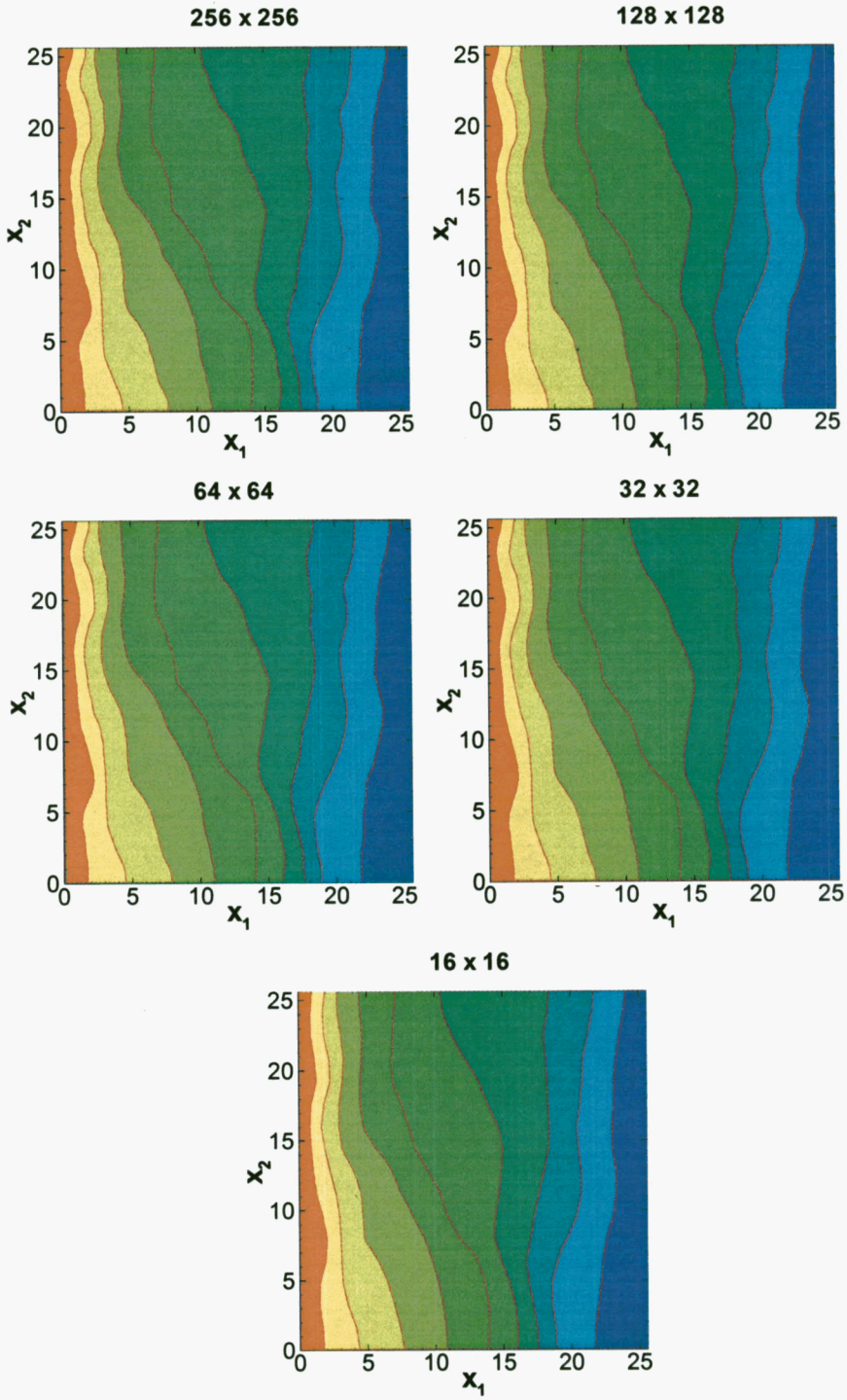

Figure 8-8. : The hydraulic head fields obtained from different resolutions of the hydraulic conductivity fields

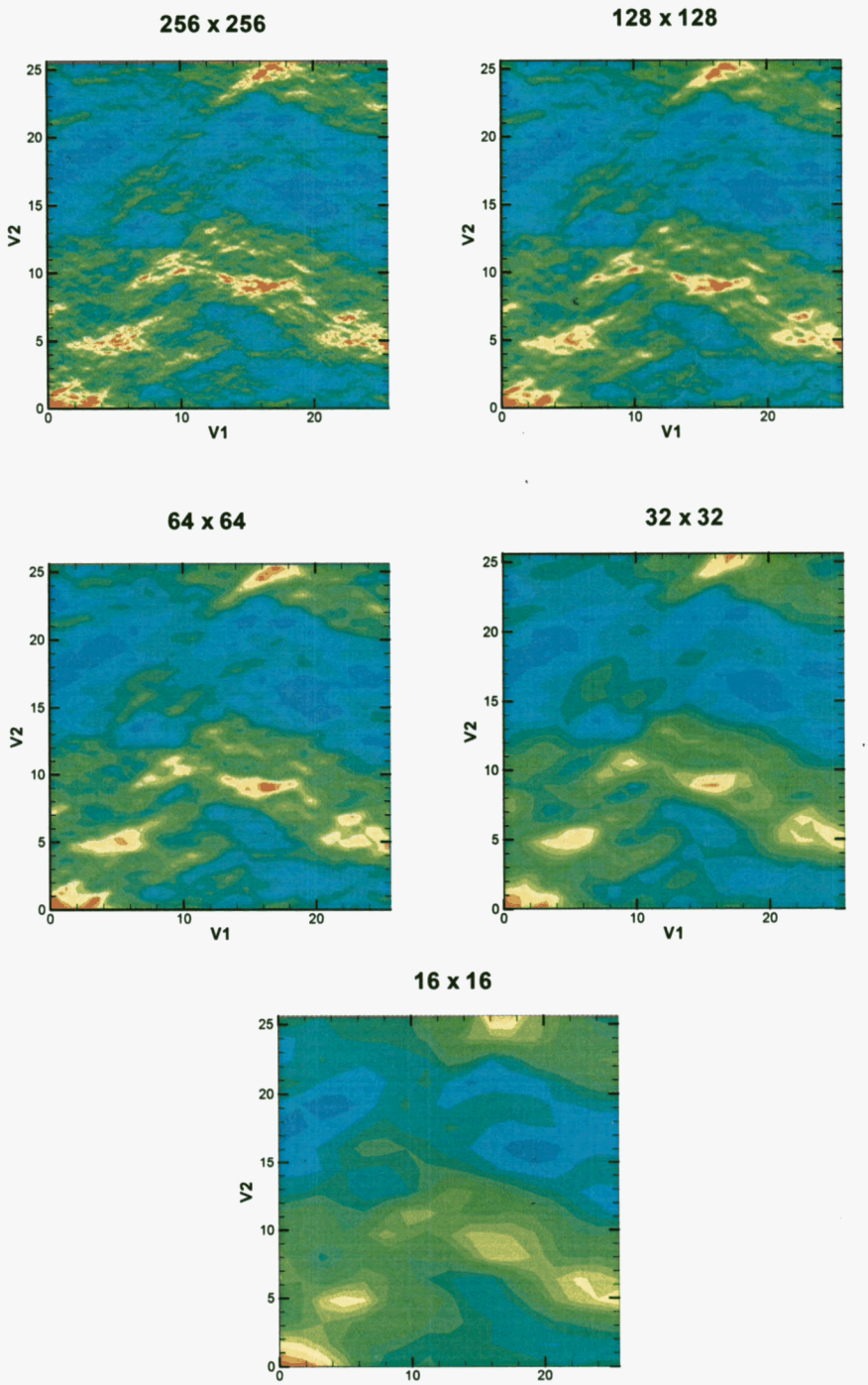

Figure 8-9. The longitudinal velocity fields obtained from different resolutions of the hydraulic conductivity fields

The effect of upscaling on solute transport was studied using two approaches. Using the method of characteristics approach, the MOC solves the classical convection-dispersion equation in variably saturated porous media (Bear, 1972), which can be expressed as:

$$\nabla(D_{ij} \cdot \nabla C) - q \cdot \nabla C = \theta \frac{\partial C}{\partial t} \tag{U3}$$

where C is the solute concentration, θ is the water content, and Dij is the dispersion coefficient tensor. The dispersion coefficient is generally defined as

$$D_{ij} = (\alpha_L - \alpha_T)\frac{q_i q_j}{q} + \alpha_T q \delta_{ij} + D_m \tag{U4}$$

where α_L and α_T are the longitudinal and transverse dispersivities, respectively; qi is the specific discharge at the ith direction, q is the magnitude of specific discharge; δ_{ij} is the Kronecker delta ($\delta_{ij} = 1$, if i = j and 0 otherwise); and Dm is the molecular diffusion, which is generally small and can be omitted. In this study, we assume both longitudinal and transverse local dispersivity values are zero. Nevertheless, small numerical dispersion exists in our simulations. Solutions to (U3) require the specification of the initial and boundary conditions. In our simulation, the initial concentration in the flow domain was assumed zero everywhere. Zero concentration flux boundary conditions were assigned to the upper and lower sides of the flow domain. At the right side of the flow domain, non diffusive flux boundary condition was specified. A prescribed concentration is specified at the middle of the left boundary.

During the solute transport simulation, the time step used for each case under different mean pressure heads was selected by using the maximum velocity in the field. In other words, the time step is selected in a way such that any solute particle within one element at the current time will remain in the element or in the adjacent elements within next time step. The selection of the time step allows us to avoid numerical instability and minimize numerical dispersion. The concentration distributions for different resolutions of the hydraulic conductivity fields are shown in Figure 8-10. The difference in concentration distributions represents the dispersion effect due to heterogeneity of the hydraulic conductivity fields and numerical grids. To see the effect of numerical dispersion, we solved the concentration fields with uniform hydraulic conductivity fields on the same numerical grids as those heterogeneous cases. The concentration distributions for different grids are shown in Figure 8-11.

Another way is the particle-tracking technique. For a particle originating from a location a at time $t = t_0$, its trajectory is described by the following kinetic equation

$$\frac{dX(t;\boldsymbol{a},t_0)}{dt} = \boldsymbol{V}[\boldsymbol{X}(t;\boldsymbol{a},t_0)] \tag{U5}$$

subject to the initial condition $\boldsymbol{X}(t_0;\boldsymbol{a},t_0)=\boldsymbol{a}$, where $\boldsymbol{X}(t_0;\boldsymbol{a},t_0)$ stands for the particle position at time t and $\boldsymbol{V}[\boldsymbol{X}(t;\boldsymbol{a},t_0)]$ denotes the Lagrangian velocity of the particle. Once the Eulerian velocity field is obtained from the flow simulation, it is converted to the Lagrangian velocity field based on the position at which the particle was released and then Equ. (U5) is solved step by step from the time $t = t_0$ to any elapsed time.

In our case, a particle is placed at the middle of the left boundary, i.e., x = 0 and y = 12.8 m. The trajectories for different levels of upscaling were illustrated in Figure 8-12. The figure shows that there is no significant difference between different levels of upscaling.

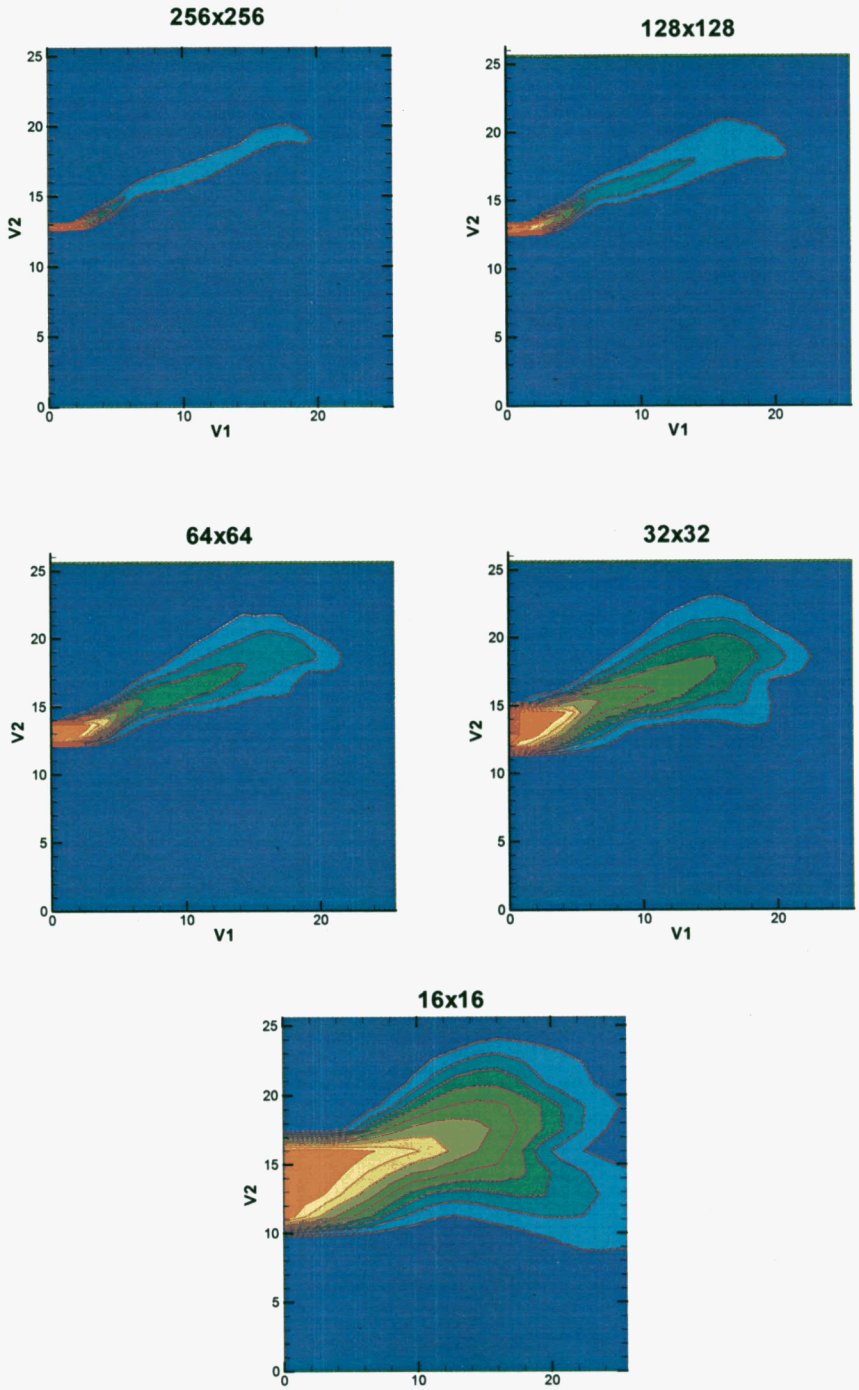

Figure 8-10. Concentration fields corresponding to different resolutions of heterogeneous hydraulic conductivity fields

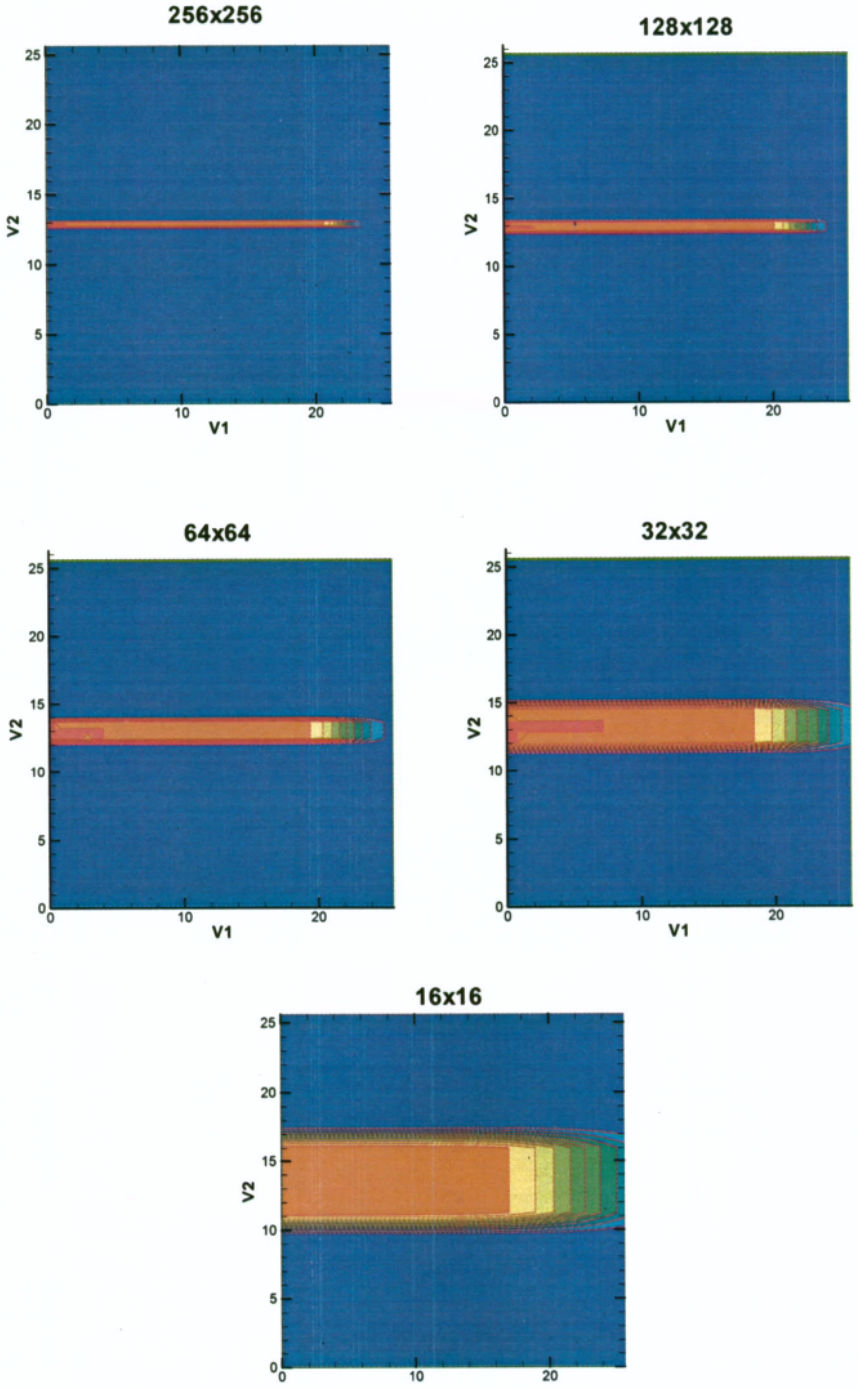

Figure 8-11. : Concentration fields corresponding to different resolutions of homogeneous hydraulic conductivity fields

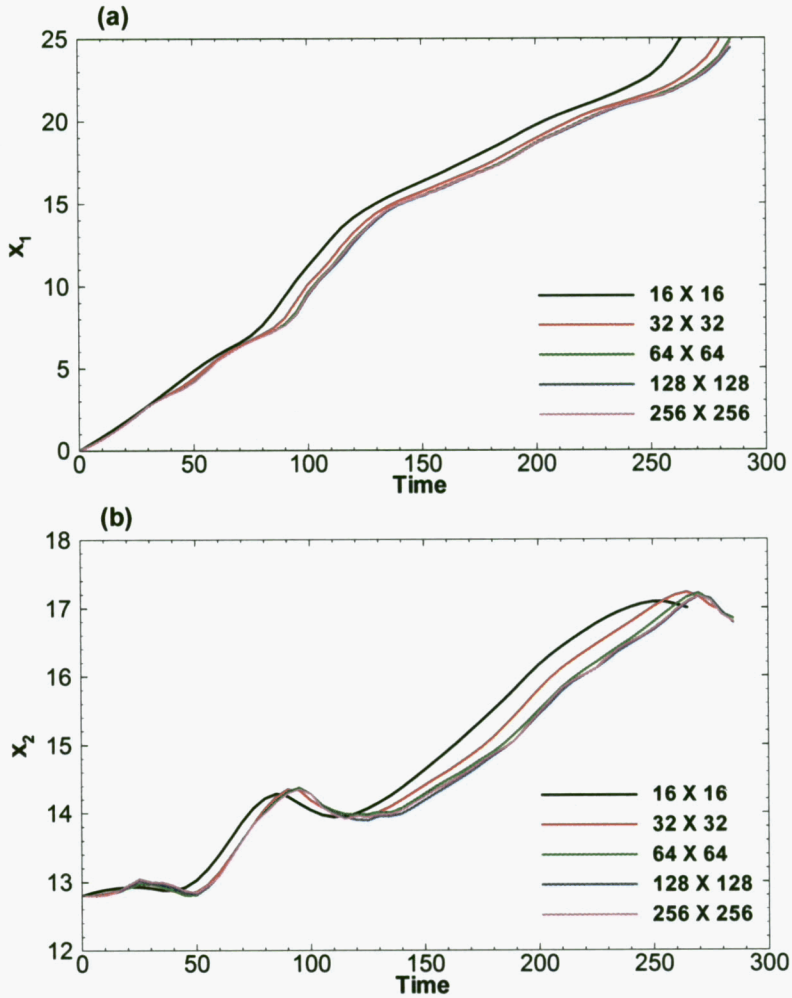

Figure 8-12. Trajectories of the particle released at (0, 12,8m), for different resolutions of the hydraulic conductivity fields

9 REFERENCES

Agterberg, F. P. (1974). Geomathematics. New York, Elsevier Sci.

Birdsell, K., A. V. Wolfsberg, et al. (2000). "Groundwater flow and radionuclide transport calculations for a performance assessment of a low-level waste site." Journal of Contaminant Hydrology **46**: 99-129.

Carey, B., G. Cole, et al. (1999).Revised site-wide geologic model for Los Alamos National Laboratory (FY99). LA-UR-00-2056.

Carle, S. F. (1996). A transition probability-based approach to geostatistical characterization of hydrostratigraphic architecture,. Ph.D. dissertation, Univ. of Calif., Davis: 182 pp.

Carle, S. F. (1997). "Implementation schemes for avoiding artifact discontinuities in simulated annealing,." *Mathematical Geology* **29**(2): 231-244.

Carle, S. F., Integration of geologic interpretation into geostatistical simulation, in , edited by , pp.,., 1997. (1997). Integration of geologic interpretation into geostatistical simulation. *Third Annual Conference of the International Association for Mathematical Geology*, Barcelona, Spain, International Association for Mathematical Geology.

Carle, S. F. and G. E. Fogg (1997.). "Modeling spatial variability with one- and multi-dimensional continuous Markov chains." *Math. Geology* **29**(7): 891-918.

Carle, S. F., E. M. LaBolle, et al. (1998.). Conditional simulation of hydrofacies architecture: A transition probability/Markov approach, in Hydrogeologic Models of Sedimentary Aquifers. *SEPM Concepts in Hydrogeology Environmental Geology*. O. S. Fraser and J. M. Davis. Tulsa, Okla., Society for Sediment. Geology. **1:** 147-170.

Carrera, J. and S. P. Neuman (1986). "Estimation of Aquifer Parameters Under Transient and Steady State Conditions: 2. {Uniqueness,} Stability, and Solution Algorithms." Water Resources Research **25**: 211-227.

Deutsch, C. and A. Journel (1992). *GSLIB: Geostatistical Software Library*. New York,, Oxford Univ. Press.

Doherty, J. (1997). Parallel {PEST}. Brisbane, Australia, Watermark Computing.

Doherty, J., L. Brebber, et al. (1994). {PEST}: Model Independent Parameter Estimation. Brisbane, Australia, Watermark Computing.

Fogg, G. E. (1989). Emergence of geologic and stochastic approaches for characterization of heterogeneous aquifers. NWWA Conference,, Dallas, Texas, National Well Water Association.

Fogg, G. E., C. D. Noyes, et al. (1998). " Geologically-based model of heterogeneous hydraulic conductivity in an alluvial setting." Hydrologeology Journal **6**(1): 131-143.

Freeze, R. A. (1975). " A stochastic-conceptual analysis of one-dimensional groundwater flow in nonuniform homogeneous media." *Water Resources Research* **11**(5): 725-741.

Freeze, R. A. and P. A. Witherspoon (1967). "Theoretical analysis of regional groundwater flow, 2, Effect of water-table configuration and subsurface permeability variation." Water Resources Research **3**: 623-634.

Gelhar, L. W. (1986). " Stochastic subsurface hydrology from theory to applications." *Water Resouces Research* **22**(9): 135S-145S.

Gelhar, L. W. (1993). *Stochastic Subsurface Hydrology*. Englewood Cliffs, N. J., Prentice-Hall.

Gomez-Hernandez, J. J. (1991). A Stochastic Approach to the Simulation of Block Conductivity Fields Conditioned Upon Data Measured at a Smaller Scale. *Stanford, California, Stanford University.*

Gomez-Hernandez, J. J. (1991). A stochastic approach to the simulation of block conductivity fields conditioned upon data measured at a smaller scale. Stanford, California, Stanford University.

Gomez-Hernandez, J. J. and E. F. Cassiraga (1994). Theory and practice of sequential simulation. Geostatistical Simulations. M. Armstrong and P. A. Dowd. Norwell, Mass.,, Kluwer Academics: 111-124.

Gomez-Hernandez, J. J. and S. M. Gorelick (1989). "Effective groundwater model parameter values: Influence of spatial variability of hydraulic conductivity, leakance, and recharge." Water Resources Resources **25**(3): 405-420.

Gomez-Hernandez, J. J. and A. G. Journel (1993). Joint sequential simulation of multi-Gaussian fields. *4th Annual International Geostatistical Congress-Geostatistic*, Norwell, Mass, Kluwer, Acad.

Gomez-Hernandez, J. J. and R. M. Srivastava (1990). " ISIS3D: An ansi-C three-dimensional multiple indicator conditional simulation program,." Comput. Geosc **16**(4): 395-440.

Gutjahr, A. L. (1989). Fast Fourier transform for random field generation, project report for Los Alamos grant, contract 4-R58-2690R,. Socorro, NM, N. M. Inst. of Min. and Technology.

Haldorsen, H. H., C. J. MacDonald, et al. (1988). Review of the stochastic nature of reservoirs. *Mathematics in Oil Production*. S. Edwards and P. R. King: 109-210.

Harbaugh, J. W. and G. F. Bonham-Carter (1970). Computer simulation in geology. New York, Wiley-Interscience.

Hoeksema, R. J. and P. K. Kitanidis (1984). " An application of the geostatistical approach to the inverse problem in two-dimensional groundwater modeling." *Water Resour. Res* **20**(7): 1003-1020.

Hoeksema, R. J. and P. K. Kitanidis (1985). " Analysis of the spatial structure of properties of selected aquifers." *Water Resour. Res.* **21**(4): 563-572.

Journel, A. G. (1983). " Non-parametric estimation of spatial distributions." *Math. Geol.* **15**(3): 445-468.

Journel, A. G. and F. Alabert (1987). " Focusing on spatial connectivity of extreme-valued attributes: Stochastic indicator models of reservoir heterogeneities." *SPE Tech. Pap. 18324*.

Journel, A. G. and C. J. Huijbregts (1978). *Mining Geostatistics*. San Diego, Calif., Academic.

Keating, E., E. Kwicklis, et al. (2000).A Regional Flow and Transport Model for Groundwater at Los Alamos National Laboratory. Los Alamos National Laboratory. A progress report submitted to the Hydrogeologic Characterization Program. LA-UR-01-2199.

Keating, E., V. V. Vesselinov, et al. (2001). **Coupling a Large-Scale Basin Model With a High Resolution Local Model Using a Finite-Element Flow and Transport Solver (FEHM) and an Automated Parameter Estimator (PEST)**. MODFLOW 2001 and Other Modeling Odysseys, Golden, Colorado, International Ground Water Modeling Center.

Kelley, V. C. (1978). Geology of the Espanola Basin. New Mexico Bureau of Mines and Mineral Resources Map

Landmark (1998). Stratamodel- Stratigraphic Geocellular Modeling, Landmark Graphics.

Longmire, P. A., D. Broxton, et al. (2001).Characterization Well R-15 Completion Report. Los Alamos National Laboratory Report. LA-13749-MS.

Purtymun, W. D. (1995).Geologic and hydrologic records of observation wells, test holes, test wells, supply wells, springs, and surface water stations in the Los Alamos area. Los Alamos National Laboratory Report. LA-12883-MS.

Purtymun, W. D., A. K. Stoker, et al. (1995).Water supply at Los Alamos during 1993. Los Alamos National Laboratory. LA-12951-PR.

Reneau, S. (2001), personal communication. .

Rogers, D. and B. Gallaher (1995).The unsaturated characteristics of the Bandelier Tuff. Los Alamos National Laboratory. LA-12968-MS.88.

Trease, H., D. George, et al. (1996). The X3D grid generation system. Numerical grid generation system in computational fluid dynamics and related fields. B. K. Soni, J. F. Thompson, H. Hausser and P. R. Eiseman.

Vecchia, A. V. and R. L. Cooley (1987). "Simultaneous Confidence and Prediction Intervals for Nonlinear Regression Models with Application to a Groundwater Flow Model." Water Resources Research **23**(7): 1237-1250.

Waresback, B. D. (1986). The Puye Formation, New Mexico: analysis of a continental rift-filling, volcaniclastic alluvial-fan sequence, University of Texas at Arlington.

Zyvoloski, G. A., B. A. Robinson, et al. (1997).Summary of the Models and Methods for the {FEHM} Application --- A Finite-Element Heat- and Mass-Transfer Code. Los Alamos National Laboratory. LA-13306-MS.

10 APPENDIX A. WATER LEVEL AND PERMEABILITY DATA

Table A-1. Most recent water level data from wells in the vicinity of LANL

	Well	Water level	Top of screen	Bottom of screen	Year	Water level	Figure 2-1
Pajarito Plateau							
Test wells	R-9	5696	1738	1718	1998	1737	Y
	R-7						Y
	R-31-5	5851	1637	1634	2000	1784	
	R-31-4	5854	1691	1688	2000	1785	
	R-31-3	5852	1741	1738	2000	1784	
	R-31-2	5853	1787	1777	2000	1784	Y
	R-25-8	6153	1743	1740	2000	1876	
	R-25-7	6177	1801	1798	2000	1883	
	R-25-6	6203	1862	1859	2000	1891	
	R-25-5	6220	1895	1892	1998	1896	Y
	R-22-4	5670	1596	1598	2000	1729	
	R-22-3	5682	1632	1630	2000	1732	
	R-22-2	5725	1731	1718	2000	1745	
	R-22-1	5730	1754	1741	2000	1747	Y
	R-19-7	5904	1594	1591	2000	1800	
	R-19-6	5932	1626	1624	2000	1809	
	R-19-3	5882	1795	1782	2000	1793	Y
	R-15	5854	1786	1768	2000	1785	
	R-12	6080	1739	1727	1999	1738	Y
	DT-10	5921	1809	1710	1998	1805	Y
	DT-5a	5950	1818	1620	1996	1814	Y
	DT-9	5917	1717	1656	1998	1804	Y
	TW-1	5837	1751	1748	1998	1780	
	TW-2	5848	1794	1782	1996	1783	Y
	TW-3	5810	1784	1766	1997	1771	Y
	TW-4	6066	1851	1842	1996	1849	Y
	TW-8	5884	1801	1762	1997	1794	Y
	H-19		1899	1899		0	Y
	SHB-3	6942	2063	2060	1994	2116	
Water Supply	G-1	5705	1737	1219	1997	1739	Y
	G-1A	5709	1752	1373	1997	1741	Y

	G-2	5700	1761	1249	1997	1738	Y
	G-3	5764	1737	1327	1986	1757	Y
	G-4	5863	1772	1315	1997	1788	Y
	G-5	5858	1713	1466	1994	1786	Y
	G-6	5857	1789	1353	1997	1786	Y
	LA-1	5537	1695	1450	1990	1688	Y
	LA-1B	5646	1616	1199	1996	1721	Y
	LA-2	5525	1690	1458	1991	1684	Y
	LA-3	5560	1697	1466	1991	1695	Y
	LA-4	5706	1592	1223	1987	1740	Y
	LA-5	5671	1646	1249	1987	1729	Y
	LA-6	5678	1631	1217	1985	1731	Y
	PM-1	5737	1693	1225	1997	1749	
	PM-2	5847	1742	1353	1995	1783	
	PM-3	5859	1732	1252	1997	1786	
	PM-4	5827	1726	1240	1997	1777	
	PM-5	5840	1724	1226	1997	1780	
	O-4	5863	1680	1228	1995	1788	
	O-1	5793	1640	1195	1990	1766	
Buckman well field							
Test Wells	SF-2A	5510	1125	1122	1997	1680	
	SF-2B	5038	1445	1441	1997	1536	
	SF-2C	5320	1590	1587	1997	1622	
	SF-3A	5307	1587	1584	1997	1618	
	SF-3B	5466	1625	1622	1997	1666	
	SF-3C	5467	1659	1655	1997	1667	
	SF-4A	5326	1588	1585	1997	1624	
	SF-4B	5468	1634	1631	1997	1667	
	SF-4C	5461	1655	1652	1997	1665	
	SF-5C	5453	1648	1645	1997	1663	
	Buckman 5	5431	1690	1440	1998	1656	
	Buckman 6	5408	1685	1319	1998	1649	
	Buckman 7	4932	1648	1282	1997	1504	

Table A-2. Permeability data for wells on the Pajarito Plateau, and average linear velocity estimates

Stratigraphic unit	Well	Fraction [a]	Hydraulic conductivity			Average linear velocity[b]
			Log m^2	Ft/day	method[c]	m/yr
Tsf	O-1	0.99	-12.64	0.64	P	7.1
	LA-6	1	-12.36	1.21	P	13.5
	LA-5	1	-12.84	0.40	P	4.5
	LA-4	1	-12.56	0.77	P	8.5
	LA-3	1	-12.80	0.44	P	4.9
	LA-2	1	-12.77	0.47	P	5.2
	LA-1B	1	-12.35	1.24	P	13.8
	G-4	0.52	-12.26	1.53	P	17.0
	G-3	0.52	-12.59	0.71	P	7.9
	G-2	0.65	-12.36	1.21	P	13.5
	G-1A	0.53	-12.36	1.21	P	13.5
	G-1	0.59	-12.47	0.94	P	10.5
Tsfuv	DT-9	0.73	-11.23	16.36	P	182.0
	O-4	0.61	-11.84	4.02	P	44.7
	PM-4	0.6	-11.94	3.19	P	35.5
Tpf	CDV-R-15	1	-12.70	0.56	G	6.2
	CDV-R-15	1	-13.10	0.22	G	2.4
	CDV-R-15	1	-13.19	0.18	G	2.0
	CDV-R-15	1	-12.57	0.74	G	8.2
	R7	1	-13.44	0.10	G	1.1
	R-19	1	-12.90	0.35	G	3.9
	R-19	1	-12.30	1.40	G	15.6
	R-19	1	-12.67	0.60	G	6.7
	R-15	1	-12.14	2.01	I	22.4
	R-15	1	-11.92	3.34	I	37.2
	R-19	1	-11.20	17.53	I	195.0
	R-19	1	-11.15	19.67	I	218.8
	CDV-R-15	1	-13.05	0.25	I	2.8
	CDV-R-15	1	-13.44	0.10	I	1.1
	TW-8	1	-11.92	3.34	P	37.2

Tpt	TW-3	1	-11.24	15.98	P	177.9
	TW-2	1	-10.93	32.64	P	363.2
	TW-1	1	-12.71	0.54	P	6.0
	R-31	1	-12.41	1.08	I	12.0
	R-31	1	-12.82	0.42	I	4.7
	R-31	1	-11.88	3.66	I	40.7
	R-31	1	-14.49	0.01	I	0.1
	R-31	1	-14.60	0.01	I	0.1
	R-9i	1	-10.87	37.47	I	417.0
	R-9i	1	-12.55	0.78	I	8.7
Tb	PM-5	.60 (Tb2)	-12.59	0.71	P	7.9
	G-5	.79 (Tb1)	-12.38	1.16	P	12.9
	DT-10	.63 (Tb4)	-11.27	14.92	P	166.0
Tt	TW-4	1	-12.04	2.53	P	28.2

[a] fraction of screened interval occupied by given hydrostratigraphic unit

[b] assuming horizontal flow, hydraulic gradient = 0.01, effective porosity = 0.1.

[c] P=pump test; I= injection test; G=geophysical log

APPENDIX B. HYDROSTRATIGRAPHY AS INTERPOLATED ONTO LOCAL-SCALE MODEL GRID

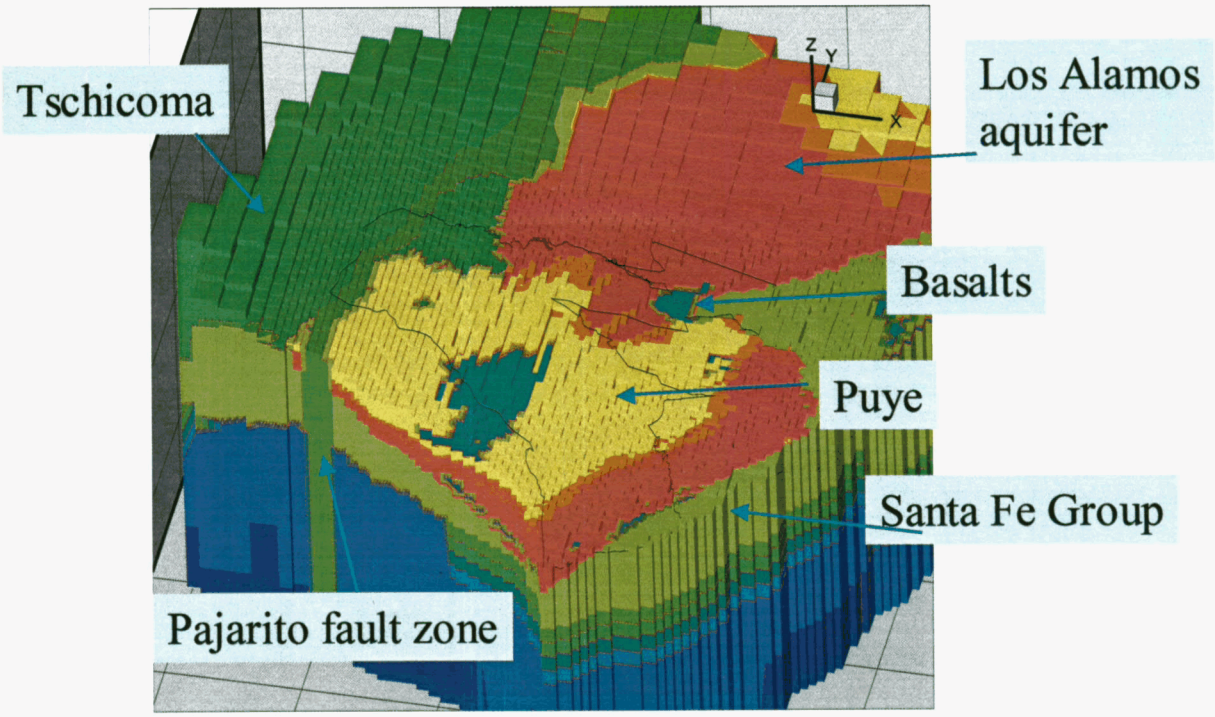

Figure B-1. Local-scale grid, with elements colored according to hydrostratigraphy

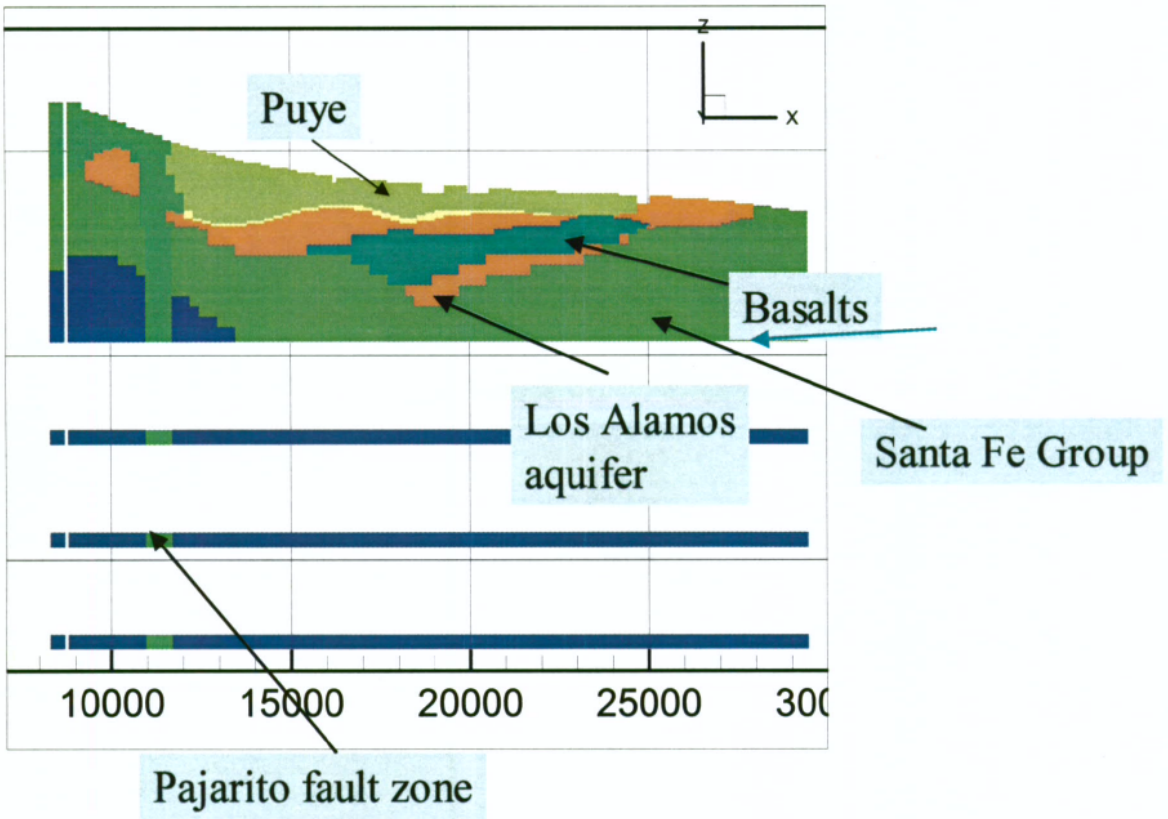

Figure B-2. E-W cross-section of local-scale grid, beneath LANL

APPENDIX C. DATA USED IN MARKOV CHAIN MODELS

Table C-3. Textural class data compiled from Waresback (1986) dataset

Outcrop name	Thickness d (m)	Gravel		Coarse sand		Fine sand		Clay		Totavi Lentil	
		%	d	%	d	%	d	%	d	%	d
LA-01 (Totavi)	86.3	48.5	2.79	7.0	0.6	17.1	1.64	19.4	2.1	N/A	0
GC-01	65.5	41.0	0.89	7.5	0.31	9.5	0.41	38.9	1.16	4.5	1.48
GC-02	70.01	44.1	0.66	5.0	0.18	8.0	0.29	35.0	0.63	13.8	3.22
GC-03	110.7	56.0	0.63	16.9	0.57	2.0	0.1	31.7	0.48	0.1	0.05
GC-04	100.7	73.9	0.46	11.7	0.24	4.6	0.19	10.9	0.12	0	0
SC-01	141.8	82.7	0.56	9.3	0.24	0.1	0	8.7	0.11	0	0
WR-01	27.3	42.4	0.05	13.3	0.06	14.7	0.14	33.3	0.08	0	0
BM-01	58.3	39.3	0.1	21.2	0.18	0.3	0.01	31.3	0.14	9.8	1.14
FR-01	50.8	50.0	0.1	12.6	0.08	0	0	13.9	0.05	25.4	1.61

Table C-4. Textual class data compiled from drillers lithologic logs

Well name	Thickness d (m)	Gravel		Coarse sand		Fine sand		Clay		Totavi Lentil		Fanglomerate		unclassified	
		%	d	%	d	%	d		d	%	d	%	d	%	d
R-9	108.9	30.3	4.7	29.0	3.5	39.9	5.4	0.6	0.3	0	0	0	0	0	0
R-12	72.9	40.5	7.4	29.6	10.8	24.1	8.8	0	0	0	0	0	0	5.8	4.2
R-15	115.9	59.5	69.0	8.4	9.8	25.0	29.0	0	0	1.8	2.1	0	0	5.3	6.1
cdV-R-15-3	272.8	9.5	13.0	67.9	14.3	19.0	5.8	0	0	0	0	0	0	3.6	4.9
R-19	133.8	29.6	4.0	58.1	4.3	3.9	2.6	0	0	0	0	0	0	9.6	6.4
R-25	228.3	21.4	48.8	69.0	26.3	2	2.3	0.3	0.6	0	0	0	0	7.3	16.8
R-31	119.8	14	16.8	0	0	0	0	0	0	82.2	98.5	0	0	3.8	4.6
TW-1	106.1									10.7	11.3	89.3	23.7		
TW-1A	18.6									0	0	100	9.3		
TW-2	235									0	0	100	117.5		
TW-2A	21.3									0	0	100	21.3		
TW-2B	48.8									0	0	100	48.8		
TW-3	173.1									10.9	18.9	89.1	77.1		
TW-4	73.2									0	0	100	73.2		
TW-8	131.1									0	0	100	65.5		

H-19	122.2									2.5	3.1	97.5	119.2		
TH-6	4.6									0	0	100	4.6		
Sigma Mesa 1992	141.7									5.4	7.6	94.6	67.1		
Layne Western	19.2									79.4	15.2	20.6	4.0		
LAO-4.5	7.9									0	0	100	7.9		
DT-5	6.7									0	0	100	6.7		
DT-5A	135.6									11.7	15.9	88.3	39.9		
DT-9	82.0									14.1	11.6	85.9	35.2		
DT-10	69.8									20.1	14.0	79.9	27.9		
LA-4	41.5									36.8	15.2	63.2	26.2		
G-1	19.2									81.0	15.5	19.1	3.7		
G-1A	33.5									57.3	19.2	42.7	14.3		
G-2	18.9									72.6	13.7	27.4	5.2		
G-3	28.4									55.9	15.9	44.1	12.5		
G-4	32									57.1	18.3	42.9	13.7		
G-5	36.3									0	0	100	36.3		
G-6	48.8									44.8	21.3	56.3	27.4		
PM-1	74.7									8.2	6.1	91.8	68.6		
PM-2	205.4									10.4	21.3	89.6	92.1		
PM-3	88.4									20.7	18.3	79.3	35.1		
PM-4	97.5									12.5	12.2	87.5	85.3		
PM-5	147.8									16.5	24.4	83.5	41.2		
O-1	143.3									12.8	18.3	87.2	41.7		
O-4	153.6									19.4	29.9	80.6	61.9		

Table C-5. Total thickness of the each material in wells and outcrop sections

		Gravel	Coarse sand	Fine sand	clay	Totavi	Total
Well	d (m)	2470.21	486.87	160.99	1.24	447.77	3567.08
	(%)	69.25	13.65	4.51	0.03	12.55	100.00
Outcrop	d (m)	371.32	74.34	22.81	142.67	110.76	721.91
	(%)	51.44	10.30	3.16	19.76	15.34	100.00

Table C-6. Thickness of Totavi Lentil measured at outcrops (m)

Location	North-South dimensions		East-West dimensions		Thickness (m)		Top elevation
	Min	Max	Min	Max	Min	Max	
Ancho Canyon	20.1	244	80.7	264	18.3	30.5	1755.6
Water canyon	20.4	223	61	122	12.2	18.3	1524
Mortandad Canyon	61	223	41	548.6	18.3	24.4	1774
Sandia Canyon	41	142	41	771.7	6.1	18.3	1792
Los Alamos Canyon	41	893.7	41	1097.3	6.1	30.5	1823
Mean	36.7	345.1	52.9	560.6	12.1	24.4	
Standard deviation	17.1	309.3	17.8	391.4	6.1	6.1	